

AD-A121 122

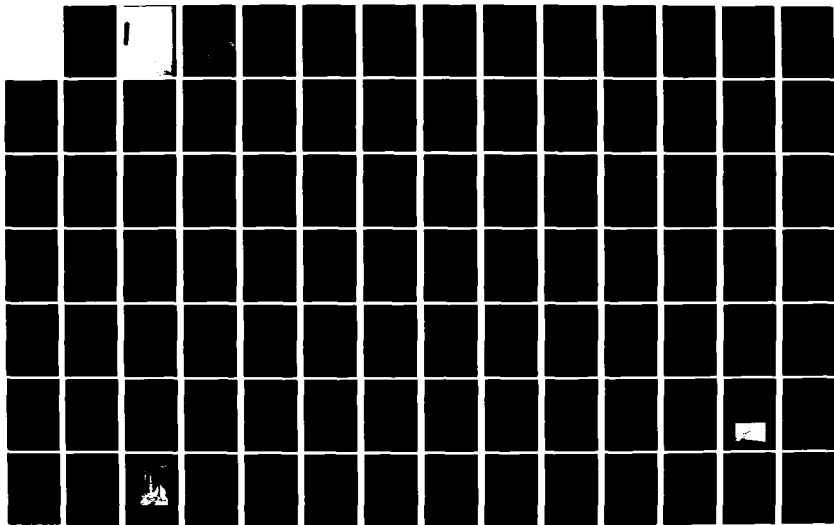
SUSPENDED SEDIMENT UNDER WAVES(U) SYDNEY UNIV
(AUSTRALIA) COASTAL STUDIES UNIT P NIELSEN ET AL.
SEP 82 CSU-TR-82/6 N00014-80-G-0001

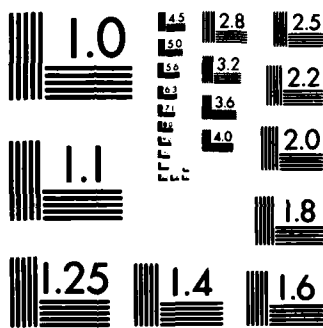
172

UNCLASSIFIED

F/G 8/3

NL





MICROCOPY RESOLUTION TEST CHART
NATIONAL BUREAU OF STANDARDS-1963-A

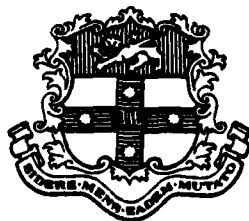
AA 121122

COASTAL STUDIES UNIT TECHNICAL REPORT No.82/6

September , 1982

SUSPENDED SEDIMENT UNDER WAVES

P.NIELSEN , M.O.GREEN and F.C.COFFEY



COASTAL STUDIES UNIT
DEPARTMENT OF GEOGRAPHY
THE UNIVERSITY OF SYDNEY
SYDNEY , N.S.W. 2006

DTIC
ELECTE
NOV 5 1982
D
H

Approved for public release.
Distribution Unlimited

CONTENTS

ABSTRACT

1. INTRODUCTION

2. HYDRODYNAMICS

Waves	7
Boundary Layers	12
Quantitative Descriptions of Boundary Layers	19
Prediction of f_0 , f_w and δ_1	37
Turbulence Structure of Wave Boundary Layers	43
Wave-Current Boundary Layers	49

3. THE MOTION OF SUSPENDED PARTICLES

Quantitative Approach	65
Simple Example	72
Second Order Effects	76

4. FIELD DATA

The Sediment Sampler	77
Transducer and Flowmeter Characteristics	79
Experimental procedure, determination of $c(z)$	82
Determination of h , T , H_s , \bar{U} and \bar{V}	86
Determination of C_0 , l_s , ϵ_s and ϵ_{sc}	87
Description of Experiment Sites	95

5. EMPIRICAL RESULTS

Sediment Distributions over Vortex Ripples	98
Grain Size Variation with Elevation over Vortex Ripples	107
Concentration Profiles over Flat Beds	111
Concentration Profiles over Megaripples	117
The Diffusion Approach to Near Bed Sediment Distributions	120
Concentration Magnitude	124
Influence of Wave Breaking on Concentration Profiles	131
Influence of Currents on Concentration Profiles	136
Shore Normal Sediment Transport	138
Shore Parallel Sediment Transport	141

REFERENCES

LIST OF SYMBOLS

HYDRODYNAMICS - SEDIMENT - and PROFILE DATA

MEASURED VALUES OF \bar{c} AND THE CORRESPONDING ELEVATIONS

Accession For	
NTIS GRA&I	<input checked="" type="checkbox"/>
DTIC TAB	<input type="checkbox"/>
Unannounced	<input type="checkbox"/>
Justification	
By	
Distribution	
Availability	
Notes	
A	



ACKNOWLEDGEMENTS

157

REPORT DOCUMENTATION PAGE

158

ABSTRACT

A new very simple and dependable field sediment sampler has been developed. It is a multi-siphon device that samples suspended sand from seven elevations simultaneously. The 65 concentration profiles that have been obtained so far are presented, complete with hydrodynamics and bed sediment data. The profiles were measured under breaking and non-breaking waves in a wide range of coastal environments all over Australia. These data together with a review of oscillatory boundary layer flow and the motion of suspended sand in an accelerated non uniform flow lead to a range of new insights into the processes of sediment entrainment under waves.

1. INTRODUCTION

Sediment transport in the coastal environment is often a result of the combined actions of waves and currents. A steady current must at first sight seem more efficient as a sand transporter than the back and forth motion of waves; but the process of picking the sand up from the bed is dominated by the waves. The efficiency of waves with respect of entrainment of sediment is due to two main characteristics of oscillatory water motion.

Firstly, the boundary layer of an oscillatory flow is thin: a few centimetres for typical wave periods, which means that wave induced near bed velocities and bed shear stresses become large.

Secondly, the periodic flow reversals cause the boundary layer to separate from the bed twice every period and send dense clouds of suspended sediment upwards. This is the first step of the entrainment process by which the suspended sand reaches elevations comparable to the wave boundary layer thickness. From this level it may either start to settle out again or rise further due to the mixing action of currents or wave breaking.

The present report gives a detailed discussion of these processes based on the literature and previous laboratory studies as well as a large amount of field data collected by the Coastal Studies Unit over the last two and a half years.

Chapter 2 deals with the hydrodynamic problems involved in sediment transport calculations, mainly the structure of wave boundary layers. Special emphasis is put onto developing formulae relating quantities such as boundary layer thickness, bed shear

stress and the turbulence structure with very few assumptions about the nature of the flow.

Previous experimental studies fall into three categories and the linking together of their results has so far been incomplete. Detailed velocity measurements like those of Kalkanis (1964) and Jonsson and Carlsen (1976) give good information about the average character of the flow and the shear stresses, but they get no direct information about the turbulence structure. Such information has become available later through the measurements of MacDonald (1977), Nakato et. al. (1977), Du Toit and Sleath (1981) and Kemp and Simons (1982). However, all of these except from Nakato et. al. used artificial solid beds. Natural sand beds were used by Carstens et. al. (1969) and Lofquist (1980) who measured energy dissipation and bed friction. The major aim of the analysis is to make the latter friction measurements useful for prediction of eddy viscosities and vertical length scales over natural sand beds.

Chapter 3 is an analysis of the motion of suspended sediment particles in an accelerated, non uniform flow field. The approach to the solution is new in that it splits the sediment particle velocity \vec{u}_p into three parts from the outset, $\vec{u}_p = \vec{u} + \vec{v} + \vec{w}$. \vec{u} is the water velocity, \vec{w} is the still water settling velocity and \vec{v} is the extra velocity which results from the fluid accelerations. Special attention is paid to the case of sand in vortices because this is the key to understanding the entrainment mechanism over rippled beds under waves, and the resulting sediment distributions. The simplest approximation $\vec{u}_p \approx \vec{u} + \vec{w}$ and the very simple kinematic arguments are used to show the essence of the trapping mechanism which makes it possible for grains of nearly all sizes to travel together inside migrating vortices. A process which leads to very similar dis-

tributions of all grain sizes over ripples. This process is fundamentally unlike gradient diffusion which leads to vastly different distributions for different grain sizes. The fact that sand and vortices travel together also explains why the distributions of sand and turbulence are very similar as observed by Nakato et. al. (1977) and MacDonald (1977).

Chapter 4 describes the experimental equipment and experimental technique. The sediment sampler was designed to sample a complete profile of time averaged concentrations simultaneously. This was done in order to overcome the large scatter problem encountered in previous field studies, e.g. Fairchild (1977) and Kana (1979). After obtaining well defined concentration profiles the problem is to extract parameters that are both practically and theoretically well defined, which can in turn be related to the flow of sediment characteristics. In the present study we extract these parameters from the profiles: C_0 , ϵ_B and ϵ_S . C_0 is the concentration at the bed level, ϵ_B represents the diffusivity inside the wave boundary layer and ϵ_S represents the larger diffusivity outside the boundary layer, due to wave breaking or currents. Some concentration profiles show an apparent increase in diffusivity or vertical length scale with distance from the bed, although there is neither breaking waves nor steady currents around to produce significant turbulence outside the boundary layer. This apparent increase is due to the variability of settling velocity in the suspended material. A method for correcting the observed diffusivities for this effect is devised. It is based on the diffusion equation and uses a continuous settling velocity distribution which leads to vastly simpler calculations than previous models that work with discrete size classes.

Chapter 5 is a heuristic discussion and analysis of the field measurements of the present study together with the results of some previous laboratory investigations. The clearest results are obtained in relation to the near bed sediment distributions. Over fully developed vortex ripples we find exponential concentration profiles

$$\bar{c}(z) = C_0 \exp(-z/l_s) \quad (1.1)$$

where the length scale l_s is approximately equal to the ripple height. Different grain sizes follow very similar distributions because the entrainment mechanism is convective as described in Chapter 3. The sediment gets trapped in the lee vortices while these are being formed, and when the vortices are released and travel upwards, they act as elevators for all grain sizes alike.

Over flat beds and round crested bed forms the vertical length scale of the concentration profiles is typically ten times smaller than over ripples, so it is rather difficult to obtain detailed information about the profile structure. However, the present data give a good indication that the lower part of the profiles scale on the hydraulic roughness length of the flat bed, and that the entrainment mechanism within the wave boundary layer is predominantly convective because the observed near bed length scales l_s ($=\epsilon_B/w$) depend little on the settling velocity.

The concentration magnitudes, C_0 , is somewhat more difficult to predict. It is probably valid to assume that C_0 depends mainly on the skin friction Shields parameter, θ' . However, a proper calculation of θ' for the laboratory data is difficult because most of them are in the transition region between laminar and turbulent flow.

This makes a comparison between laboratory and field values difficult. Furthermore the very different degrees of compaction of sand beds in the field is likely to result in variable relations between C_0 and θ' .

The data available on external mixing from wave breaking and currents are not yet sufficient for a detailed quantitative study. Instead we have given a qualitative description of the entrainment mechanisms due to two extremes: the heavily plunging breaker and the gently spilling breaker.

2. HYDRODYNAMICS

The water motion in the nearshore area and the surfzone involves velocities that vary over a large range of time scales, from diurnal tides to harmonics of wind waves with periods less than a second. It is often convenient to split the velocity, u , in two parts

$$u = \bar{u} + \tilde{u} \quad (2.1)$$

where \bar{u} is the steady or quasi steady part and \tilde{u} is periodic with zero mean.

The cutoff period, above which everything is considered quasi steady depends on the problem under consideration. Sometimes everything above wind wave periods (≈ 10 seconds) can be considered steady in other cases even the tide must be considered unsteady.

WAVES

The most important part of the water motion is due to wind waves and swell with periods between 5 and 20 seconds. At present there are no theories for non periodic waves so for any theoretical considerations, waves are assumed periodic. This is of course an idealized description since the wave period is normally quite variable just like the wave height H in the surf zone. The pressure record in Figure 2.1 gives an idea of this variability. It is necessary however for any theoretical work to represent the incoming waves by a monochromatic wave train with constant height. With respect to sediment transport the most relevant wave period is the one determined from zero crossings of the near bed

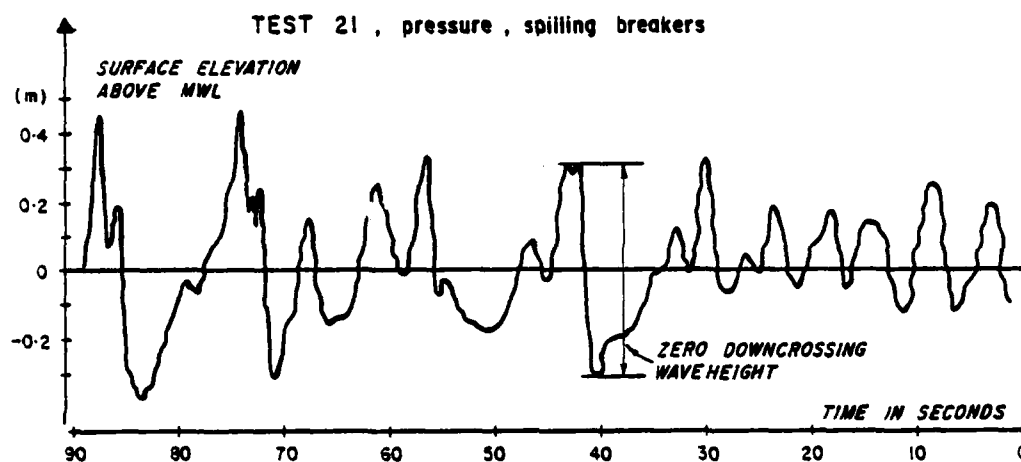


Figure 2.1: Instantaneous surface elevations measured by a pressure transducer. The waves are spilling breakers under a slight onshore wind (TEST 21, Broome 1981). Note that the time progresses from right to left. With typical records like this, the meanings of such terms as *wave period* and *wave height* are no longer trivial.

velocity because these flow reversals cause a break down of the boundary layer structure.

Individual waves are best characterized by their zero downcrossing height H , and for an ensemble of waves one may use either the average \bar{H} , the root-mean-square H_{rms} or the significant wave height H_s , which is the average of the highest 1/3 of the waves. The relevance of each of these measures depends on the phenomenon described. There is some evidence that H_s is superior for describing ripple geometry (Nielsen 1981) while H_{rms} seems to be the best for describing sediment concentrations (Rasmussen and Fredsoe 1981).

Since nearshore waves are often highly non linear and irregular the only way to get reliable information on the water motion at a given spot is by measuring it locally.

The best way of measuring the velocity field is by using an array of good flow meters. However, one may also derive the characteristic wave induced velocities from pressure measurements, and as long as our main concern is the velocity right at the bed, we may use linear wave theory. The relations between wave height and the pressure and velocity fluctuations for a sinus wave are

$$\bar{p}(z) = \rho g \frac{H}{2} \frac{\cosh kz}{\sinh kh} \quad (2.2)$$

$$\bar{u}(z) = \frac{\pi H}{T} \frac{\cosh kz}{\sinh kh} \quad (2.3)$$

and for the near bed velocity amplitude $\bar{u}(0)$ which will be referred to in the following as aw we get

$$aw = \frac{\pi H}{T \sinh kh} \quad (2.4)$$

the important parameter kh which is the local wave number, $k = 2\pi/L$ times the water depth, is determined by the dispersion relation

$$k_0 h = kh \tanh kh \quad (2.5)$$

This implicit relation has traditionally been solved numerically and the results tabulated, however it is accurate enough and more practical to use the following explicit formula

$$kh = \sqrt{k_0 h} \left[1 + \frac{1}{6} k_0 h + \frac{11}{360} (k_0 h)^2 \right] \quad (2.6)$$

where k_0 is the deep water wave number

$$k_0 = 2\pi/L_0 = 4\pi^3/(gT^2) \quad (2.7)$$

Equation (2.6) is exact in the limit $k_0 h \rightarrow 0$ and the relative error is less than 0.0045 for $k_0 h < 2.5$. In deeper water we recommend the asymptotic expansion.

$$kh = k_0 h (1 + 2e^{-2k_0 h}) \quad (2.8)$$

The two formulae (2.6) and (2.8) cover the whole range $0 < kh < \infty$ with an error of less than 0.45 percent. Relative errors for the two formulae and for a few simpler formulae as well are shown in Figure 2.2. Details about the derivation of equation (2.5) from the linear wave dispersion relation are given by Nielsen (1982).

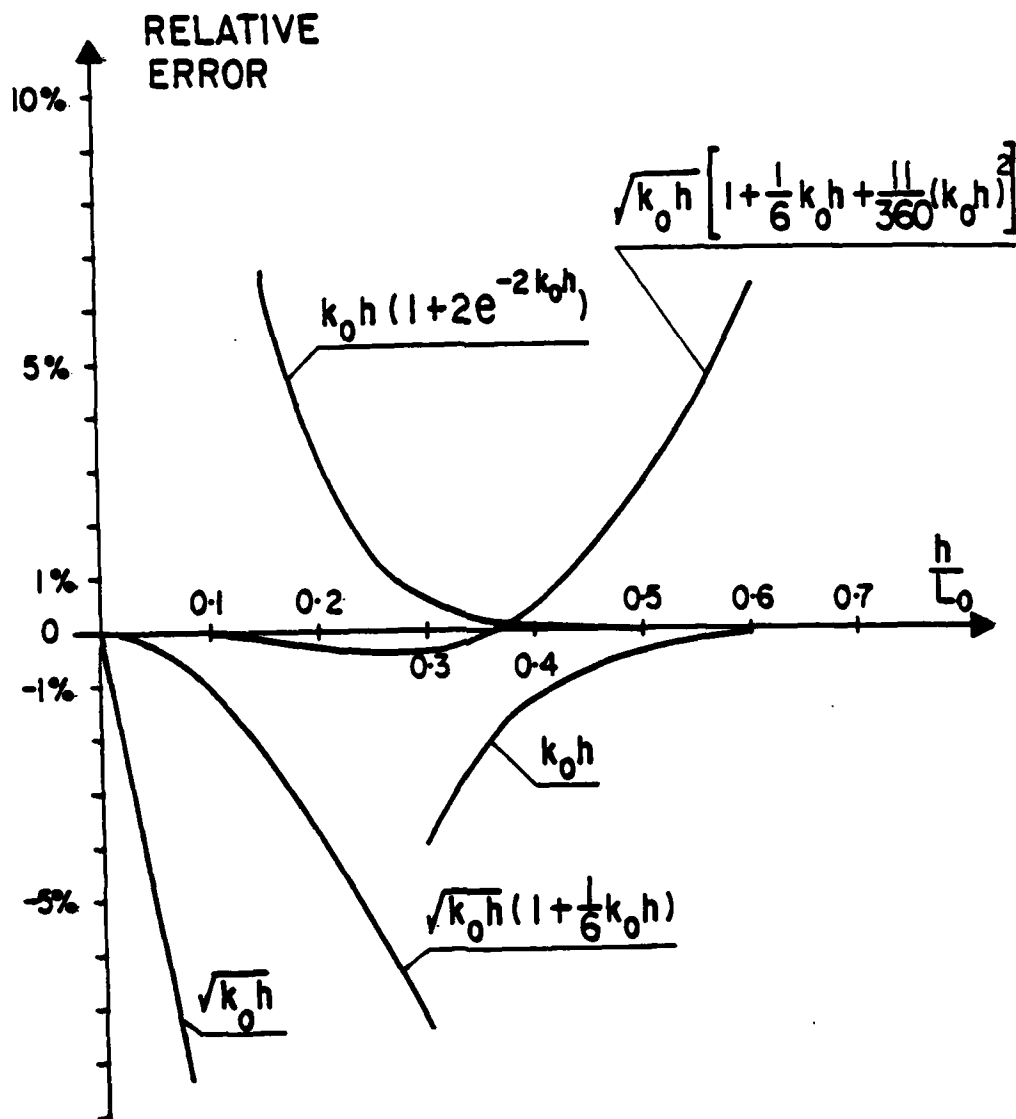


Figure 2.2: Relative error for successive approximations to kh . We see that the formulae (2.6) and (2.8) are much more accurate than the shallow water approximation $\sqrt{k_0 h}$ and the deep water expression $k_0 h$. The two of them together, matched at any value of h/L_0 between 0.3 and 0.4 will cover the whole range with plenty accuracy for practical purposes, ($k_0 h = 2\pi h/L_0$).

WAVE BOUNDARY LAYERS

The wave boundary layer is intuitively defined as the layer close to the bottom, where the wave induced water motion is noticeably affected by the boundary. This layer is normally very thin, i.e. a few millimetres over a smooth, solid bed and a few centimetres over a flat bed of loose sand. Bed forms like ripples will change the structure of the boundary layer by introducing strong rhythmic vortices and the boundary layer over sharp crested ripples will extend to a height of four or five ripple heights or up to about 50 centimetres under field conditions.

It is a typical feature of oscillatory boundary layers that the velocity close to the boundary and the resulting shear stress $\tilde{\tau}(t)$ are ahead of the free flow, $\tilde{u}_\infty(t)$. For laminar flow the shear stress is 45 degrees ahead and for rough turbulent flow it is between 20 and 30 degrees ahead.

The shear stress in a simple harmonic, laminar flow is simple harmonic, but in turbulent flow the variation with time is much more complicated. When the ratio between the bed roughness, r and the semi excursion, a are small, the variation of $\tau(t)$ is still quite smooth and rather like a simple harmonic. This is the case for the measurements of Jonsson and Carlsen (1976) where r/a was only 0.008, see Figure 2.3. For flow over fully developed ripples, the ratio r/a is of the order of magnitude one, and the flow near the bed is dominated by the rhythmic formation and release of strong vortices. Lofquist (1980) measured instantaneous values of $\tilde{\tau}(t)$ under such conditions. Figure 2.4 shows some of his results and we see that the behaviour is completely different from that of a simple harmonic or from that of $\sin(\omega t - \phi)$ or $|\sin(\omega t - \phi)|$ which has

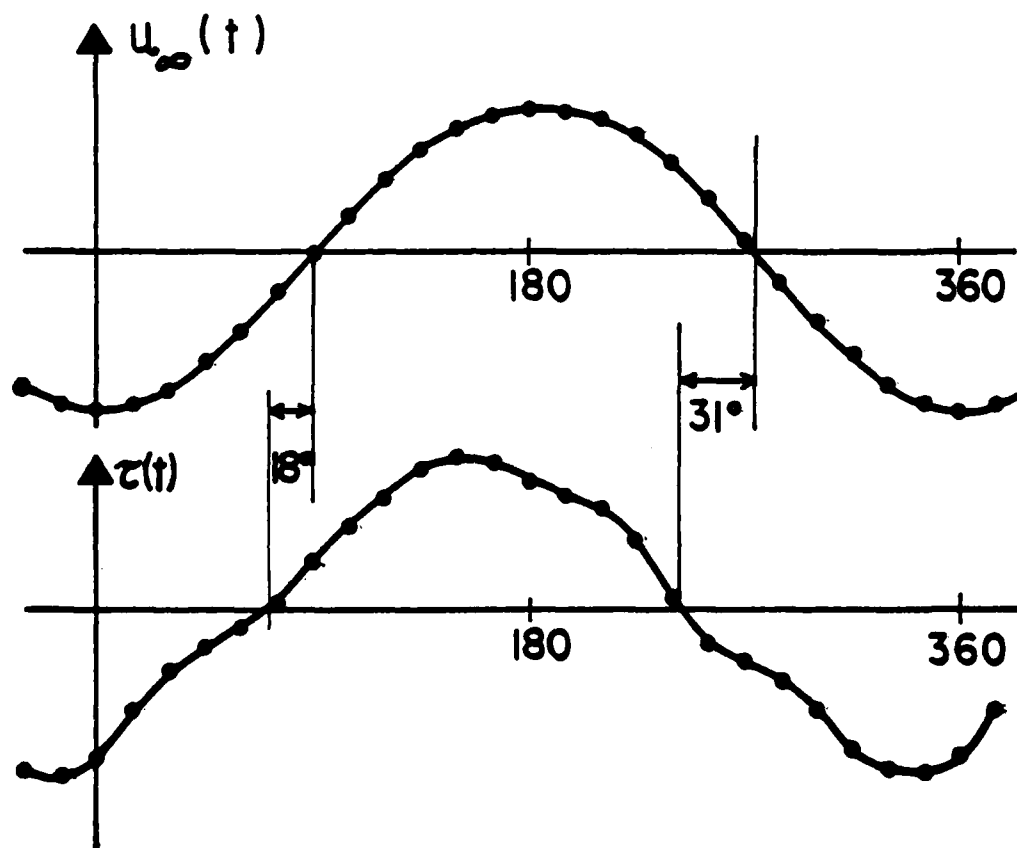


Figure 2.3: Time variations of the bed shear stress $\tau(0,t)$ for rough turbulent flow over relatively small roughness elements $r/a \approx .008$. From Jonsson and Carlsen.

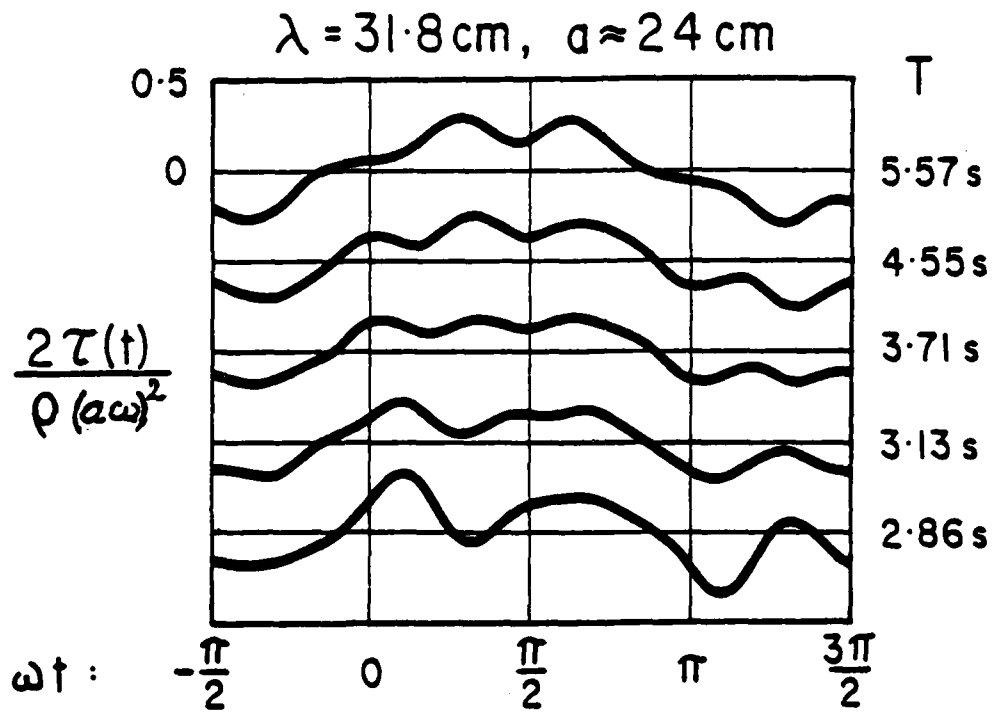


Figure 2.4: Shear stress variation over fully developed ripples, $r/a \approx 0.5$. The free flow $u_\infty(t)$ varies as $\sin \omega t$.

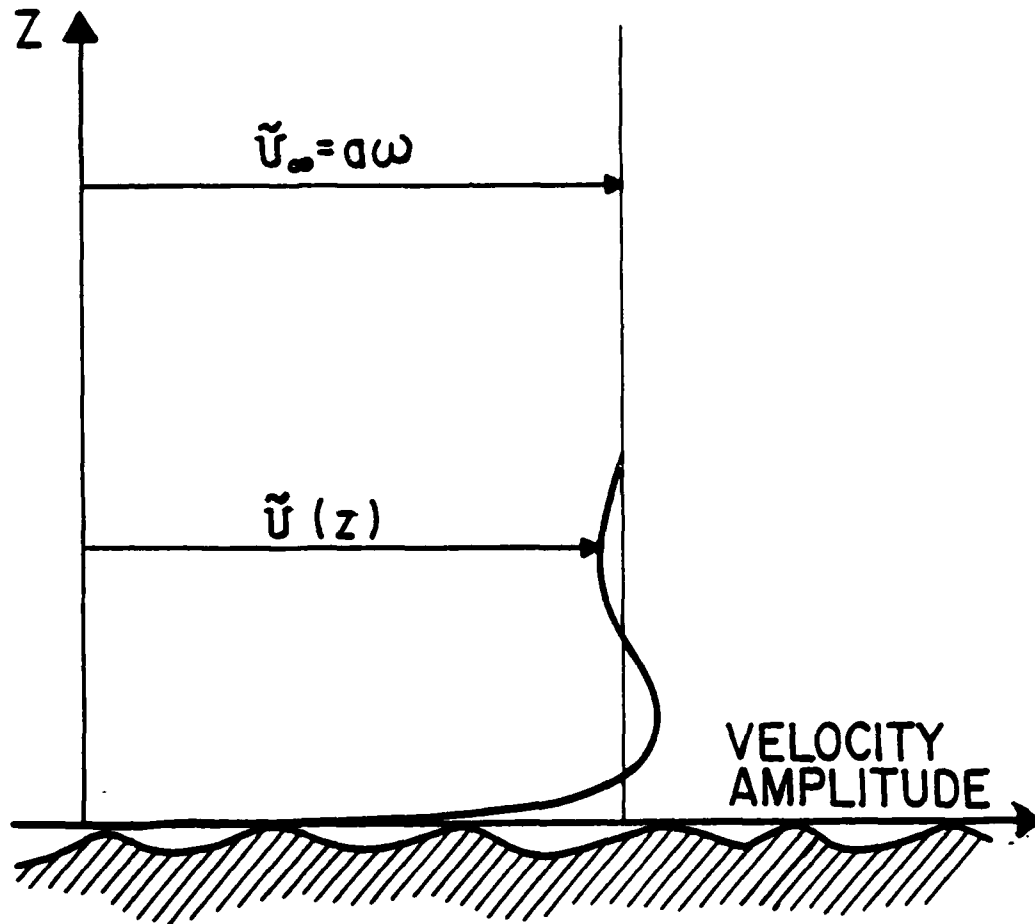


Figure 2.5: The velocity amplitude $\tilde{u}(z)$ oscillates around the free flow value $\alpha \omega$ because the deficit $u_\infty - u$ has the form of a wave, propagating away from the bed.

been assumed in several "theoretical" studies.

Another typical feature of oscillatory boundary layers is the "overshoot" near the bed, which comes about because the velocity deficit $\bar{u}_\infty(t) - \bar{u}(z,t)$ has the nature of a damped wave which alternately adds to and subtracts from the total amplitude $\bar{u}(z)$. See Figure 2.5.

The above mentioned main periodic properties of the oscillatory boundary layers have been studied in great detail by Kalkanis (1957 and 1964), Kamphuis (1975) and Jonsson and Carlsen (1976) on the experimental side and by Kajfura (1968) and Jonsson (1980) on the theoretical or speculative side. Their work is useful for sediment transport studies because they provide predictive formulae for bed shear stresses and boundary layer thicknesses. Those early experimental studies were not however concerned with the details of the turbulence or the vortex motion. Nevertheless, the latter are very important for the understanding of sediment entrainment processes. The formation and strength of lee vortices over large ripples was studied and described by Tunsdall and Inman (1975), who found that the vortices formed twice every period just about the time of velocity extremes in either direction and that the order of magnitude of the maximum velocities in the vortices was $a\omega$.

The turbulence (or velocity fluctuation) intensities over ripples in purely oscillatory flow was studied by Nakato et al (1977) and MacDonald (1977). All of their measurements show that the turbulence intensity as well as the sediment concentrations decay exponentially away from the bed

$$\bar{c}(z) = C_0 e^{-z/\ell_s} \quad (2.9)$$

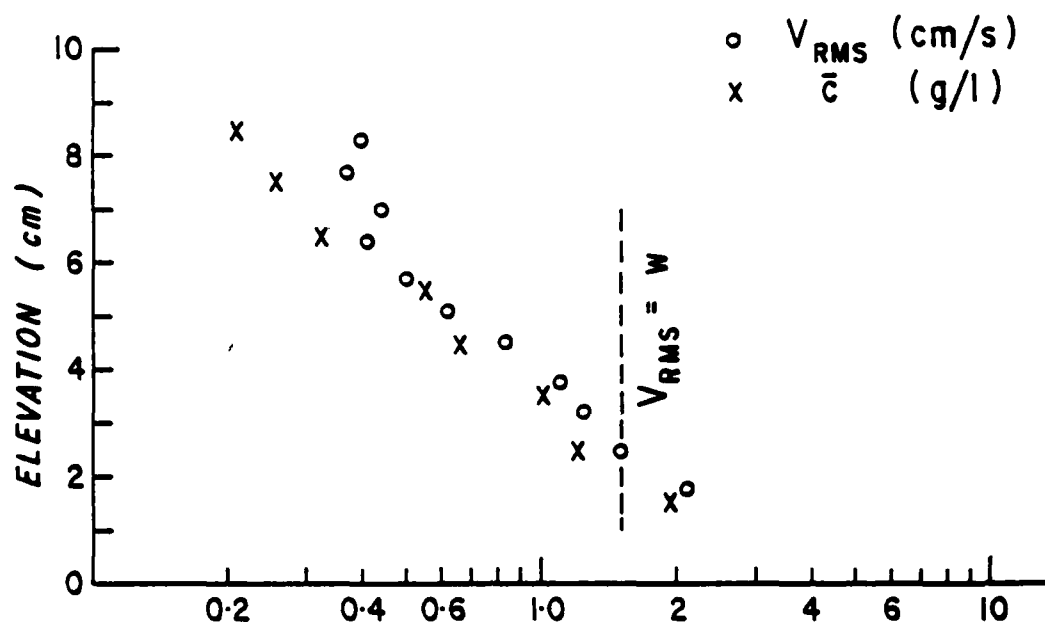


Figure 2.6: Distributions of vertical velocity fluctuations, v_{rms} and time averaged sediment concentrations \bar{c} from MacDonald (1977). Both are exponentially distributed with very similar length scales z_v and z_c . The measurements were taken over a circular swing moving through still water. $T = 6s$, $a = 0.27m$, $w = 0.015m/s$.

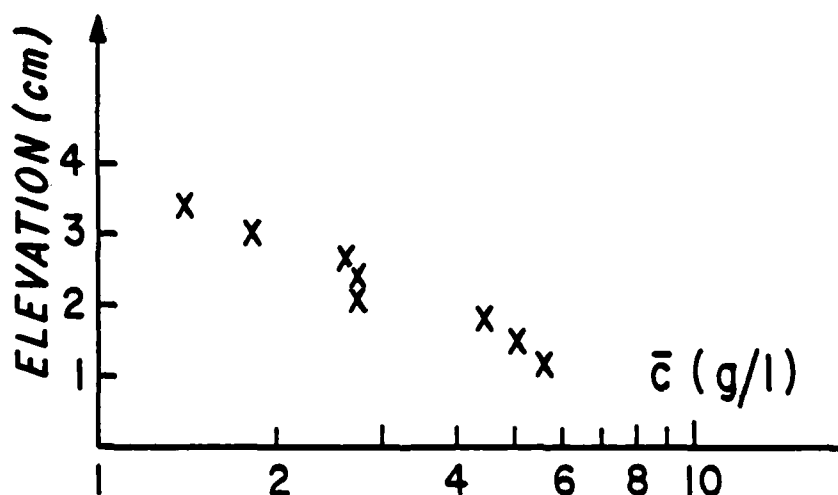


Figure 2.7: Time averaged suspended sediment concentrations \bar{c} from Nakato et. al. (1977), measured over natural ripples in an oscillating water tunnel. $T = 1.8s$, $a = .075m$, $d = .14mm$.

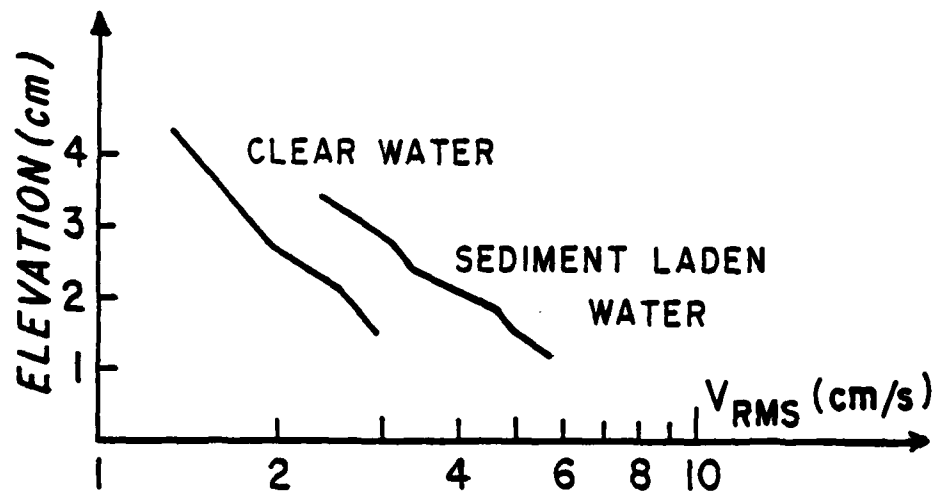


Figure 2.8: Vertical velocity fluctuations v_{rms} from Nakato et. al. (1977), measured over natural ripples and over the same ripples solidified by glue. We see that the presence of loose sand enhances v_{rms} by a factor 2, all other things being equal. Same flow conditions as in Figure 2.7.

$$v_{rms}(z) = v_{rms}(0) e^{-z/l_v} \quad (2.10)$$

and the vertical length scales are very similar. See Figures 2.6 and 2.7. This is a very important observation because it shows that sand and turbulent water spread away from the bed by very similar mechanisms irrespective of the fact that sand has a finite settling velocity, which the turbulent water has not. This is possible because of the way in which sand grains travel in vortex flow. We shall study this in one of the following sections.

Nakato et al's measurements show one more interesting thing about the turbulence intensity over ripples. They show that the intensity is increased by the presence of moving sand, all other things being equal. This is surprising and so far unexplained, but it is consistent with the fact that flat beds of loose sand offer much more resistance to oscillatory flow than flat beds of fixed sand grains (see Figure 2.8), and also with the fact that Bagnold (1946) measured no energy dissipation factors larger than 0.24 over large sharp crested ripples in clear water, while Carstens et al (1969) and Lofquist (1980) observed values in excess of 0.30 in sediment laden water.

QUANTITATIVE DESCRIPTION OF BOUNDARY LAYERS

We shall now try to give a mathematical description of the flow in the wave boundary layer that is, within four or five ripple heights or a few hundred grain diameters from the bed.

We assume that the velocity outside the boundary layer is uniform

in space and varies as a simple harmonic with time

$$u_{\infty} = u_{\infty}(t) = a\omega \cos \omega t \quad (2.11)$$

In order to simplify the mathematical treatment, it is convenient to use the complex formalism

$$u_{\infty}(t) = a\omega e^{i\omega t} \quad (2.12)$$

The complex number $a\omega e^{i\omega t}$ moves around a circle with radius $a\omega$ and angular velocity ω while the real part $a\omega \cos \omega t$ which corresponds to the physical velocity oscillates between $a\omega$ and $-a\omega$ on the real axis, and the imaginary part $i a\omega \sin \omega t$ oscillates between the corresponding values on the imaginary axis, see Figure 2.9.

The equation of motion is

$$\frac{\partial u}{\partial t} = \frac{1}{\rho} \frac{\partial \tau}{\partial z} - \frac{1}{\rho} \frac{\partial p}{\partial x} \quad (2.13)$$

where p is the pressure. This equation is valid both outside and within the boundary layer but outside the boundary layer there are, by definition, no shear stresses in a purely oscillatory flow. We have therefore

$$\frac{\partial u_{\infty}}{\partial t} = - \frac{1}{\rho} \frac{\partial p}{\partial x} \quad (2.14)$$

This expression for the pressure gradient is valid inside the boundary layer as well if the pressure distribution is hydrostatic. That is,

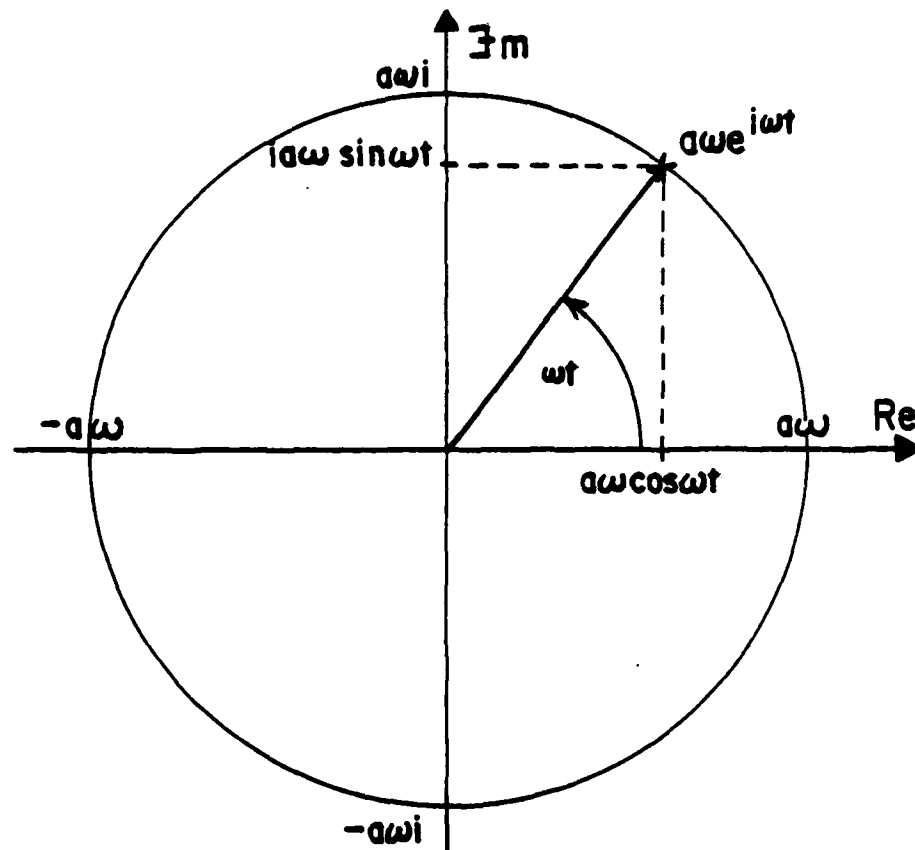


Figure 2.9: The complex velocity $a\omega e^{i\omega t}$ has constant modulus $a\omega$ and moves around a circle with angular velocity ω . The real part $a\omega \cos \omega t$ which represents the physical velocity oscillates between $a\omega$ and $-a\omega$.

if vertical accelerations in the boundary layer are small compared to gravity. In that case equation (2.13) can be written

$$\frac{\partial}{\partial t} (u_{\infty} - u) = - \frac{1}{\rho} \frac{\partial \tau}{\partial z} \quad (2.15)$$

It is convenient now to write the velocity deficit $u_{\infty} - u$ in the form

$$(u_{\infty} - u) = a\omega D(z,t) \quad (2.16)$$

where the non dimensional $D(z,t)$ shown in Figure 2.10, is a complex function which must be equal to $e^{i\omega t}$ at the boundary where the velocity vanishes

$$u(0,t) = 0 \rightarrow D(0,t) = e^{i\omega t} \quad (2.17)$$

At infinity the deficit is of course zero so we also have

$$D(z,t) \rightarrow 0 \text{ for } z \rightarrow \infty \quad (2.18)$$

The deficit function $D(z,t)$ takes a particularly simple form when the bed is smooth and the flow is laminar. For laminar flow the shear stress is proportional to the velocity gradient

$$\tau = \rho \nu \frac{\partial u}{\partial z} \quad (2.19)$$

where ν is the kinematic viscosity of water, so equation (2.15) can

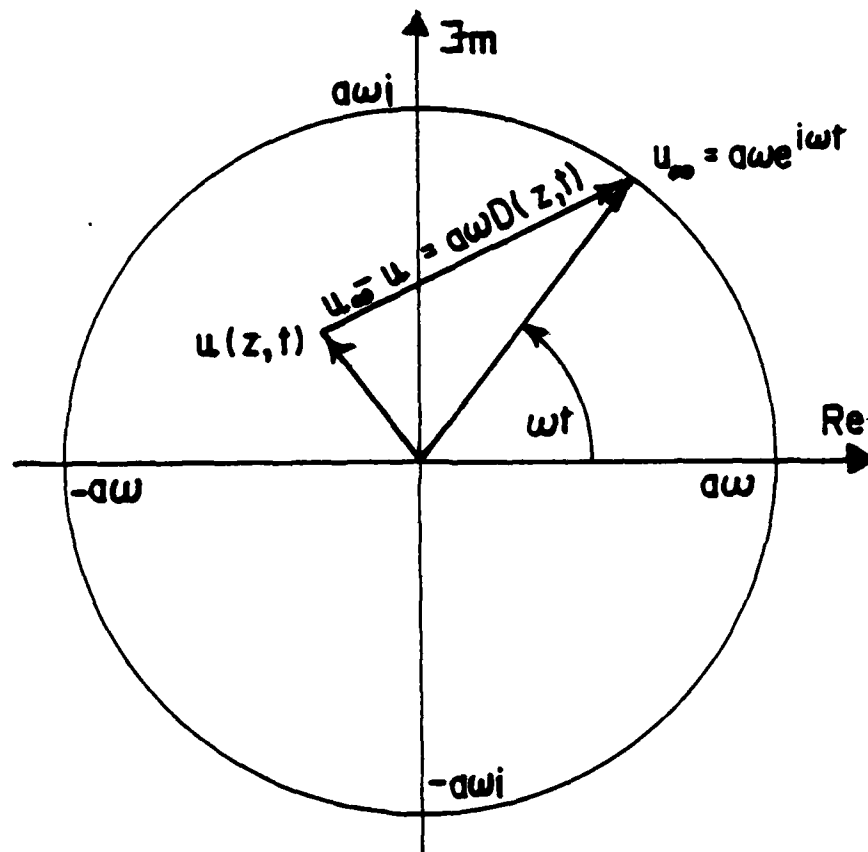


Figure 2.10: The complex velocity deficit $a\omega D(z,t)$ gives the local velocity a different phase as well as the different amplitude from the free flow $u_\infty(t)$.

be written

$$\frac{\partial}{\partial t} [a\omega D(z,t)] = -\frac{1}{\rho} \frac{\partial}{\partial z} \left(\rho v \frac{\partial}{\partial z} [u_{\infty} - a\omega D(z,t)] \right) \quad (2.20)$$

which reduces to

$$\frac{\partial D}{\partial t} = v \frac{\partial^2 D}{\partial z^2} \quad (2.21)$$

We solve this equation by separation of the variables, z and t .

First we notice that the velocity deficit $D(z,t)$ must be periodic

in time like $u_{\infty}(t)$ so we assume the following form

$$D(z,t) = \sum_{n=1}^{\infty} D_n(z) e^{in\omega t} \quad (2.22)$$

which we insert into (2.21) and get

$$in\omega D_n = v \frac{\partial^2 D_n}{\partial z^2} \quad (2.23)$$

This has the solution

$$D_n(z) = A_n e^{\sqrt{in\omega/v} z} + B_n e^{-\sqrt{in\omega/v} z} \quad (2.24)$$

Now since D_n must decrease with increasing z we must have

$$A_n = 0 \text{ for all } n \quad (2.25)$$

which leaves us with

$$u(z,t) = u_{\infty}(t) - \alpha \omega \sum_{n=1}^{\infty} D_n(z) e^{in\omega t} \quad (2.26)$$

$$= \alpha \omega e^{i\omega t} - \alpha \omega \sum_{n=1}^{\infty} B_n e^{-\sqrt{in\omega/\nu} z} e^{in\omega t} \quad (2.27)$$

The velocity must vanish at the bed so we have

$$0 = \alpha \omega e^{i\omega t} - \alpha \omega \sum_{n=1}^{\infty} B_n e^{in\omega t} \quad (2.28)$$

which gives

$$B_1 = 1 \quad (2.29)$$

$$B_n = 0 \quad \text{for } n \neq 1 \quad (2.30)$$

so for laminar flow over a smooth wall we have

$$D(z,t) = D_1(z) e^{i\omega t} = e^{-\sqrt{i\omega/\nu} z} e^{i\omega t} \quad (2.31)$$

and

$$u(z,t) = \alpha \omega [1 - e^{-\sqrt{i\omega/\nu} z}] e^{i\omega t} \quad (2.32)$$

Although laminar flow over a smooth bed is a rather special case, unlikely to occur in nature, the solution (2.31) for this case shows most of the general properties of oscillatory boundary layers.

If we write (2.32) in the form

$$u(z,t) = [1 - D_1(z)] a\omega e^{i\omega t} \quad (2.33)$$

we can see how $D_1(z)$ determines the local amplitude and phase relative to the free flow.

We see that when $D_1(z)$ is a real, negative number, the velocity is in phase with $u_\infty(t)$ and the amplitude is larger than $a\omega$. That is, there are elevations where the velocities get larger than those of the free flow.

Remembering the form of D_1 ,

$$D_1(z) = e^{-\sqrt{i\omega/V} z} = e^{-\sqrt{\omega/2V} (1+i) z} \quad (2.34)$$

or

$$D_1(z) = e^{-\sqrt{\omega/2V} z} \left[\cos \sqrt{\omega/2V} z - i \sin \sqrt{\omega/2V} z \right] \quad (2.35)$$

we see that this occurs for

$$\sqrt{\frac{\omega}{2V}} z = p\pi, \quad p = 1, 3, 5, \dots \quad (2.36)$$

Figure 2.11 a & b show the position of $D(z)$ and of $1-D(z)$ in the complex plane. Figure 2.11c shows the position of $u(z,t)$ in the complex plane and Figure 2.11d shows the variation of the velocity amplitude $U(z)$ with the non dimensional elevation, $z\sqrt{\omega/2V}$.

The general picture of the velocity variation is the same for

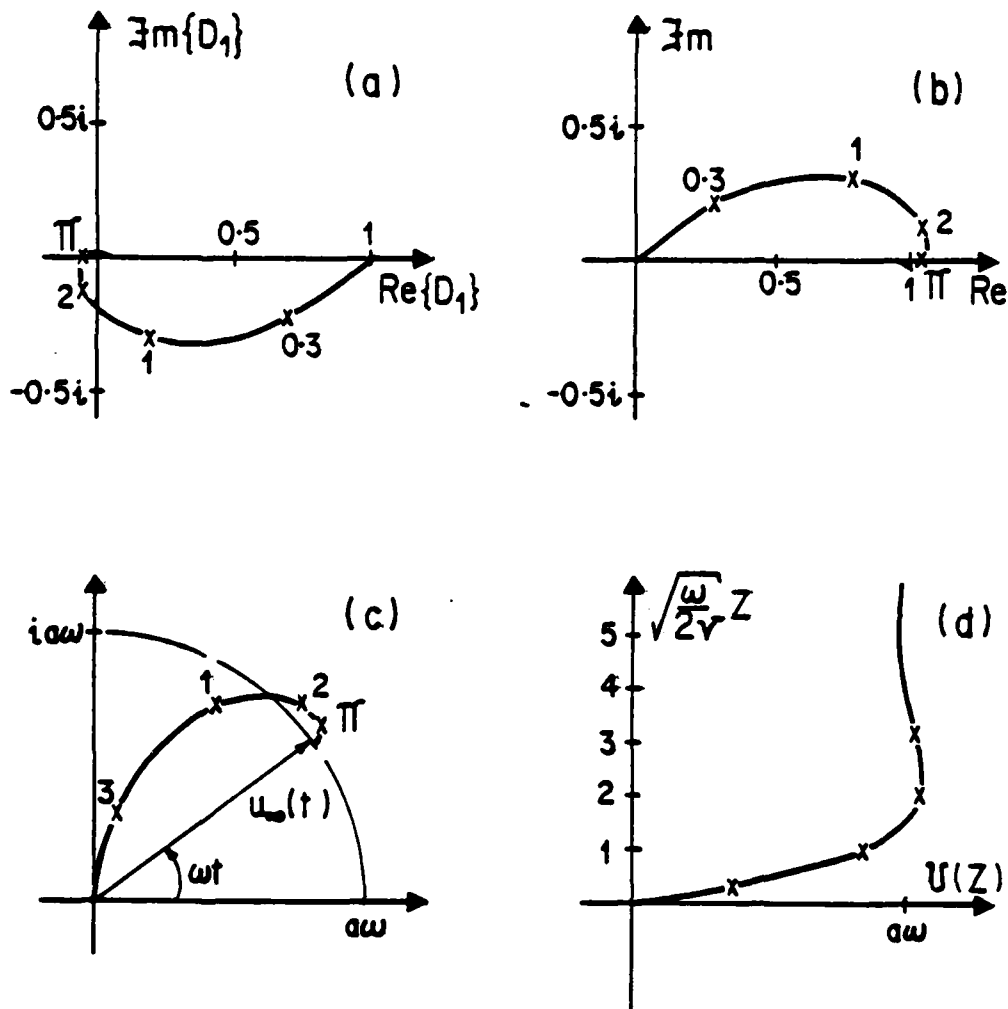


Figure 2.11: Velocity variations with elevation in oscillatory laminar flow over a smooth wall.

- a: The deficit function $D(z,t)$ moves along a logarithmic spiral starting at 1 and approaching 0 as z increases. Numbers on the curves refer to the non dimensional elevation $\sqrt{\omega/2\nu}z$.
- b: Corresponding variation of $1-D_1(z)$ which is the ratio between $u(z,t)$ and $u_\infty(t)$ see equation (2.33).
- c: In the simple case of laminar flow over a smooth wall where $u(z,t)$ is simple harmonic ($u(z,t) = \omega(1-D_1(z))e^{i\omega t}$), we can construct $u(z,t)$ geometrically by using the circle from figure 2.9 and the spiral of figure 2.11b).
- d: The variation of the velocity amplitude $U(z) = \omega|1-D_1(z)|$ with elevation.

turbulent flow with small roughness to semi excursion ratios ($r/a \lesssim 0.1$) as shown by Jonsson (1980). Again the path of $D_1(z)$ in the complex plane is a spiral which starts at 1 for $z = 0$ and approaches zero quickly as z grows. The expression (2.34) shows that for laminar flow over a smooth boundary, the complex logarithm of $D_1(z)$ is a particularly simple function of z :

$$\ln D_1 = -(1 + i) \sqrt{\omega/2\nu} z \quad (2.37)$$

and that the angle $\text{Arg}(D_1)$ and the logarithm of the modulus $\ln |D_1|$ are identical:

$$\text{Arg}(D_1) = \ln |D_1| = -\sqrt{\omega/2\nu} z \quad (2.38)$$

Kalkanis' (1964) measurements show that for turbulent flow over a smooth wall the relation is

$$\text{Arg}(D_1) \approx 1.2 \ln |D_1| \quad (2.39)$$

and both increase as $z^{0.3}$ approximately. See Figure 2.12. For flow over two dimensional roughness the pattern is different again.

Figure 2.13 shows experimental data from Kalkanis (1964), where the bed roughness was made up by half cylinders. Figure 2.14 shows data from Jonsson and Carlsen (1976) who worked with considerably larger Reynolds numbers than Kalkanis, and with a different type of two dimensional roughness elements.

The data plotted in Figures 2.12 through 2.14 show some variations in behaviour, however a general feature is that $\ln D_1$ behaves very

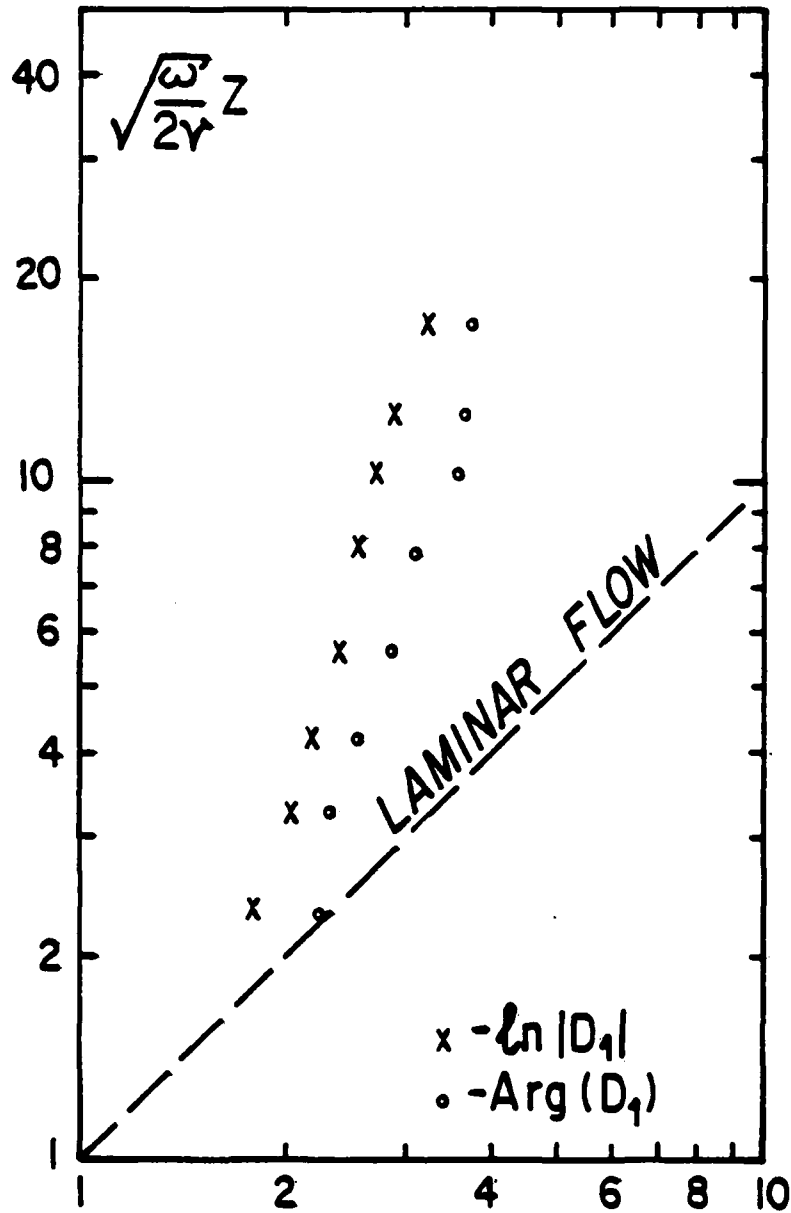


Figure 2.12: Variation of $\ln D_1$ for turbulent flow over a smooth wall. Kalkanis (1964), Run 105, $T = 1.4s$, $a = .25m$.

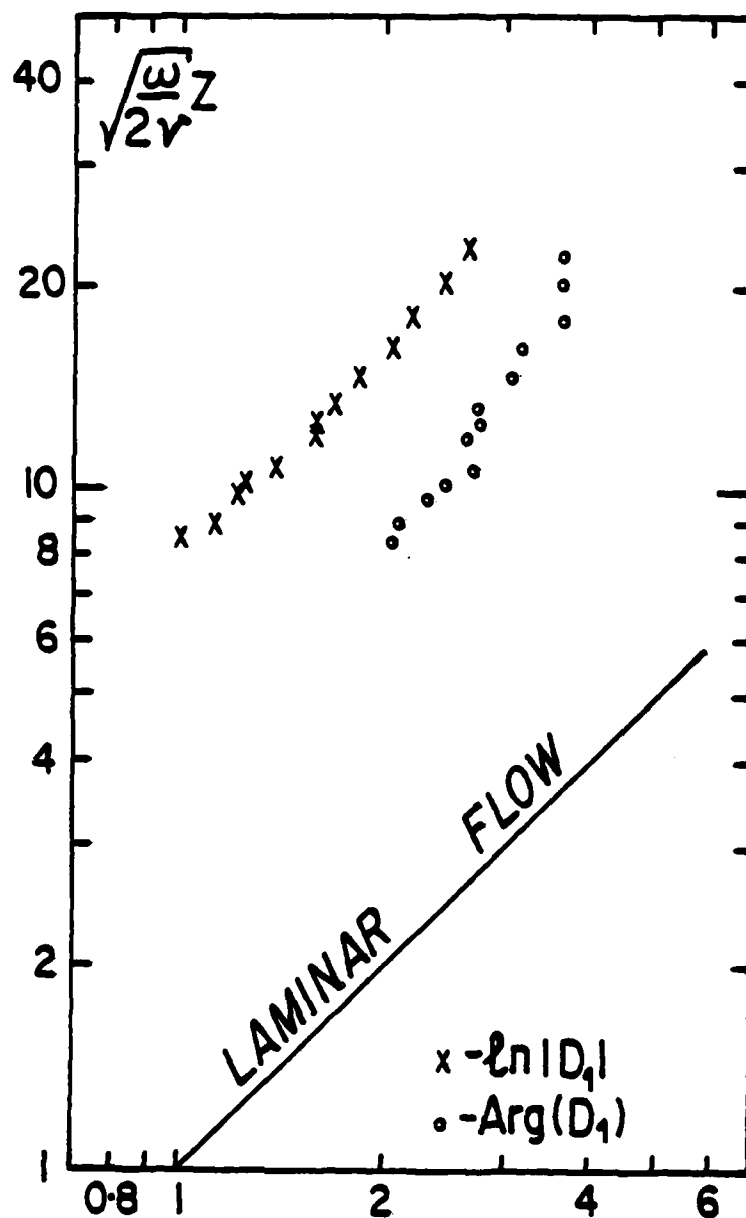


Figure 2.13: Variation of $\ln D_1$ for flow over two dimensional roughness elements. Kalkanis (1964), Run 224, $T = 1.4s$, $a = .15m$, Jonsson (1980) estimates that the roughness in Kalkanis experiments was equal to the radius of Kalkanis' roughness cylinders, for this experiment : $r = .010m$.

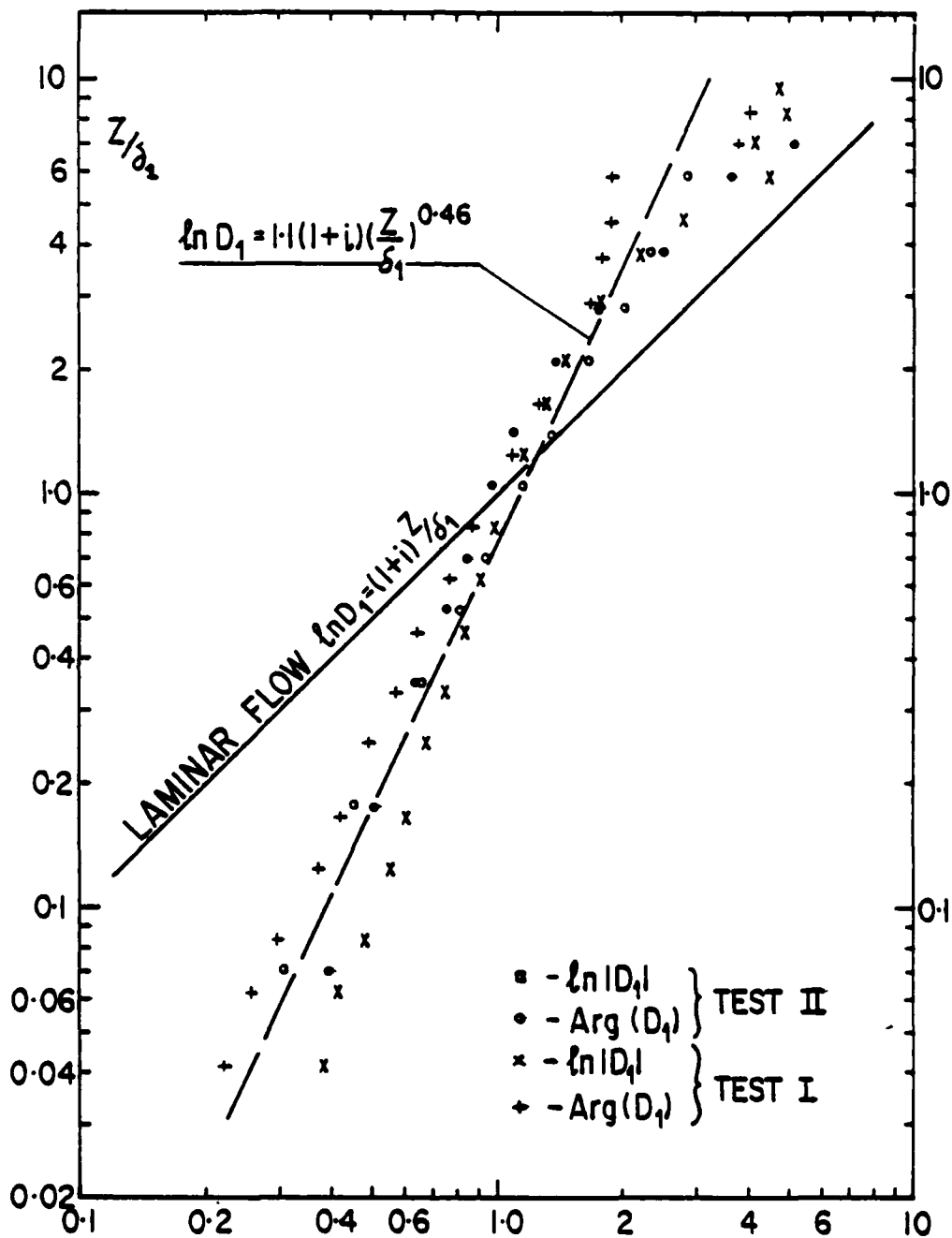


Figure 2.14: Variation of $\ln D_1$ for rough turbulent flow. Measurements from Jonsson and Carlsen (1976). The values obtained above $z/\delta_1 = 5$ are probably unreliable. The scaling length δ_1 is the real displacement thickness defined in equations (2.59) through (2.61).

similarly and that both $\text{Arg}(D_1)$ and $\ln|D_1|$ can be determined by one power function throughout the whole experimental range. This is interesting because all of the theoretical (or speculative) models, eg. Kajiura (1968) and Jonsson (1980) work with two or more layers where the behaviour of D_1 is expected to be different.

We shall not however, go deeper into the study of the details of $u(z,t)$ at the moment. Instead we will consider another measurable feature of the boundary layer, namely the bed shear stress $\tau(0,t)$, and show how the empirical information on τ can be used to predict vertical length scales in the boundary layer. This is important because we need the vertical length scales for prediction of suspended sediment distributions and the only detailed empirical information about the boundary layer over natural sand beds (Carstens et. al. 1969 and Lofquist 1980) are obtained by friction or energy dissipation measurements, without detailed velocity measurements.

We start again with the equation of motion

$$\frac{\partial}{\partial t} (u_\infty - u) = - \frac{1}{\rho} \frac{\partial \tau}{\partial z} \quad (2.15)$$

which we integrate with respect to z and get

$$\frac{\partial}{\partial t} \int_0^\infty (u_\infty - u) dz = \frac{1}{\rho} [\tau(0,t) - \tau(\infty,t)] \quad (2.40)$$

The term $\tau(\infty,t)$ can be neglected since the shear stresses vanish outside the boundary layer, so we have

$$\frac{\partial}{\partial t} \int_0^{\infty} (u_{\infty} - u) dz = \frac{1}{\rho} \tau(0, t) \quad (2.41)$$

which shows that the instantaneous bed shear stress is proportional to the total acceleration deficit.

Since both the velocity deficit $u_{\infty} - u$ and the bed shear stress $\tau(0, t)$ must be periodic with period T we may write both as a Fourier expansion

$$u_{\infty} - u = a\omega \sum_1^{\infty} D_n(z) e^{in\omega t} \quad (2.42)$$

$$\tau(0, t) = \rho(a\omega)^2 \sum_1^{\infty} C_n e^{in\omega t} \quad (2.43)$$

After introduction of these and cancellation of common factors, the integrated equation of motion, (2.41), becomes

$$in\omega \int_0^{\infty} D_n(z) dz = a\omega C_n \quad (2.44)$$

We are particularly interested in the fundamental mode ($n = 1$) for which we get

$$i \int_0^{\infty} D_1(z) dz = a C_1 \quad (2.45)$$

The integral

$$\Delta_1 = i \int_0^{\infty} D_1(z) dz \quad (2.46)$$

is the complex displacement thickness of the fundamental mode of the velocity, so equation (2.45) enables us to determine a vertical length scale for the boundary layer if we know the bed shear stress and vice versa.

We shall illustrate this by looking once more at the special case of smooth laminar flow where we have found

$$D_1(z) = e^{-\sqrt{i\omega/\nu} z} \quad (2.34)$$

for which

$$\Delta_1 = i \int_0^{\infty} D_1(z) dz = \sqrt{i\nu/\omega} \quad (2.47)$$

and thus from (2.45):

$$C_1 = \sqrt{i\nu/a^2\omega} \quad (2.48)$$

so the bed shear stress in smooth laminar flow is given by

$$\tau(o,t) = \rho (a\omega)^2 \sqrt{i\nu/a^2\omega} e^{i\omega t} \quad (2.49)$$

The fact that the argument of C_1 is $\pi/4$ means that the bed shear stress leads the free flow $u_{\infty} = a\omega \exp[i\omega t]$ by $\pi/4$ or 45 degrees. The result (2.49) could of course also have been obtained from the definition (2.19) together with (2.34).

Several authors, starting with Jonsson (1966) describe the bed shear stress in terms of the wave friction factor f_w defined by

$$\tau_{\max} = \frac{1}{2} \rho f_w (a\omega)^2 \quad (2.50)$$

Normally f_w will include contributions from the higher harmonics (equation 2.43)

$$\frac{1}{2} f_w = \text{Max} \left\{ \sum_{n=0}^{\infty} C_n e^{in\omega t} \right\} \quad (2.51)$$

and there is no simple relation between f_w and C_1 . However for smooth laminar flow where only C_1 is non-zero we have

$$\frac{1}{2} f_w = |C_1| \quad (2.52)$$

and thus

$$f_w = 2\sqrt{\nu/a^2\omega} \quad (2.53)$$

While (2.52) only holds for smooth laminar flow we can find a similar relation for the energy dissipation coefficient: f_e , which holds as long as the free flow is simple harmonic ($u_\infty(t) = a\omega \exp[i\omega t]$).

The average rate of energy dissipation per unit area over one period is

$$E = \overline{u_\infty(t) \tau(0,t)} \quad (2.54)$$

see eg. Kajiura (1968). Since $u_\infty(t)$ is assumed simple harmonic, only the fundamental mode of the shear stress will contribute to the average

$$E = \overline{\text{Re} \{ a\omega e^{i\omega t} \}} \text{Re} \{ \rho(a\omega)^2 C_1 e^{i\omega t} \} \quad (2.55)$$

$$E = \frac{1}{2} \rho(a\omega)^3 \text{Re} (C_1) \quad (2.56)$$

The traditional way of describing the energy dissipation is in terms of the energy dissipation factor f_e , defined by

$$E = \frac{2}{3\pi} \rho f_e (a\omega)^3 \quad (2.57)$$

which is related to C_1 by

$$f_e = \frac{3\pi}{4} \text{Re} \{ C_1 \} \quad (2.58)$$

As mentioned above, most of the existing empirical data on oscillatory boundary layers over natural sand beds consist of friction or energy dissipation measurements, so we can predict f_e or $\text{Re} \{ C_1 \}$ reasonably well using those data.

In order to utilize the same data for the prediction of vertical length scales in the boundary layer, we now look for one which is directly related to f_e or $\text{Re} \{ C_1 \}$. Equation (2.45) shows that what we are looking for is

$$\delta_1 = \text{Re} \left\{ i \int_0^\infty D_1(z) dz \right\} \quad (2.59)$$

which is related to C_1 by

$$\delta_1 = \alpha \text{Re} \{ C_1 \} \quad (2.60)$$

and to f_e via (2.58)

$$\delta_1 = \frac{4}{3\pi} f_e a \quad (2.61)$$

PREDICTION OF f_e , f_w and δ_1

Both the wave friction factor and the energy dissipation factor will in general depend on the flow Reynolds number, $a^2\omega/\nu$, as well as on the roughness to semi excursion ration, r/a ; but when the flow is rough turbulent, as is the case under field conditions we can neglect the Reynolds number dependence. The hydrodynamic conditions of most wave flume experiments are in the region of transition between laminar and turbulent flow, see Jonsson (1966). For such conditions there is no empirical data (known to the author) about friction factors over natural sand beds. The following derivations are therefore restricted to rough turbulent flow conditions.

The wave friction factor f_w and the energy dissipation factor f_e are theoretically different and may indeed take very different values under some conditions (Figure 2.15). The differences are however, usually small compared to the scatter in the empirical data. Therefore it is not really worth while to distinguish between f_e and f_w for predictive purposes.

In the following we will make use of data from Kamphuis (1975) who measured shear stresses, and thus f_w , over fixed sand beds, from Carstens et. al. (1969) who measured energy dissipation ($\approx f_e$) over natural sand beds, and from Lofquist (1980) who measured both, over natural rippled sand beds. The differences between f_e and f_w are illustrated by Lofquist's data in Figure 2.15. Only two experiments show a significant deviation corresponding to a particularly peaked

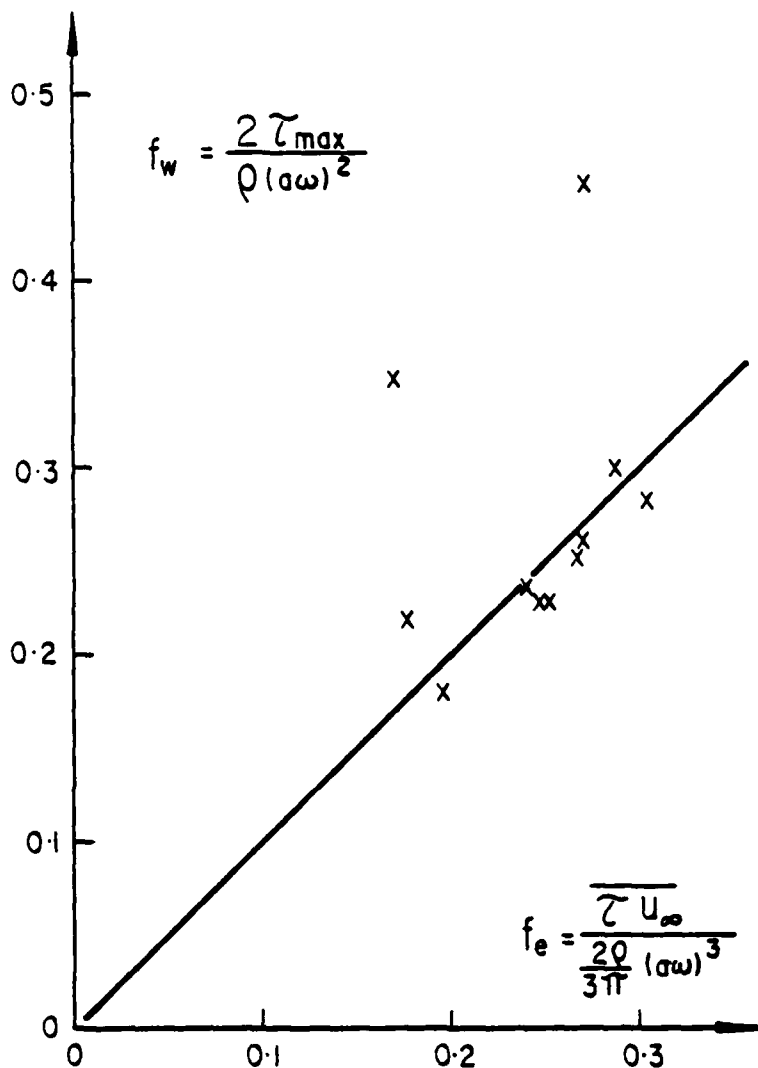


Figure 2.15: Comparison of measured values of f_w and f_e from Lofquist (1980). We see that f_w and f_e are generally nearly equal. The few extreme deviations stem from experiments where $\tau(t)$ has a pronounced, narrow peak.

variation of $\tau(t)$. The particular experimental conditions that lead to such behaviour are as yet unknown, but they may become clear with the progression of Lofquist's work.

Prediction of f_e for rough turbulent oscillatory flows involves two steps, namely, estimations of the hydraulic roughness, r , of the

bed and determination of f_e from

$$f_e = \begin{cases} \exp [5.213 (\frac{r}{a})^{1.9} - 5.977] & \text{for } \frac{r}{a} < .63 \\ 0.30 & \text{for } \frac{r}{a} \geq .63 \end{cases} \quad (2.62)$$

Equation (2.62) which corresponds to the flow model, suggested by Jonsson and Carlsen (1976) is only one of several semi empirical formulae of the upper limit of 0.3 is somewhat arbitrary. It is also doubtful whether all of the underlying physical assumptions, such as the existence of an overlap layer (a layer where the shear stress is proportional to the distance from the bed and the velocity gradient) are met by the flow over large natural sand ripples. We will, however, use equation (2.62) indiscriminately with all the experimental data from Carstens et al (1969) and Lofquist (1980) and not claim that the resulting predictive formulae are anything but empirical.

The bed roughness, r , depends on the bed form geometry, sand grain size and on the motion of sandgrains near the sand-water-interface. The simplest case is that of the flat bed with no sediment motion. Kamphuis (1975) measured friction factors under such conditions. Figure 2.16 shows that his results are well predicted by equation 2.62) with

$$r = 2.5\bar{d} \quad (2.63)$$

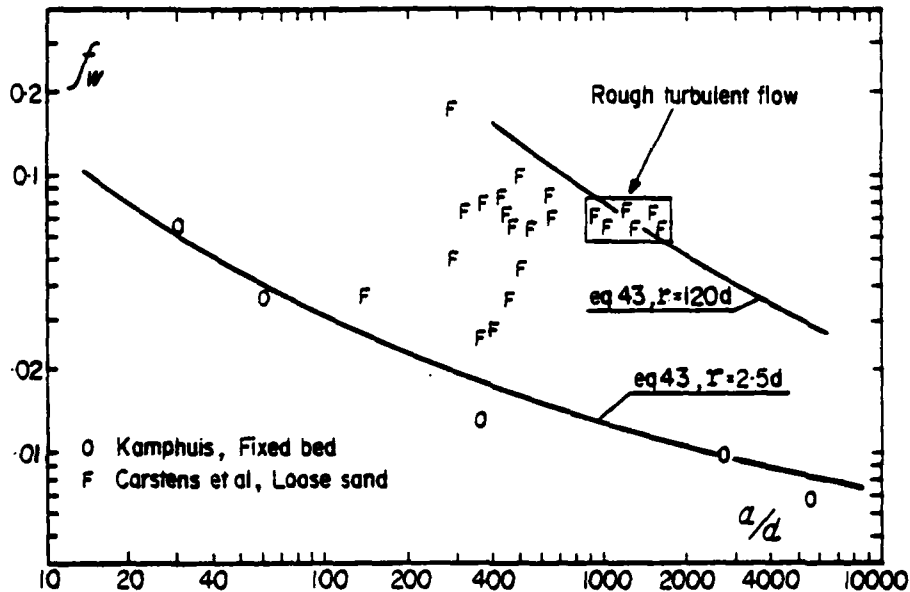


Figure 2.16: Friction factors measured over flat beds of fixed and loose sand. The moving sand over a loose bed will increase the roughness by one or two orders of magnitude, depending on the intensity of the sediment motion.

When the sand is allowed to move, the friction is increased very considerably, see Figure 2.16. Grant and Madsen (1982) suggested that the roughness contribution from moving sand be given by

$$\frac{r}{d} = 160 \theta_c (\sqrt{\theta'} - 0.7 \sqrt{\theta'_c})^2 \quad (2.64)$$

which is based on the mechanics of sand saltation in air. It is reasonable to expect r to be a function of the skin friction Shields parameter θ' . However, the form of (2.64) seems not to work too well for the data of Carstens et. al. (1969), see Figure 2.17. The expression (2.64) varies essentially as θ' , where as the data indicate a slower growth, more like $\sqrt{\theta'}$ for $\theta' > 0.1$.

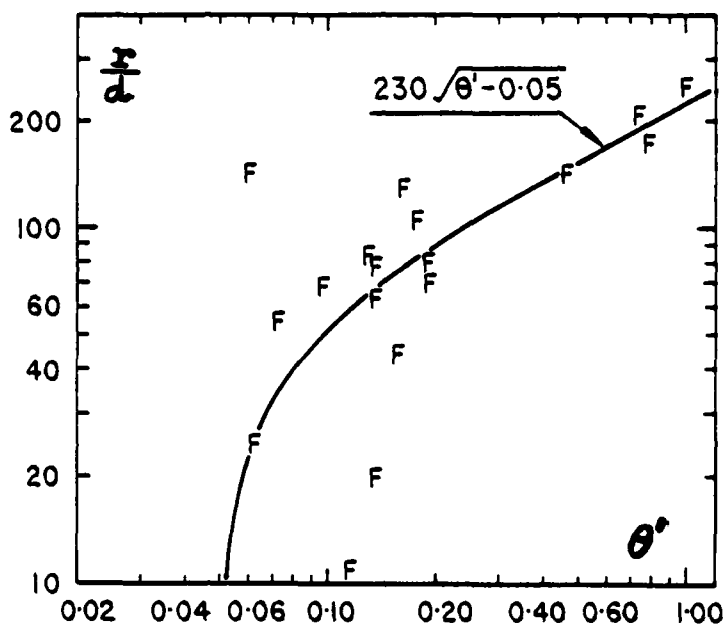


Figure 2.17: Observed roughness (via equation 2.62) for flat beds of loose sand. Measurements by Carstens et. al. (1969).

When the bed is covered by ripples, these will contribute to the roughness as well. Grant and Madsen argue that as a first approximation, this contribution should be proportional to the ripple height η and the steepness η/λ

The equation

$$r = 8 \eta^2 / \lambda + 190 \sqrt{\theta' - 0.05} d \quad (2.65)$$

provides a good fit to all the experimental data from Carstens et. al. (1969) and Lofquist (1980). See Figure 2.18.

The skin friction Shields parameter θ' expresses the ratio between the moving shear force ($\sim \tau d^2$) and the stabilizing gravity force ($\sim \rho g (s - 1) d^3$). It may be estimated by

$$\theta' = \frac{\frac{1}{2} f_w' (\omega)^2}{(s-1)g d} \quad (2.66)$$

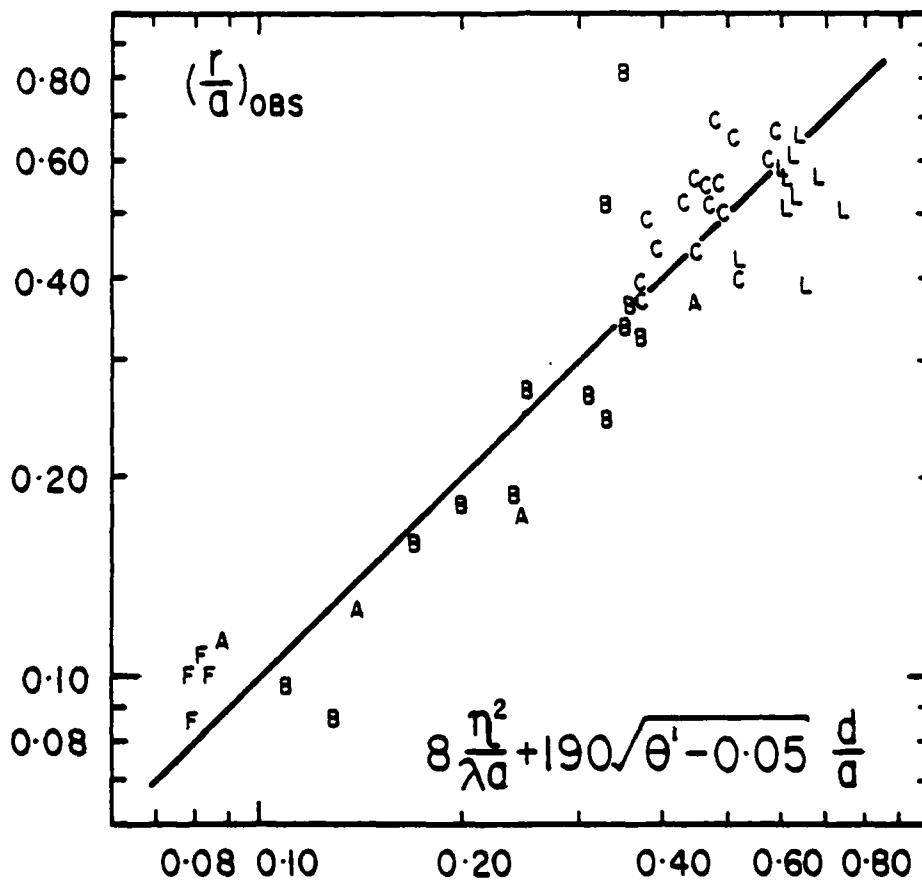


Figure 2.18: Predicted (eq. 2.65) and observed (via eq. 2.62) values of r/a for the energy dissipation measurements of Carstens et. al. (1969) A: rippled bed, $d = .19\text{mm}$. B: rippled bed, $d = .30\text{mm}$. C: rippled bed, $d = .59\text{mm}$. F: flat bed, $d = .30\text{mm}$ and from Lofquist (1980), L: rippled bed, $d = .55\text{mm}$. The straight line corresponds to perfect agreement between prediction and observation. The corresponding f_b values will be in closer agreement because f_b varies slowly with r/a .

where f'_w is calculated from (2.62) using the roughness of a flat bed of fixed grains: $r = 2.5\bar{d}$, s is the relative density of the sand and g is the acceleration of gravity.

For prediction of the ripple geometry under field conditions, one may use

$$\eta/\lambda = 0.342 - 0.34 \sqrt{\theta'} \quad \text{for } \theta' < 1 \quad (2.67)$$

$$\eta/\alpha = 21 \left(\frac{(\alpha \omega)^2}{(s-1) g d} \right)^{-1.85} \quad (2.68)$$

as suggested by Nielsen (1981). When $\theta' > 1$, the ripple height should be taken as zero.

TURBULENCE STRUCTURE OF WAVE BOUNDARY LAYERS

The turbulence structure of oscillatory boundary layers can be observed in different ways. Indirectly by determinations of the eddy viscosity ν_T from velocity measurements

$$\nu_T = \frac{\tau}{\rho \frac{\partial u}{\partial z}} = \frac{\frac{\partial}{\partial t} \int_z^\infty (u - u_\infty) dz}{\frac{\partial u}{\partial z}} \quad (2.69)$$

as done by Horikawa and Watanabe (1968), Lundgren (1972), Jonsson and Carlsen (1976), or by direct measurement of the vertical velocity fluctuations (v_{rms}) as done by Nakato et. al. (1977), MacDonald (1977), Kemp and Simons (1982) and Du Toit and Sleath (1981).

Local eddy viscosities determined by (2.69) taking $\tau(z,t)$ and $u(z,t)$ as the real physical quantities show a strong variation with time, which is at first sight quite astonishing. It behaves like $-\tan(\omega t)$, and tends to minus and plus infinity on either side of two vertical asymptotes during each wave cycle, see Figure 2.19. The asymptotes are of course at the phases where the velocity gradient is zero. Now the eddy viscosity is normally

interpreted as the product of a typical turbulent velocity and a typical length

$$v_T = v_v l_v \quad (2.70)$$

It is not physically meaningful however, to interpret the infinite or negative values of v_T as a result of the negative velocity - or length scales. The alternative is to interpret v_T as a complex number which has a constant modulus

$$|v_T| = v_v l_v \quad (2.71)$$

and an argument ϕ , which is equal to the phase difference between

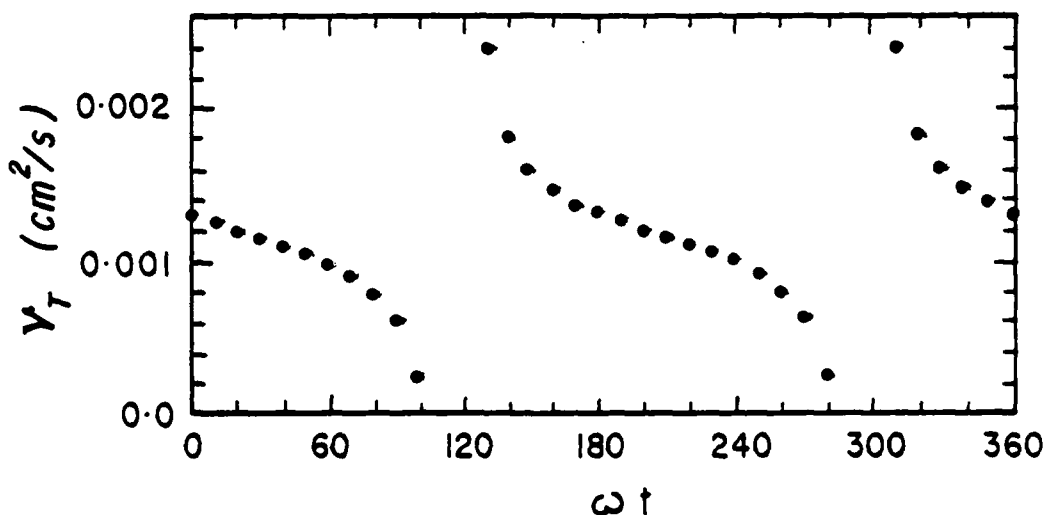


Figure 2.19: Eddy viscosities from Horikawa and Watanabe (1968), obtained as instantaneous ratios between shear stress and velocity gradients. The vertical asymptotes are at the phases where the velocity gradient is zero.

shear stress and velocity gradient. If both the shear stress $\tau(z,t)$ and the velocity gradient $\frac{\partial u}{\partial z}$ vary as simple harmonics with time we may describe them by the real parts of the following complex functions.

$$\frac{\partial u}{\partial z} = U'(z) e^{i\omega t} \quad (2.72)$$

$$\tau = \tau(z) e^{i(\omega t + \phi)} \quad (2.73)$$

where U is the local velocity amplitude and the prime denotes differentiation with respect to z and $\tau(z)$ is the local shear stress amplitude. The corresponding complex eddy viscosity is

$$v_T = \frac{\tau/\rho}{\frac{\partial u}{\partial z}} = \frac{\tau(z)}{\rho U'(z)} e^{i\phi} \quad (2.74)$$

which is a complex *constant* (for fixed z) with modulus

$$|v_T| = \frac{\tau(z)}{\rho U'(z)} \quad (2.75)$$

and argument ϕ .

In contrast, an apparently time dependant eddy viscosity results if we take the ratio of the real parts of (2.72) and (2.73):

$$v_T = \frac{\text{Re} \{ \tau(z) e^{i(\omega t + \phi)} \}}{\rho \text{Re} \{ U'(z) e^{i\omega t} \}} \quad (2.76)$$

$$= \frac{\tau(z) \cos(\omega t + \phi)}{\rho U'(z) \cos \omega t} \quad (2.77)$$

$$= \frac{\tau(z)}{\rho U'(z)} [\cos \phi - \sin \phi \tan \omega t] \quad (2.78)$$

which describes the curves shown in Figure 2.19.

The fact that the apparent eddy viscosities measured by Horikawa and Watanabe approach the asymptotes from the left through negative values means that $\sin \phi$ is positive (see equation 2.78) and thus that the argument ϕ of the complex eddy viscosity is positive. For the experiments of Jonsson and Carlsen (1976), ϕ is always less than about 5 degrees and mostly positive, but for flow over fully developed sand ripples it might be larger and more variable due to the strong vortices which may cause a substantial momentum transfer (= shear stress) even when the velocity gradient is zero.

Lundgren (1972) derived the magnitude $|v_T(z)|$ from the measurements subsequently published by Jonsson and Carlsen (1976) and recommended the following formula for prediction of $|v_T|$.

$$|v_T| = \frac{\kappa u_* z}{1 + 1.34 \sqrt{f_w} \frac{z}{\delta} \exp[\frac{z}{\delta}]} \quad (2.79)$$

where the boundary layer thickness, δ , is defined as the lowest elevation where the velocity amplitude equals that of the free flow ($U(\delta) = \alpha \omega$). Following (2.79) $|v_T|$ will increase linearly with z for $z \ll \delta$ and decrease exponentially with z for $z \gg \delta$. Figure 2.20 shows a somewhat different expression

$$v_T = \frac{0.4 u_* z}{1 + 0.2 \frac{z}{\delta_1} \exp \frac{z}{1.6\delta_1}} \quad (2.80)$$

which uses the displacement length δ_1 for scaling, because it is predictable on the basis of Carstens et.al.'s and Lofquist's energy dissipation measurements over natural sand beds.

Figure 2.20 also shows measured vertical velocity fluctuations, from Nakato et. al. and MacDonald. We see that v_{rms} decays exponentially like $|v_T|$ for $z \geq \delta_1$ but at a somewhat slower rate:

$$v_{rms} \approx 0.9 u_* e^{-z/4.5\delta_1} \quad \text{for } z \geq \delta_1 \quad (2.81)$$

For $z \leq \delta_1$, v_{rms} is nearly constant at least half way down to the bottom of the ripple trough ($z = -\eta$).

$$v_{rms} \approx 0.65 u_* \quad \text{from } -\eta/2 \leq z \leq \delta_1 \quad (2.82)$$

If the involved experiments are comparable in spite of their very different Reynolds numbers and r/a values we may obtain an estimate of the length scale l_v by dividing the above expressions for $|v_T|$ and v_{rms}

$$l_v = \frac{|v_T|}{v_{rms}} \quad (2.83)$$

The result, shown in Figure 2.20, should not however, be taken as more than an indication of the magnitude and variation of l_v . Experiments where both τ , $\frac{\partial u}{\partial z}$ and v_{rms} are measured are clearly needed for a deeper understanding of this phenomenon.

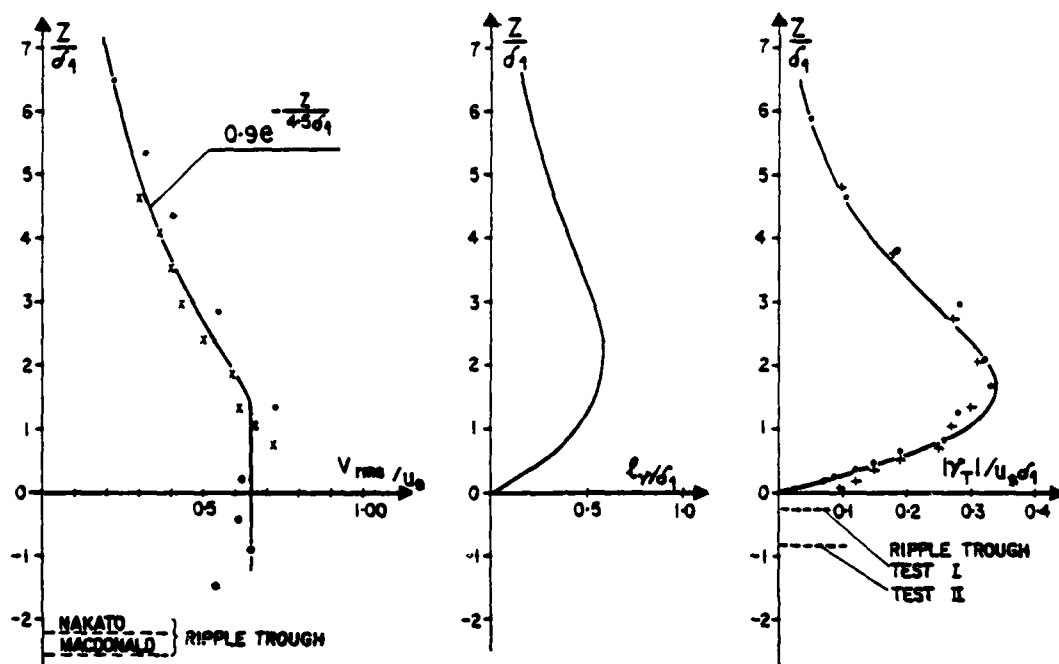


Figure 2.20: Turbulence structure of oscillatory boundary layers.

Left: Vertical velocity fluctuations measured by Macdonald (\circ), over artificial roughness, made up by half cylinders with diameter .03m; $\alpha = .282\text{m}$, $T = 6\text{s}$, $r = 0.015\text{m}$, and by Nakato et. al. (\times : over ripple crest, \circ : over trough) over natural ripples, $\alpha = .075\text{m}$, $T = 1.8\text{s}$, $d = 0.14\text{mm}$.

Center: Inferred turbulence length scale (eq. 2.83).

Right: $|v_T|$ from measurements by Jonsson and Carlsen, derived by harmonic analysis and equation (2.75). TEST I: $\alpha = 2.85\text{m}$, $T = 8.39\text{s}$, $r = 0.023\text{m}$. TEST II: $\alpha = 1.79\text{m}$, $T = 7.20\text{s}$, $r = 0.062\text{m}$.

WAVE-CURRENT BOUNDARY LAYERS.

The water motion in the surf zone normally involves oscillatory components of very different periods, from the order of one second for the harmonics and incoming waves to several hours for currents that are forced by the tides. The ability of these components to penetrate to the bottom and contribute to the motion of the large near bed sediment concentrations is highly variable. The short period oscillations develop thin boundary layers and the long period oscillations develop thick boundary layers. The thickness δ of an oscillatory boundary layer is proportional to the square root of the period:

$$\delta \sim \sqrt{T \nu_T} \quad (2.84)$$

where T is the period and ν_T is the typical eddy viscosity. This means that if the boundary layer related to a ten second swell wave is 5 centimetres thick, then the surf beat current with period 90 seconds will have a boundary layer 15 centimetres thick and a tidal current with period 12 hrs will have a boundary layer thickness of about 10 metres. So under normal surf zone conditions with depth of the order 2 metres, the wave and surf beat boundary layers are thin compared to the depth while the tidal current has a boundary layer thickness much larger than the water depth.

The Figures 2.21 and 2.22 show two examples of surf zone currents. Both were measured in the trough behind a well developed bar where the depth over the bar crest was about half a metre and

GIPPSLAND, VIC. 8 MAY, 1981
4 SHORENORMAL FLOWMETERS

1 cm/min, ± 0.5 m/s, 2V, 100 sec. Filter

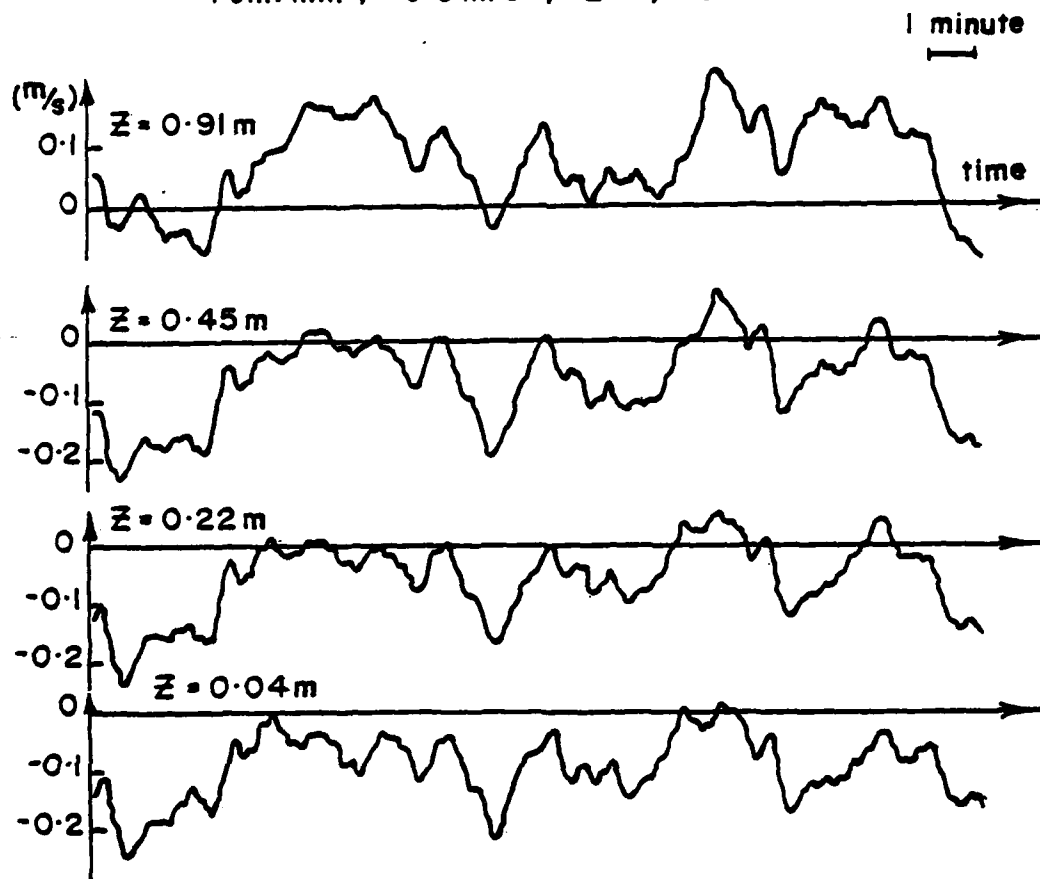


Figure 2.2 : Shore-normal current time series from 4 elevations in the bar trough showing vertical segregation: onshore velocities near the surface and offshore closer to the bed. An electronic filter with a 100 second time constant has been applied to remove incident waves. The water depth was between 1.5 and 2 metres.

**LONGSHORE VELOCITY PROFILE, MAY, 1982
EASTERN BEACH, LAKES ENTRANCE, GIPPSLAND.**

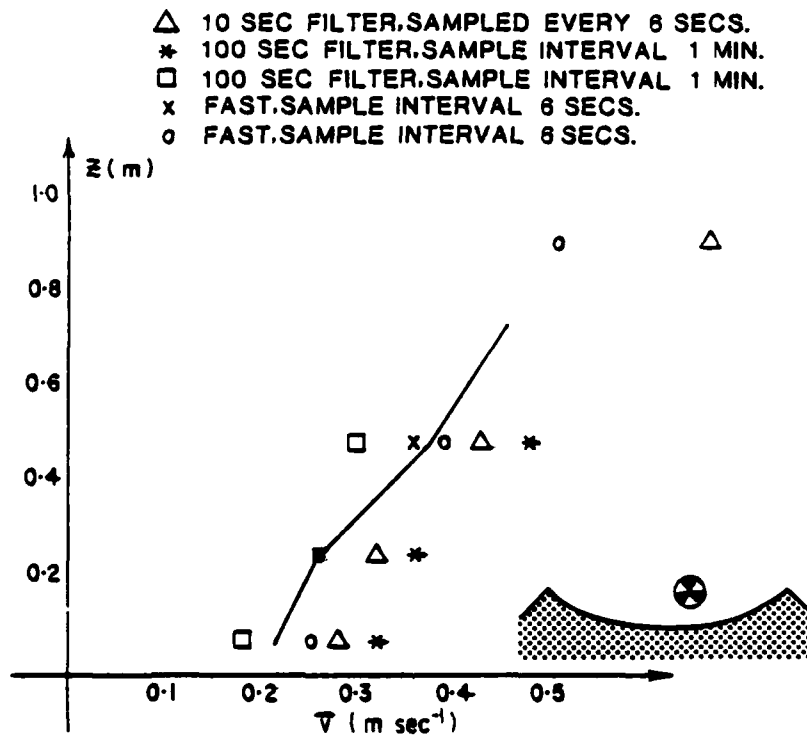


Figure 2.22: Vertical profile of time-averaged longshore current velocity, as recorded within the trough of Eastern Beach in a succession of runs. The position of the lowest flow meter relative to the ripples is shown. $h = 1.14\text{m}$, $T = 8.65\text{s}$, $H_{\text{rms}} = 0.39\text{m}$, $\eta = 0.08\text{m}$.

the maximum depth in the trough about 2 metres. For both the shore parallel current and the shore normal one, we see that the mean (obtained by averaging over about 20 minutes) varies considerably over the depth. The shore normal mean current is segregated with onshore motion at the top and offshore motion near the bed; while the longshore current shows the usual monotonous increase towards the surface. The wave and surf beat oscillations however, are unchanged right down to the lowest flow meter.

The shape of the longshore current profiles in Figure 2.22 are remarkable in that the velocity gradients between 7 and 22 centimetres are much smaller than those between 22 and 100 centimetres. This is because the waves cause a vast increase in the eddy viscosities in the lower layer. These eddy viscosities are visualized by the entrained sand in the lee vortices shed by the ripples. The particular measurements shown in figure 2.22 have been discussed in great detail by Wright et. al. (1982).

Detailed mean current profiles from under a combination of waves and currents are rare and the laboratory measurements, e.g. Brevik and Aas, (1978) and Kemp and Simons (1982) are all performed with the current parallel to the wave propagation. However, all the laboratory measurements and the field measurements of Cacchione and Drake (1982) show that the steady current profile is logarithmic above the wave boundary layer while the velocity gradients inside the boundary layer are suppressed by the extra turbulence created by the waves. The resulting appearance of the current profile is illustrated in Figure 2.23 where we have assumed a particularly simple eddy viscosity distribution, which was suggested by

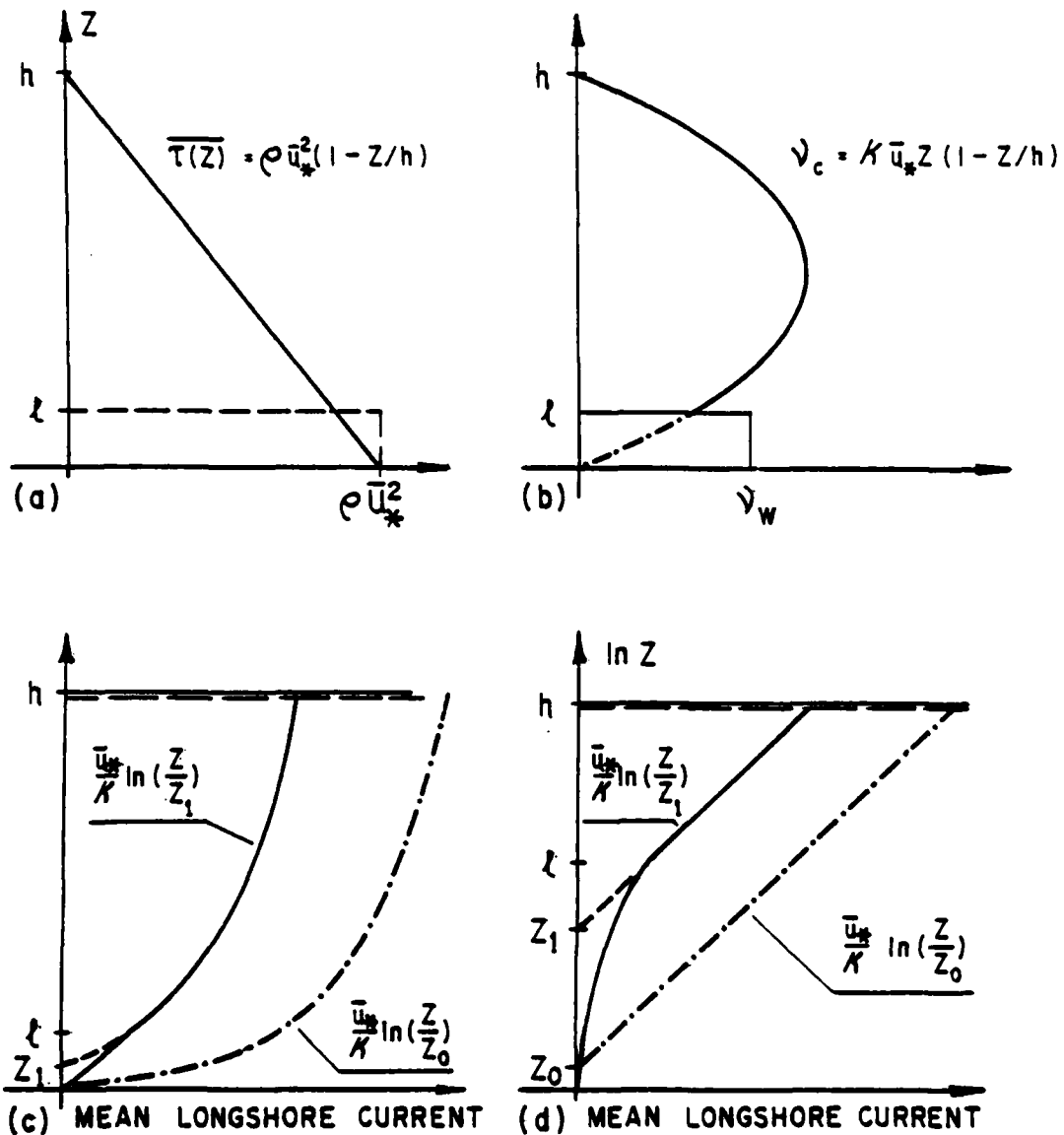


Figure 2.23: Characteristics of the mean current profile in the presence of waves, strong enough to dominate the near bed turbulence structure.

- a: The time averaged shear stress is linearly distributed and may be assumed constant for $z < \ell$ if $\ell \ll h$.
- b: The eddy viscosity distribution is parabolic for $z > \ell$ and ν_T is a constant for $z < \ell$.
- c: The $\bar{u}(z)$ distribution is logarithmic for $z > \ell$. With no waves but the same \bar{u}_* , the profile would have the same shape (same $\partial \bar{u} / \partial z$) but be shifted to the right.
- d: Same $\bar{u}(z)$ profile in the usual semi logarithmic plot where the logarithmic part becomes a straight line.

Christoffersen 1980.

$$\begin{aligned} v_T &\equiv v_w && \text{for } z \leq l \\ v_T &= \kappa \bar{u}_* z (1 - z/h) && \text{for } z \geq l \end{aligned} \quad (2.85)$$

The parabolic part, used for $z \geq l$ is the usual expression for a steady flow eddy viscosity, κ being von Karman's constant (≈ 0.4) and \bar{u}_* being the time averaged friction velocity defined by

$$\bar{u}_* = \sqrt{\bar{\tau}(0)/\rho} \quad (2.86)$$

where $\bar{\tau}(z)$ is the time averaged shear stress. The distribution of $\bar{\tau}(z)$ must be linear and we neglect wind shear stress ($\bar{\tau}(h) = 0$) so we have

$$\bar{\tau}(z) = \bar{\tau}(0) (1 - z/h) \quad (2.87)$$

or in terms of the friction velocity

$$\bar{\tau}(z) = \rho \bar{u}_*^2 (1 - z/h) \quad (2.88)$$

When the distributions of shear stresses and eddy viscosities are known, we get the velocity gradients $\partial \bar{u} / \partial z$ from the definition of

v_T :

$$\tau = \rho v_T \frac{\partial u}{\partial z} \quad (2.89)$$

With the expressions (2.85) and (2.88) this yields

$$\frac{\partial \bar{u}}{\partial z} = \frac{\bar{u}_*^2 (1 - z/h)}{v_w} \quad \text{for } z \leq l \quad (2.90)$$

$$\frac{\partial \bar{u}}{\partial z} = \frac{\bar{u}_*}{\kappa} \frac{1}{z} \quad \text{for } z \geq l \quad (2.91)$$

We can find $\bar{u}(z)$ for $z \leq l$ by integrating (2.90) and using $\bar{u}(0) = 0$:

$$\bar{u}(z) = \frac{\bar{u}_*^2}{v_w} \left(z - \frac{1}{2h} z^2 \right) \quad \text{for } z \leq l \quad (2.92)$$

The velocity above $z = l$ is found by integrating (2.91)

$$\bar{u}(z) = \frac{\bar{u}_*}{\kappa} \ln \left(\frac{z}{z_1} \right) \quad \text{for } z \geq l \quad (2.93)$$

z_1 represents the constant of integration and is equal to the level where the extrapolation of (2.93) intercepts the z axis, see Figure 2.23c and 2.23d. The value of z_1 can be determined by matching the two expressions (2.92) and (2.93) at $z = l$. We find

$$z_1 = l \exp \left[- \frac{\kappa \bar{u}_* l}{v_w} \left(1 - \frac{l}{2h} \right) \right] \quad (2.94)$$

or for $z \ll h$

$$z_1 = z \exp \left[- \frac{\kappa \bar{u}_* z}{v_w} \right] \quad (2.95)$$

Cacchoine and Drake (1982) found $z_1 \approx 4.8$ cm under field conditions and Kemp and Simons (1982) found z_1 values between 1.3 and 1.9 millimetres under 1 second waves with au increasing from 0.06 to 0.12m/s, and a depth averaged current of 0.184m/s. The bed roughness elements were triangular wooden strips of height 5 millimetres, and the z intercept z_0 , for steady current alone was 0.84 millimetres.

Experimental determination of v_T is difficult but Kemp and Simons found that the assumption of v_T being a constant in the lower layer was quite well justified under their experimental conditions where au was of the order 0.3 to 0.7 of the depth averaged mean current.

Brevik and Aas (1980) performed similar experiments, only with a stronger mean current relative to au and with sinusoidal ripples that would have been less efficient vortex makers than the triangles used by Kemp and Simons. Their velocity profiles were logarithmic in the inner layer which indicates a linearly increasing v_T as assumed by Grant and Madsen (1979).

The limited experimental evidence seems thus to indicate that the ripple eddy viscosity model (2.85) applies when the boundary layer is dominated by the waves, while a different model like the one of Grant and Madsen (1979) must be applied when the current dominates. Visual observation of bed forms can easily reveal which one is dominant

at a given location. If the bed is flat or covered by symmetrical ripples, it is most likely that the waves are dominating; but if the bed is covered by asymmetrical dunes like in rip currents, the current must be dominating.

3. THE MOTION OF SUSPENDED PARTICLES

Since the main topic of the present report is suspended sediment we shall study the small scale motion of such particles in some detail.

We do that in terms of an analytical solution for the equation of motion of a suspended particle in an accelerated non uniform flow field. This solution treats the effects of gravity and those of the fluid accelerations separately, which is a major advantage because it enables a step wise analytical treatment of the problem which is easier to follow physically than numerical models that take all steps at once.

Wave boundary layers are dominated by vortices and therefore we pay special attention to this kind of flow structure. However the resulting formulae are quite general and apply to any flow as long as the fluid accelerations are reasonably small compared to the acceleration of gravity.

SEDIMENT MOTION IN VORTEX FLOW, QUALITATIVELY

For kinematic as well as for dynamic analysis of suspended sediment motion, it is convenient to split the sediment particle velocity \vec{u}_p into three parts, as shown in Figure 3.1

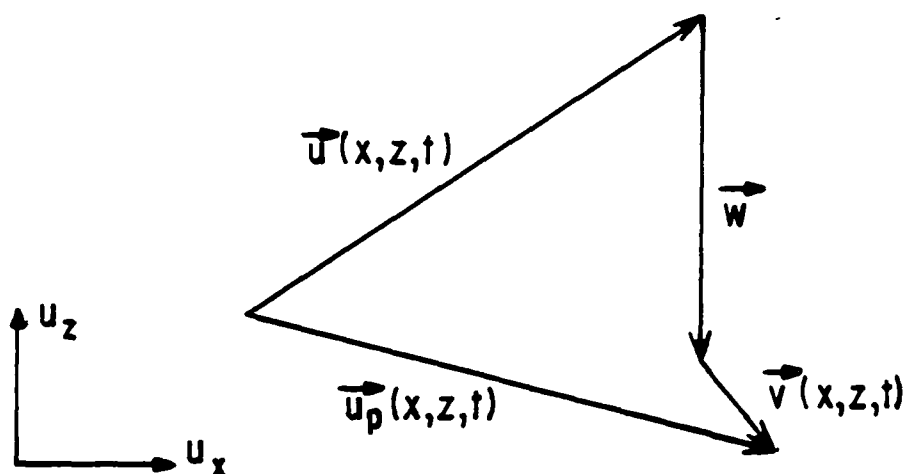


Figure 3.1: The sediment velocity u_p is split into three parts: $\vec{u}_p = \vec{u} + \vec{w} + \vec{v}$, and \vec{v} is treated as a perturbation to $\vec{u} + \vec{w}$.

$$\vec{u}_p(x, z, t) = \vec{u}(x, z, t) + \vec{w} + \vec{v}(x, z, t) \quad (3.1)$$

where \vec{u} is the water velocity, \vec{w} is the still water settling velocity and \vec{v} is due to the accelerations of the flow (see Figure 3.1). In most practical situations the fluid accelerations are much smaller than the acceleration of gravity, g , so we have

$$|\vec{v}|/w \approx \left| \frac{d\vec{u}}{dt} \right|/g \ll 1 \quad (3.2)$$

and can use

$$\vec{u}_p \approx \vec{u} + \vec{w} \quad (3.3)$$

as an approximation for the sediment particle velocity. Let us see what that leads to in vortex flow.

Consider a forced vortex with the velocity field

$$u_z^x = \Omega \frac{-z}{x} \quad (3.4)$$

which is that of a rigid body rotating with angular velocity Ω .

Applying equation (3.3) we find

$$\vec{u}_p \approx \vec{u} + \vec{w} = \Omega \left(\frac{-z}{x} - w/\Omega \right) \quad (3.5)$$

($\vec{w} = (0, -w)$). This shows that a sediment particle will move along some circle with centre $(w/\Omega, 0)$ (See Figure 3.2). Tooby et. al. (1977) showed experimentally that small particles do in fact follow these circular paths very closely and only very slowly spiral away from them. We shall study this spiralling process in detail later.

The interesting implication of these approximately closed paths is that the Lagrangian mean velocity for the sediment particles is approximately $\vec{0}$ and not \vec{w} as one would find from $\vec{u}_p = \vec{u} + \vec{w}$, assuming that \vec{u} is random turbulence with average $\vec{0}$. This emphasizes the importance of considering the flow structure in the context of sediment entrainment.

The fact that the settling velocity is partly eliminated in a vortex flow field has been touched upon by Reizes (1977) who found it in a numerical study. He concluded that the sediment particle must spend more time in the upward moving parts of the flow than in the downward moving parts. This is indeed the case; the sediment path sketched in Figure 3.2 lies completed in the "upward

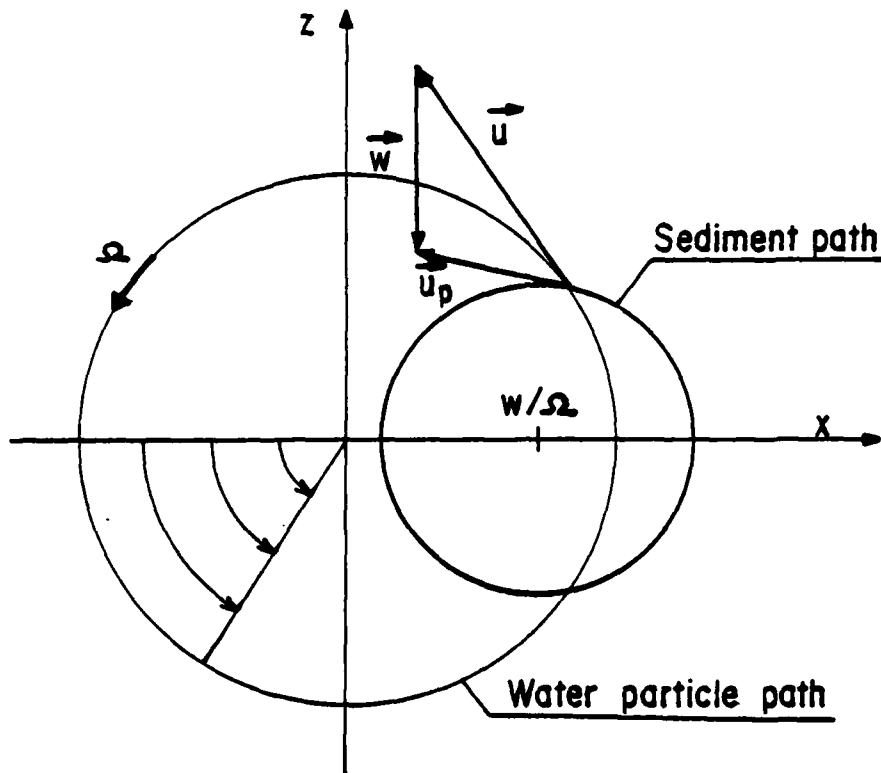


Figure 3.2: Sediment particle with settling velocity w moving in a forced vortex with velocity field \vec{u} . The particle paths corresponding to $\vec{u} + \vec{w}$ are circles and thus the lagrangian mean of the sediment particle velocity will be zero.

moving" part of the vortex. For buoyant particles or air bubbles the center of the "sediment path" would lie on the negative x-axis and thus they would spend the majority of the time within downward moving fluid.

The described trapping mechanism will work for all sand grains with settling velocity smaller than the maximum velocity in the vortex.

The next questions to be asked is whether the trapping is a feature of the rather unnatural, forced vortex only. The answer is no for the following reason : In general, the velocity field of a two dimensional vortex can be written

$$\vec{u} \begin{pmatrix} x \\ z \end{pmatrix} = \Omega F(x^2 + z^2) \begin{pmatrix} -z \\ x \end{pmatrix} \quad (3.6)$$

and the first approximation to the sediment velocity is then

$$\vec{u}_p = \vec{u} + \vec{w} = \Omega F(x^2 + z^2) \begin{pmatrix} -z \\ x \end{pmatrix} + \begin{pmatrix} 0 \\ -w \end{pmatrix} \quad (3.7)$$

For the components u_{px} and u_{pz} of this we have

$$u_{px}(x, -z) = -u_{pz}(x, z) \quad (3.8)$$

and

$$u_{pz}(x, -z) = u_{pz}(x, z) \quad (3.9)$$

This symmetry means that any particle path that crosses the x-axis twice must be closed since, due to the symmetry, a particle which has travelled along the curve P_1P_2 must travel back to P_1 via the image of P_1P_2 (see Figure 3.3). Hence closed sediment paths are a general feature of vortex flow.

A fair model of many natural vortices is the Rankine vortex in which the velocity field is given by

$$\vec{u} \begin{pmatrix} x \\ y \end{pmatrix} = \frac{\Omega R}{1 + (x/R)^2 + (z/R)^2} \begin{pmatrix} -z/R \\ x/R \end{pmatrix} \quad (3.10)$$

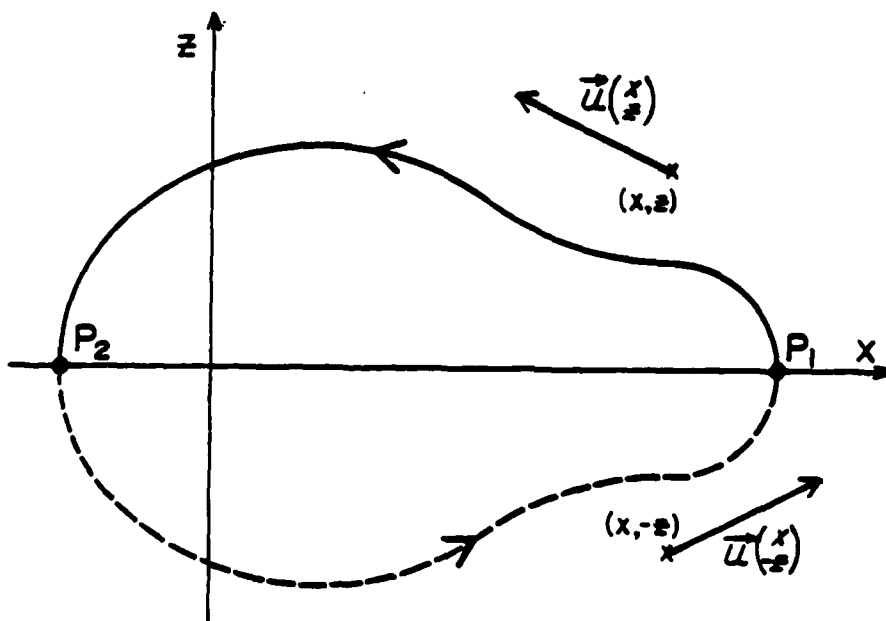


Figure 3.3: In a vortex, where the flow field has the form given by equation (3.6), any particle path given by $\vec{u}_p = \vec{u} + \vec{w}$ must be closed, if it crosses the x-axis twice.

In this vortex a sand grain with settling velocity w can be at rest at the two singular points in Figure 3.5:

$(R\Omega/2w \pm \sqrt{(R\Omega/2w)^2 - 1}, 0)$, where $\vec{u} + \vec{w} = \vec{0}$. The circle shown, which is given by

$$\left(\frac{x}{R} - \frac{\Omega R}{2w}\right)^2 + \left(\frac{z}{R}\right)^2 = \left(\frac{\Omega R}{2w}\right)^2 - 1 \quad (3.11)$$

contains all points with $u_{pz} = 0$. Sand grains will move upward ($u_{pz} > 0$) in the interior and downward ($u_{pz} < 0$) outside the circle.

Figure 3.5 also shows the sediment particle paths corresponding to $\vec{u}_p = \vec{u} + \vec{w}$. Some of these are closed and could thus keep sand grains trapped. Trapping is only possible if the settling velocity is less than the maximum upward water velocity. That is if $w < \Omega R/2$.

The equation of the sediment path through $(x_0, 0)$ is

$$z^2 = -R^2 - x^2 + (R^2 + x_0^2) \exp \left[\frac{2w}{\Omega R} \frac{x}{R} - \frac{x_0}{R} \right] \quad (3.12)$$

Now, it could be argued that since the paths are closed, sediment particles are no more likely to get onto them than to get off. And hence the trapping mechanism is not going to be effective. However, the situation in practice is that the sediment gets into the vortex during its formation. This process is easy to observe with the vortices behind ripples and dunes.

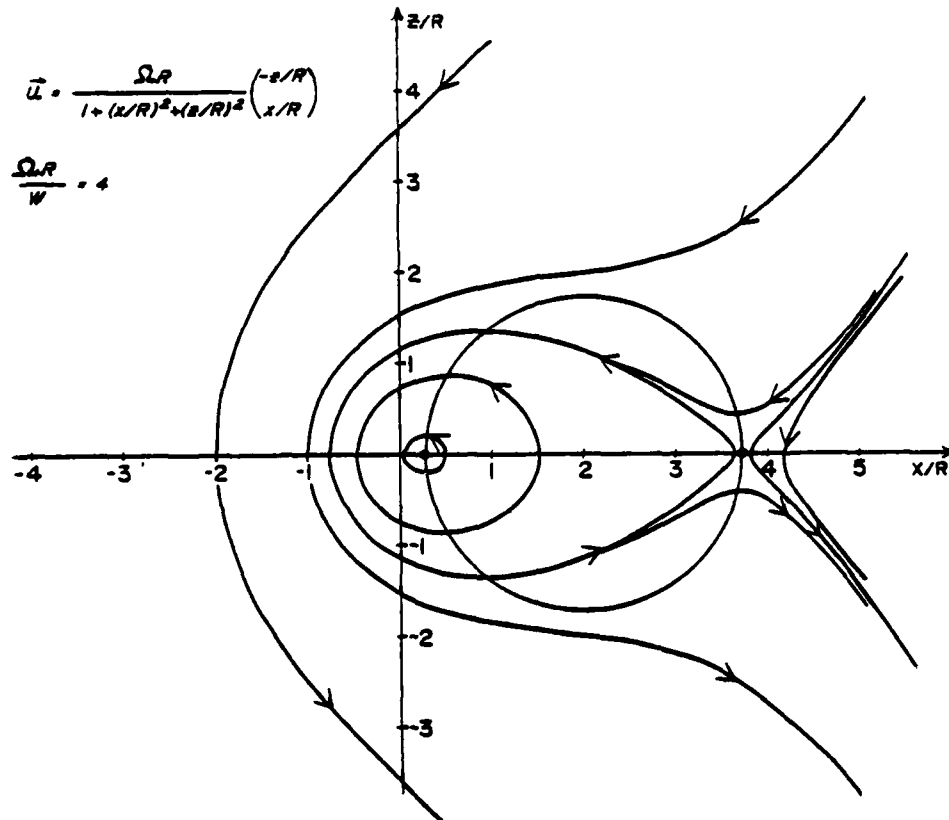


Figure 3.5: Particle paths corresponding to $\vec{u}_p = \vec{u} + \vec{w}$ in a Rankine vortex. In the inner region where $|\vec{u}|$ is proportional to the distance from the origin, we get curves that are very similar to the circles in the forced vortex (Figure 3.2).

QUANTITATIVE APPROACH

Consider a particle with diameter d and relative density s , moving in a liquid with velocity $\vec{u}(x, z, t)$ under the action of gravity. The equation of motion is:

$$\frac{d\vec{u}_p}{dt} = \frac{1}{s} \frac{d\vec{u}}{dt} + \frac{C_M}{s} \frac{d}{dt}(\vec{u} - \vec{u}_p) - \frac{3C_D}{4ds} |\vec{u}_p - \vec{u}| (\vec{u}_p - \vec{u}) + \frac{1}{s}(s-1) \vec{g} \quad (3.13)$$

The first term on the right-hand side represents the pressure gradients in the flow. The second expresses the influence of the hydrodynamic mass which is C_M/s times the mass of the particle. The third term is due to the drag force on the particle, and C_D' is the instantaneous drag coefficient which is a function of the instantaneous Reynolds number.

$$R = \frac{|\vec{u} - \vec{u}_p| d}{\nu} \quad (3.14)$$

The validity of using this instantaneous drag coefficient C_D' was verified by Ho (1964), who used it for numerical calculations. In the following we use the approximation

$$C_D' = \frac{|\vec{u} - \vec{u}_p|^{-\gamma}}{w} \quad C_D = \frac{|\vec{w} + \vec{v}|^{-\gamma}}{w} \quad C_D \quad (3.15)$$

where C_D is the drag coefficient corresponding to the terminal settling velocity through still water. The exponent γ is thus defined by

$$\gamma = - \left. \frac{d \ln C_D}{d R} \right|_{R = wd/\nu} \quad (3.16)$$

In the laminar case, where Stoke's law is valid we get $\gamma = 1$ and in the turbulent areas where C_D is practically independent of R we get $\gamma = 0$. See Figure 3.6.

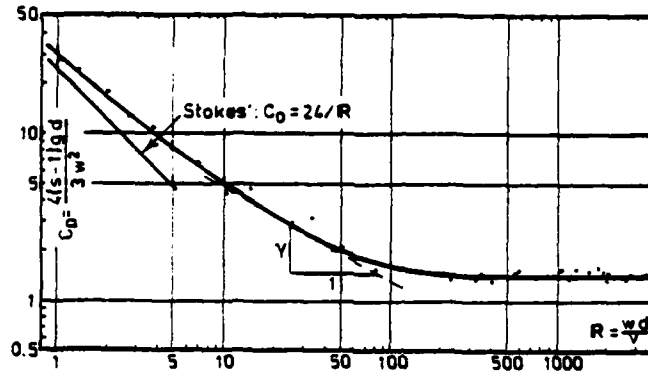


Figure 3.6: The variation of the drag coefficient C_D with the grain-Reynold's number : wd/v . After Navntoft (1968)

The Basset term, which yields a drag effect when $|\vec{u} - \vec{u}_p|$ changes magnitude rapidly, has been neglected because

$$|\vec{u}_p - \vec{u}| = |\vec{w} + \vec{v}| \quad (3.17)$$

is essentially constant ($\approx w$) under the assumption

$$\frac{d\vec{u}}{dt} / g \ll 1 \quad (3.18)$$

which holds for most practical cases. From the definition of C_D

$$(s-1)\rho g \frac{\pi}{6} d^3 = \frac{1}{2} \rho C_D w^2 \frac{\pi}{4} d^2 \quad (3.19)$$

we get

$$\frac{3C_D}{4d(s-1)} = \frac{g}{w^2} \quad (3.20)$$

Now we introduce

$$\vec{u}_p(x, z, t) = \vec{u}(x, z, t) + \vec{w} + \vec{v}(x, z, t) \quad (3.21)$$

into the equation of motion with

$$\frac{d\vec{u}}{dt} = \frac{\partial \vec{u}}{\partial t} + \vec{u} \cdot \nabla \vec{u} \quad (3.21)$$

and

$$\frac{d\vec{v}}{dt} + \frac{\partial \vec{v}}{\partial t} + (\vec{u} + \vec{w} + \vec{v}) \cdot \nabla \vec{v} \quad (3.22)$$

then we get

$$\frac{d\vec{v}}{dt} + \vec{w} \cdot \nabla \vec{u} + \vec{v} \cdot \nabla \vec{u} = \quad (3.23)$$

$$\left(\frac{1}{s} - 1\right) \frac{d\vec{u}}{dt} + \frac{C_M}{s} \frac{d}{dt} (-\vec{w} - \vec{v}) - \frac{3}{4sd} C_D \left(\frac{|\vec{w} + \vec{v}|}{w} \right)^{-\gamma} |\vec{w} + \vec{v}| (\vec{w} + \vec{v}) + \frac{s-1}{s} g$$

The drag term is simplified by equation (3.20), and we introduce

$$\alpha = \frac{s-1}{s+C_M} \quad (3.24)$$

So we get the following simplified equation of motion

$$\begin{aligned}
\frac{d\vec{v}}{dt} + \frac{1}{1+C_M/s} \vec{w} \cdot \nabla \vec{u} + \frac{1}{1+C_M/s} \vec{v} \cdot \nabla \vec{u} = \\
-\alpha \frac{d\vec{u}}{dt} + \frac{g}{w^{2-\gamma}} |\vec{w} + \vec{v}|^{1-\gamma} (\vec{w} + \vec{v}) - \vec{g}
\end{aligned} \quad (3.25)$$

To assess the relative magnitude of the terms we bring the equation on dimensionless form by the following transformations

$$\vec{U} = \vec{u}/w \quad (3.26)$$

$$\vec{V} = \vec{v}/w \quad (3.27)$$

$$\vec{W} = \vec{w}/w \quad (3.28)$$

$$T = \Omega t \quad (3.29)$$

$$X = X/R \quad (3.30)$$

$$Z = X/R \quad (3.31)$$

where Ω is a typical angular velocity of the flow and R a characteristic length. This leads to:

$$\begin{aligned}
\frac{d\vec{V}}{dT} + \frac{w/\Omega R}{1+C_M/s} \vec{W} \cdot \nabla \vec{U} + \frac{w/\Omega R}{1+C_M/s} \vec{V} \cdot \nabla \vec{U} = \\
-\alpha \frac{d\vec{U}}{dT} + \frac{g}{w\Omega} |\vec{W} + \vec{V}|^{1-\gamma} (\vec{W} + \vec{V}) - \frac{\vec{g}}{w\Omega}
\end{aligned} \quad (3.32)$$

and in terms of the vector components with the drag term expanded

$$\begin{aligned}
\frac{dv_x}{dt} - \frac{w/\Omega R}{1+C_M/s} \frac{\partial U_x}{\partial Z} + \frac{w/\Omega R}{1+C_M/s} \left[v_x \frac{\partial U_x}{\partial X} + v_z \frac{\partial U_x}{\partial Z} \right] = \\
-\alpha \frac{dU_x}{dT} + \frac{g}{w\Omega} \left[v_x - (1-\gamma) v_x v_z + \dots \right]
\end{aligned} \quad (3.33)$$

$$\frac{dv_z}{dt} - \frac{w/\Omega R}{1+C_M/s} \frac{\partial u_z}{\partial z} + \frac{w/\Omega R}{1+C_M/s} \left[v_x \frac{\partial u_z}{\partial x} + v_z \frac{\partial u_z}{\partial z} \right] =$$

$$-\alpha \frac{du_z}{dt} + \frac{g}{w\Omega} \left[(2-\gamma) v_z + \frac{2-3\gamma+\gamma^2}{1} v_z^2 - \frac{1-\gamma}{2} v_x^2 \dots \right] \quad (3.34)$$

We omit terms of the order of magnitude $|\vec{V}|^2$ and rearrange

$$\frac{dv_x}{dt} + \frac{\alpha g}{w\Omega} v_x + \frac{w/\Omega R}{1+C_M/s} \left[\frac{\partial u_x}{\partial x} v_x + \frac{\partial u_x}{\partial z} v_z \right] =$$

$$-\alpha \frac{du_x}{dt} + \frac{w/\Omega R}{1+C_M/s} \frac{\partial u_x}{\partial z} \quad (3.35)$$

$$\frac{dv_z}{dt} + (2-\gamma) \frac{\alpha g}{w\Omega} v_z + \frac{w/\Omega R}{1+C_M/s} \left[\frac{\partial u_z}{\partial x} v_x + \frac{\partial u_z}{\partial z} v_z \right] =$$

$$-\alpha \frac{du_z}{dt} + \frac{w/R}{1+C_M/s} \frac{\partial u_z}{\partial z} \quad (3.36)$$

In most practical cases w will be a few centimetres per second or less and R will be a centimeter or more, so the second term of the left hand side will dominate completely over the third, which may thus be neglected. The resulting equations on dimensional form are

$$\frac{dv_x}{dt} + \frac{\alpha g}{w} v_x = -\alpha \frac{du_x}{dt} + \frac{w}{1+C_M/s} \frac{\partial u_x}{\partial z} \quad (3.37)$$

$$\frac{dv_z}{dt} + (2-\gamma) \frac{\alpha g}{w} v_z = -\alpha \frac{du_z}{dt} + \frac{w}{1+C_M/s} \frac{\partial u_z}{\partial z} \quad (3.38)$$

When the velocity field is steady and uniform, the driving terms disappear and the solutions are

$$v_x(t) = v_x(t_0) \exp \left[-\frac{\alpha g}{w} (t-t_0) \right] \quad (3.39)$$

$$v_z(t) = v_z(t_0) \exp \left[-(2-\gamma) \frac{\alpha g}{w} (t-t_0) \right] \quad (3.40)$$

which shows that deviations from

$$\vec{u}_p = \vec{u} + \vec{w} \quad (3.3)$$

decay with a time scale of $\frac{w}{\alpha g}$ which is for most natural sediments less than 10^{-2} seconds.

This corresponds well with the results of Jenkin's (1973) who found numerically that a sand particle released in still water will only travel a distance comparable to its own diameter, before it has obtained its terminal settling velocity.

Note that for a sand grain moving in air the situation is very different because the time scale $\frac{w}{\alpha g}$ is at least one order of magnitude bigger in that case and so are the typical velocities.

In an accelerated flow field, deviations from (3.3) will be very small compared to \vec{w} because of the large damping factor $\frac{\alpha g}{w}$ (see equation 3.37 and 3.38). So equation (3.3) can be expected to give a good first approximation to the sand motion in a flow field with moderate accelerations, $(|\frac{d\vec{u}}{dt}| < g)$.

SIMPLE EXAMPLE

To gain a basic understanding of the acceleration effects, let us look at the very simple example of a small grain ($\gamma=1$) moving in a forced vortex. The velocity field is given by

$$\vec{u}(\vec{x}) = \Omega \begin{pmatrix} -z \\ x \end{pmatrix} \quad (3.4)$$

and

$$\vec{u} + \vec{w} = \Omega \begin{pmatrix} -z \\ x - w/\Omega \end{pmatrix} \quad (3.5)$$

Equation (3.5) corresponds to motion along any circle which centre $(w/\Omega, 0)$ and angular velocity Ω . See Figure 3.2.

For our small grain with $\gamma=1$ equations (3.37 and 3.38) yield:

$$\frac{d\vec{v}}{dt} + \frac{\alpha g}{w} \vec{v} = -\alpha \frac{d}{dt} \begin{pmatrix} -\Omega z \\ \Omega x \end{pmatrix} + \frac{w}{1+C_M/s} \frac{\partial}{\partial z} \begin{pmatrix} -\Omega z \\ \Omega x \end{pmatrix} \quad (3.41)$$

We introduce

$$\begin{pmatrix} x \\ z \end{pmatrix} = \begin{pmatrix} R \cos \Omega t + w/\Omega \\ R \sin \Omega t \end{pmatrix} \quad (3.42)$$

which corresponds to the same steady circular motion as (3.5), and find

$$\frac{d\vec{v}}{dt} + \frac{\alpha g}{w} \vec{v} = \alpha \Omega^2 R \begin{pmatrix} \cos \Omega t \\ \sin \Omega t \end{pmatrix} + \begin{pmatrix} -w\Omega/(1+C_M/s) \\ 0 \end{pmatrix} \quad (3.43)$$

The first term on the right hand side is a centrifugal acceleration which results in a rotating velocity \vec{v}_R :

$$\vec{v}_R = \frac{\Omega^2 R}{g} w \frac{1}{\sqrt{1 + \left(\frac{w\Omega}{\alpha g}\right)^2}} \begin{pmatrix} \cos \left(\Omega t - \tan^{-1} \frac{w\Omega}{\alpha g}\right) \\ \sin \left(\Omega t - \tan^{-1} \frac{w\Omega}{\alpha g}\right) \end{pmatrix} \quad (3.44)$$

In most practical cases, we will have $w\Omega/\alpha g \ll 1$ and thus we see that \vec{v}_R is nearly proportion to $\Omega^2 R/g = |\frac{d\vec{u}}{dt}|/g$ and that \vec{v}_R is parallel to \vec{R} except for the small angle $\tan^{-1} \frac{w\Omega}{\alpha g}$ (see Figure 3.7).

The second term on the right-hand side of (3.43) is the Coriolis acceleration which gives a steady drift \vec{v}_s towards the left for $s < 1$ and to the right for $s > 1$ (see Figure 3.7).

$$\vec{v}_s = \begin{pmatrix} \frac{-w^2 \Omega}{(s-1)g} \\ 0 \end{pmatrix} \quad (3.45)$$

The effect of \vec{v} is to make the grain spiral out (for $w > 0$) slowly. To estimate the time scale for this process we put

$$\vec{v}_R \approx \frac{R\Omega^2}{g} w \begin{pmatrix} \cos \Omega t \\ \sin \Omega t \end{pmatrix} \quad (3.46)$$

which assumes

$$\frac{\alpha}{\alpha + \beta} < 1 \quad (3.47)$$
$$\vec{v} = \vec{v}_R + \vec{v}_S = \frac{\Omega^2}{g} \vec{wR} - \frac{1}{s-1} \begin{pmatrix} w^2 \Omega / g \\ 0 \end{pmatrix} \quad (3.48)$$

The last, steady term is not contributing to the spiralling process in average over a revolution so the spiralling can be modelled by

$$\frac{dR}{dt} = \frac{\Omega^2}{g} wR \quad (3.49)$$

($\vec{u} + \vec{w}$ is perpendicular to \vec{R}) which has the solution

$$R(t) = R_0 \exp \left[\frac{\Omega^2 w}{g} (t - t_0) \right] \quad (3.50)$$

showing that the time scale of the spiralling process is

$$t_s = \frac{g}{w\Omega^2} \quad (3.51)$$

This time scale will normally be several seconds in which time the particle is travelling with the vortex with effective settling velocity zero.

The solution given by (3.44) and (3.45) is valid for particles that are so small that Stokes law applies, that is $\gamma = 1$. The general solution is:

$$v_x = \frac{\Omega^2 R w}{g \sqrt{1 + \beta^2}} \cos(\Omega t - \tan^{-1} \beta) - \frac{w^2 \Omega}{(s-1)g} \quad (3.52)$$

$$v_z = \frac{\Omega^2 R w}{g \sqrt{(2-\gamma)^2 + \beta^2}} \sin(\Omega t - \tan^{-1} [\beta / (2-\gamma)]) \quad (3.53)$$

where $\beta = w\Omega / \alpha g \ll 1$.

SECOND ORDER EFFECTS

Due to the non linearity (for $\gamma > 0$) of the drag term in equation (3.13), a sediment particle will settle slower through an accelerated or non uniform flow field than through still water. This effect can be analyzed by considering second order terms ($O(V^2)$) in solutions of equations (3.33) and (3.34). Nielsen (1979) studied this phenomenon for a homogenous, vertically oscillating flow, ($u_z = R\Omega \cos \Omega t$), and found that the reduction in settling velocity is of the order of magnitude $[R\Omega^2/g]^2 w$ which is in most practical cases very small compared to w . This analytical solution was shown to be in good agreement with measurements and numerical calculations, carried out by Ho (1964).

4. FIELD DATA

THE SEDIMENT SAMPLER

Over the twenty month period from October 1980 to July 1982, the Coastal Studies Unit has collected 71 detailed profiles of time averaged suspended sediment concentrations $\bar{c}(z)$, complete with hydrodynamic data and bed sediment samples.

The sediment sampler which was designed by Peter Nielsen and constructed by Graham Lloyd is probably the most simple instrument one can think of for this kind of task. It has no electrical or mechanical, moving parts and is therefore very rugged and dependable. The sand-water-mixture is collected by suction and the driving pressure difference is provided by connecting the sample jars, that sit on the sea bed, to a common air outlet above the water.

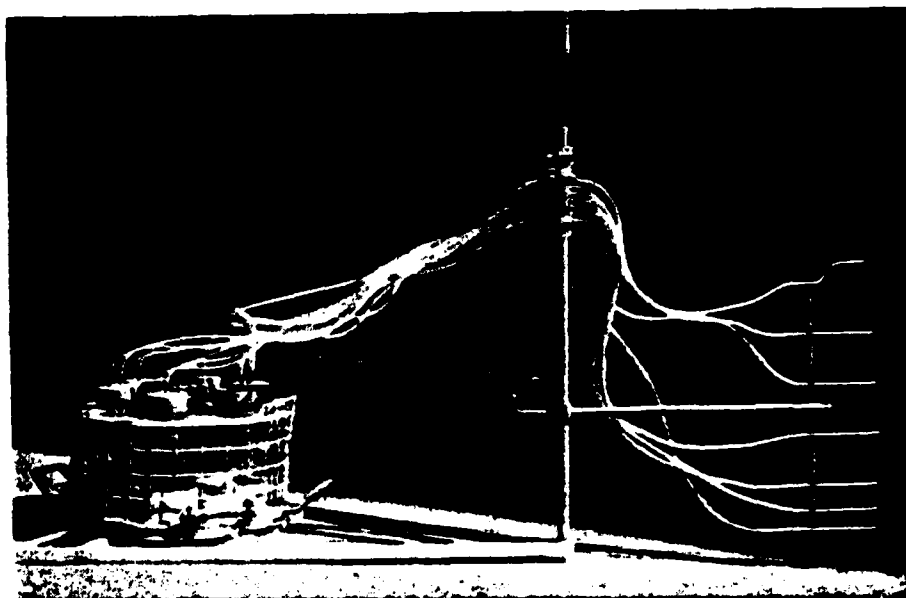


Figure 4.1: The sediment sampler.

The sampler is designed to sample a vertical array of simultaneous time averaged sediment concentrations, $\bar{c}(z)$.

The maximum distance between the top and bottom intakes is .55m, and the seven intakes can be placed with different intervals. The interval between the two bottom intakes, where the concentration gradients are largest is normally 4 centimetres and the intervals between the higher intakes vary from 10 to 15 centimetres. The interval between the bed and the bottom intake is adjusted once the sampler has been placed in the sampling position.

The intake nozzels are stainless steel pipes, 15 centimetres long and with inner and outer diameters of 3 and 6 millimetres respectively. The intakes are connected to the sample jars by transparent plastic hose with 5 millimetre inner diameter.

Glass jars of 2.2 litre capacity are used as sample jars. This size is sufficient for obtaining measurable amounts of sand ($\geq .05$ grammes) at concentrations as small as 10^{-5} by volume. This capacity is normally only required outside the surfzone. For measurements in areas with breaking waves and/or strong net currents it is recommended to use smaller jars, which will be easier to handle.

Because the jars must be placed on the bed and remain stable, while still full of air, a considerable mooring weight is needed. The seven 2.2 litre jars are kept in place by a steel plate, weighing approximately 32 kilogrammes.

Each sample jar has a water/sediment intake and an air outlet. The air outlets are connected to a common outlet which ends at the top of the glass fibre mast. The mast also helps to locate the sampler. Note that it is not necessary for the main outlet to be out

of the water. However, to provide sufficient sampling speed it should be at least one metre above the top of the jars, and the main outlet must be kept from filling with water before the sampling begins.

The distance from the intakes to the nearest part of the sample jars is 1.25m, and the intakes are .65m from the nearest part of the sampler that touches the bed. This assures a minimum of disturbance of the bed and the flow near the intakes, when the sampler is oriented properly relative to the flow. That is, the bottles are placed downstream from the intakes if a net current is present and the horizontal symmetry axis of the sampler is aligned along the wave crests.

The most common working depth until now has been 1.5m, so the driving pressure difference, which is that between the jar stoppers and the end of the air outlet, is 0.13 atmospheres. Under such conditions the jars fill up in about 3.5 minutes, which corresponds to an intake velocity of 1.5m/s. This is so much larger than the typical settling velocity ($\sim .04$ m/s) of suspended sand that one can expect all grains to be caught. On the other hand, the flow velocities induced by the suction are only about .03 m/s at positions one centimetre away from the centre of the intake, so the suction itself causes very little disturbance to the main flow field, where the typical velocity magnitude is 0.5m/s.

TRANSDUCER AND FLOW METER CHARACTERISTICS.

The hydraulic data referred to in this paper are obtained from analysis of strip charts on which water velocities and wave heights were recorded during the sediment sampling process. The response time of the chart recorder for the relevant output values is about

0.2 seconds and thus negligible compared to the time scale of natural waves, and the scaling parameter of the chart recorder is incorporated in the calibration of the instruments.

Like the chart recorder, the pressure transducers respond immediately and it is therefore assumed that the gain is the same for oscillatory input with the frequency of natural waves as it is for static pressures. After a days sampling work, the transducer-chart-recorder system is calibrated hydrostatically before disconnection in order to achieve maximum accuracy ($\pm .01m$) on determination of mean water level and wave heights. The calibration arrangements is shown in Figure 4.2.

The flow meters have been calibrated by moving them through still water attached to a heavy pendulum with periods between 2.5 and 5.5 seconds. This calibration shows that the instrument responses are linear for velocity amplitudes between 0.1 and 2 m/s and that the frequency response can be described by

$$F(\omega) = \frac{1}{1 + .77i\omega} \quad (4.1)$$

This means that the following relation exists between measured velocities u_m and real velocities u :

$$.77 \frac{du_m}{dt} + u_m = u \quad (4.2)$$

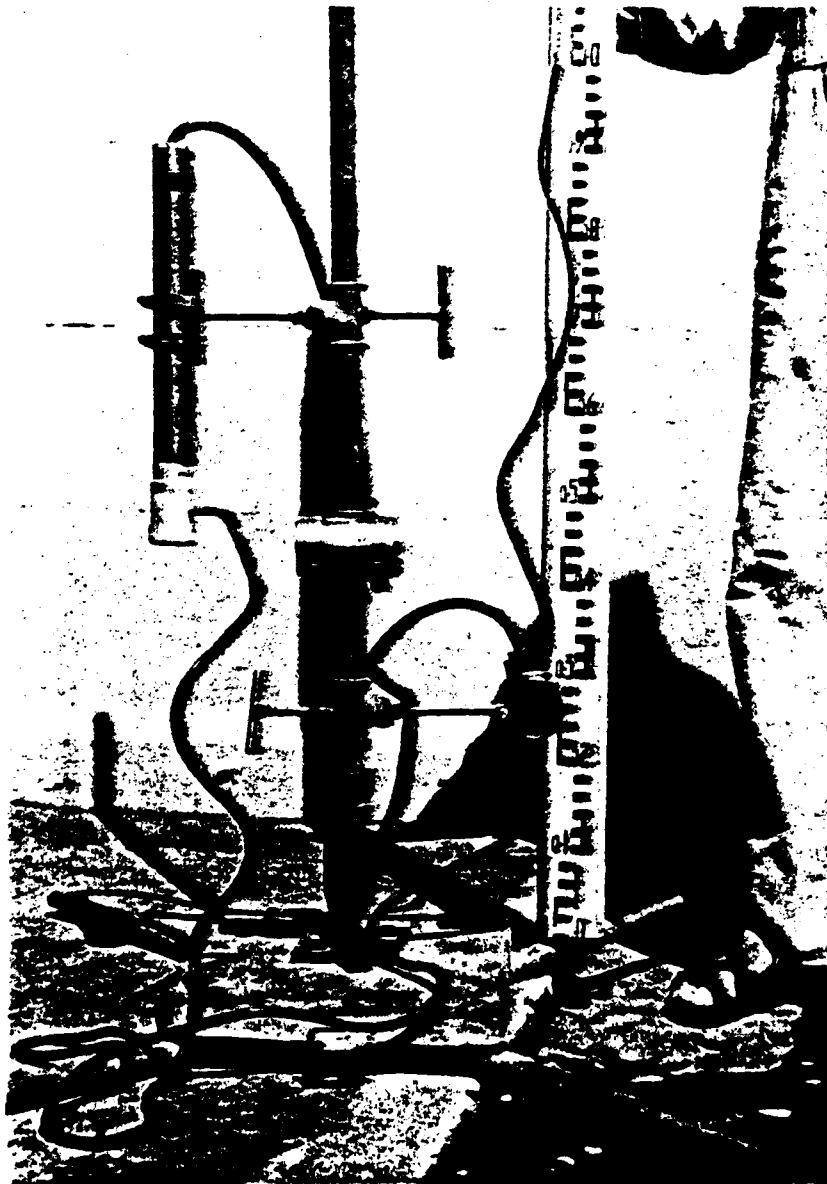


Figure 4.2: Instrument pod with flowmeters and pressure transducer. The transducer is shown with the calibration device. Different hydrostatic pressure is given by the position of the water surface in the hose.

The equations (4.1) and (4.2) provide two means of correcting the velocity measurements. Equation (4.1) can be used for correcting spectra, and (4.2) can be used for direct correction of time series.

In the following analysis, the flow meter data are only used to determine wave period and time average velocities \bar{U} and \bar{V} in the shore normal and longshore directions respectively, while the oscillatory velocity amplitude aw is obtained from the pressure records via linear wave theory.

EXPERIMENTAL PROCEDURE, DETERMINATION OF $\bar{c}(z)$.

The sampling sites are chosen so that the hydraulic conditions and the bed topography are as stationary and well defined as possible. When such a location has been found the pod with flow meters and the pressure transducer is installed. The standard setup has two ducted impellor flow meters and one pressure transducer. The shore normal flow meter is placed .2m above the bed and the longshore one at .3m. The pressure transducer is normally placed at about .5m above the bed.

The sampler is placed near the instrument pod so that the velocity measurements should represent the flow at the sampling spot and at the same time far enough away (and up stream) such that the sampler and the pod do not disturb each other.

Then the position of the intakes is carefully adjusted, and the elevation of the lowest intake above the bed is measured. If the bed is rippled, the intakes are always placed over a ripple crest.

When everything is ready, a clamp which has been blocking the intake and outlet hoses is removed, the sampling starts. When the jars are full, the intake elevation is measured again and a sand

sample is taken from the bed near the intakes. If the bed is rippled, height and length of these are measured. After this the sampler is brought ashore where the total volume of the samples is noted and the sand is filtered out. The sand is dried and weighed later in the laboratory so that the concentration can be worked out from:

$$\bar{c} = \frac{\text{mass of sand}}{(\text{density of sand}) \times (\text{total volume})} \quad (4.3)$$

DETERMINATION OF THE SEDIMENT PARAMETERS: \bar{d} , \bar{w} and V

The bottom sample from each run is sieved and the average diameter is found from

$$\bar{d} = \frac{\sum m_i d_i}{\sum m_i} \quad (4.4)$$

where m_i and d_i are mass and average diameter of each sieving fraction.

The average settling velocity is similarly found from

$$\bar{w} = \frac{\sum m_i w_i}{\sum m_i} \quad (4.5)$$

The variation coefficient V of the settling velocity is defined by

$$V = \frac{\text{Var}\{w\}}{\bar{w}^2} \quad (4.6)$$

and the variance is found from

$$\text{Var}\{w\} = \frac{N}{N-1}(\overline{w^2} - \bar{w}^2) \quad (4.7)$$

where N is the number of sieves. The settling velocity w_i for the different sieve fractions is determined by settling tube experiments for each experiment location. This is necessary because the relation between grain size (d) and settling velocity (w) varies a great deal between beaches, see Figure 4.3. This variability is caused by differences in abundance and geometry of shell fragments in the bed material. These shell fragments can have quite large sieving diameters while their settling velocity is much smaller than that of the equivalent quartz sphere.

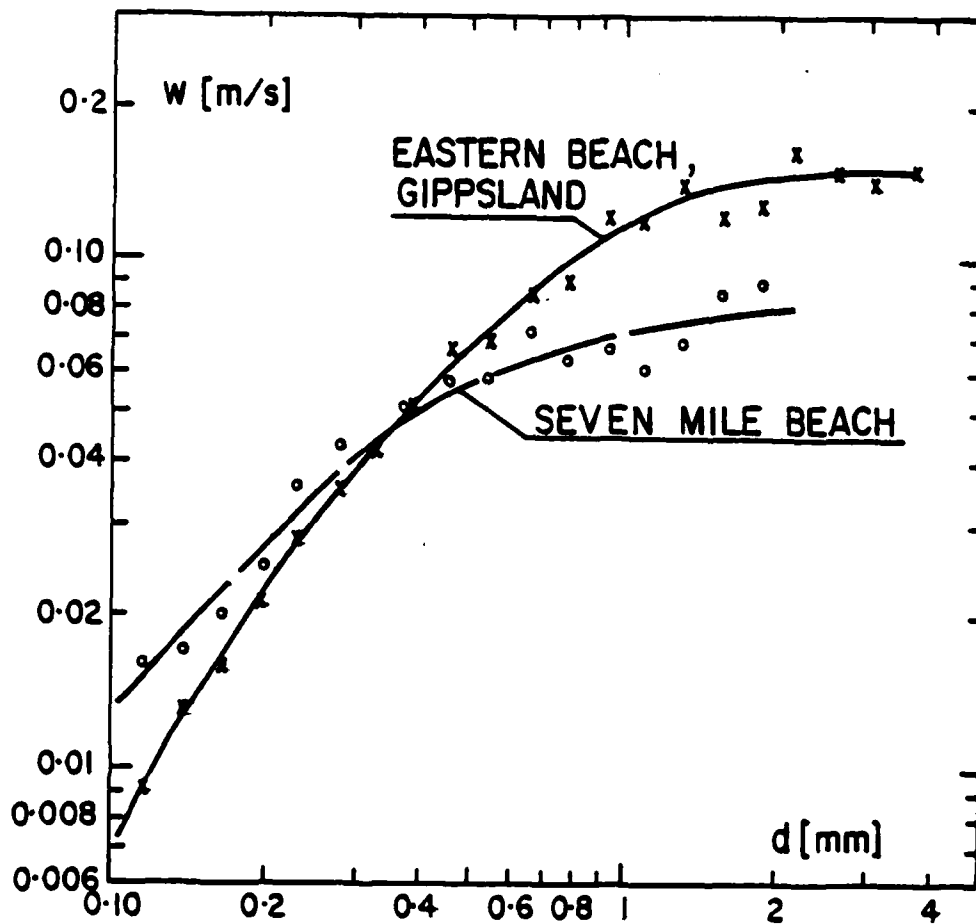


Figure 4.3: The relation between sieving grain size and settling velocity for two of the test locations. This relation varies considerably from beach to beach due to variations in grain geometry and mineral composition.

DETERMINATION OF h , T , H_s , \bar{U} and \bar{V} .

Considering the scatter of the concentration measurements, it was concluded that a representation of the hydraulic conditions by the water depth h , the significant wave height H_s , the average period T and the average flow velocities \bar{U} and \bar{V} would be detailed enough. The wave period is defined by the time interval between successive zero down crossings of the shore normal velocity $u(t)$. This definition is chosen because the reversal of the near bed velocity is essential for the behaviour of the wave boundary layer.

The significant wave height H_s is defined as the average of the highest third of the zero down crossing wave heights. That is, the height from the bottom of the wave trough to the top of the following crest. The water depth, h , and average flow velocities \bar{U} and \bar{V} are normally found by running the pressure transducer and flow meters in 100 second filter mode for about 5 minutes before and after the sampling. From the basic parameters mentioned above and using linear wave theory we derive the semi excursion α :

$$\alpha = \frac{H_s}{2 \sinh \frac{2\pi}{L} h} \quad (4.8)$$

and the velocity amplitude $\alpha\omega$ using $\omega = 2\pi/T$. The mobility number ψ is given by

$$\psi = \frac{(\alpha\omega)^2}{(s-1)gd} \quad (4.9)$$

where s is the relative density of the sand and g is the acceleration due to gravity.

DETERMINATION OF C_0 , l_s , ϵ_s and ϵ_{sc} .

Concentration profiles for suspended sediment fall into two categories. Exponential profiles are obtained from measurements over large sharp crested ripples under non-breaking waves. These profiles are characterized by the two parameters C_0 and l_s , which can be found by an exponential curve fit:

$$\bar{c}(z) = C_0 \exp(-z/l_s) \quad (4.10)$$

where C_0 determines the concentration magnitudes while the vertical length scale

$$l_s = \left[\frac{d \ln \bar{c}}{dz} \right]^{-1} \quad (4.11)$$

determines the rate of exponential decrease away from the bed. The length scale l_s is equivalent to ϵ / \bar{w} where ϵ is the so called diffusivity. These exponential profiles are similar to those measured in the laboratory by Horikawa and Watanabe (1967), Nakato et. al. (1977), MacDonald (1977) and Nielsen (1979).

The above mentioned exponential profiles are restricted to experimental locations where the waves are non breaking and the bed is covered by well developed vortex ripples with long shore parallel crests and heights in the interval

$$0.05 \alpha \leq \eta \leq 0.25 \alpha \quad (4.12)$$

When the bed forms are different or the waves are breaking, we find different concentration profiles indicating a different entrainment mechanism. These profiles are concave upward in the usual plots of $\ln \bar{c}$ versus z . As pointed out by Nielsen (1979) such profiles are well represented by the expression

$$\ln \bar{c} = \ln c_o - \frac{\bar{w}h}{\sqrt{\epsilon_B \epsilon_S}} \tan^{-1} \sqrt{\frac{\epsilon_S}{\epsilon_B}} \frac{z}{h} \quad (4.13)$$

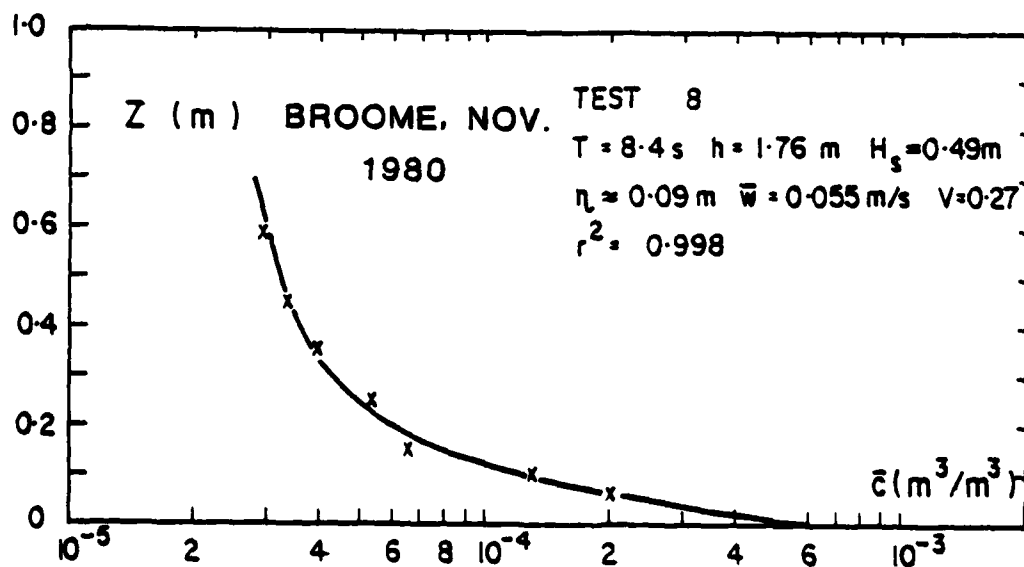


Figure 4.4: Equation 4.13 fitted to measured \bar{c} -values.

which corresponds to a diffusion model with the diffusivity distribution

$$\epsilon_a(z) = \epsilon_B + \epsilon_s \left(\frac{z}{h}\right)^2 \quad (4.14)$$

via the one dimensional, time averaged diffusion equation

$$\epsilon_a \frac{d\bar{c}}{dz} + \bar{w}\bar{c} = 0 \quad (4.15)$$

ϵ_a is an apparent diffusivity because equation (4.14) assumes that all suspended sand has the settling velocity \bar{w} .

The best fit values of the three parameters in equation (4.13) rewritten as

$$\ln \hat{c} = \alpha_1 - \alpha_2 \tan^{-1} \alpha_3 \frac{z}{h} \quad (4.16)$$

are found by the least squares criterion

$$\frac{\partial}{\partial \alpha_i} \sum [\ln \bar{c} - \ln \hat{c}]^2 = 0, \quad i = 1, 2, 3 \quad (4.17)$$

by a generalized Newton iteration and the goodness of fit, r^2 , is defined by

$$r^2 = \frac{\text{Cov} \{ \ln \hat{c}, \ln \bar{c} \}}{(\text{Var} \{ \ln \hat{c} \} \text{Var} \{ \ln \bar{c} \})^{0.5}} \quad (4.18)$$

If the bed material contains fractions with different settling velocities and if all grain sizes obey the diffusion equation

$$\epsilon \frac{d\bar{c}}{dz} + w\bar{c} = 0 \quad (4.19)$$

where ϵ is independent of grain size, the concentration of different size fractions will decrease at different rates away from the bed and the shape of the compound concentration profile will thus depend on the distribution of settling velocities for the bed material. This means that the apparent diffusivity ϵ_a , and ϵ_s in particular, which comes out of the curve fitting process, depends on the w -distribution. We shall now show how this effect can be eliminated from the observations.

In the following we assume that the time averaged concentrations $\bar{c}(z,w)$ of sand with settling velocity w obey the one dimensional diffusion equation on the form (4.19) which expresses that the upward flux $-\epsilon \frac{d\bar{c}}{dz}$ equals the downward flux $w\bar{c}$ at any level. The general solution to (4.19) is

$$\bar{c}(z,w) = C_0(w) \exp \left\{ -\int_0^z \frac{w}{\epsilon} dz_1 \right\} \quad (4.20)$$

where $C_0(w)$ is the concentration of sand with settling velocity w at $z = 0$. For completely homogeneous sand with $w \equiv \bar{w}$ the concentration profile would be given by

$$\bar{c}(z) = C_0 \exp \left\{ -\int_0^z \frac{\bar{w}}{\epsilon} dz_1 \right\}, \quad w \equiv \bar{w} \quad (4.21)$$

For convenience we introduce

$$\sigma = \int_0^z \frac{\bar{w}}{E} dz_1 \quad (4.22)$$

so that (4.21) can be rewritten

$$\bar{c}(z) = C_0 e^{-\sigma} \quad \text{for } w \equiv \bar{w} \quad (4.23)$$

Natural sediments are not homogeneous and the variance of settling velocity has a significant effect on the concentration profiles, making the gradients larger near the bed and smaller towards the surface.

If we introduce the non dimensional settling velocity

$$w' = w/\bar{w} \quad (4.24)$$

and the density function $f(w')$ defined by

$$f(w')dw' = C_0(w)/C_0, \quad 0 < w' < \infty \quad (4.25)$$

we get the following distribution for the fraction with settling velocity w

$$\bar{c}(z, w) = C_0 e^{-w'\sigma} f(w')dw' \quad (4.26)$$

and for the total concentration

$$\bar{c}(z) = C_0 \int_0^\infty e^{-w'\sigma} f(w')dw' \quad (4.27)$$

It was shown by Nielsen (1979) that the type of density function is not critical as long as $f(w')$ has the right variance $V = \text{Var}(w)/\bar{w}^2$ and a mean value of 1. We choose a Γ -distribution because it fits natural w' -distributions reasonably well (see Figure 4.5) and also gives simple analytical results

$$f(w') = \frac{(1/V)^{1/V}}{\Gamma(1/V)} \exp(-w'/V) w'^{1/V-1} \quad (4.28)$$

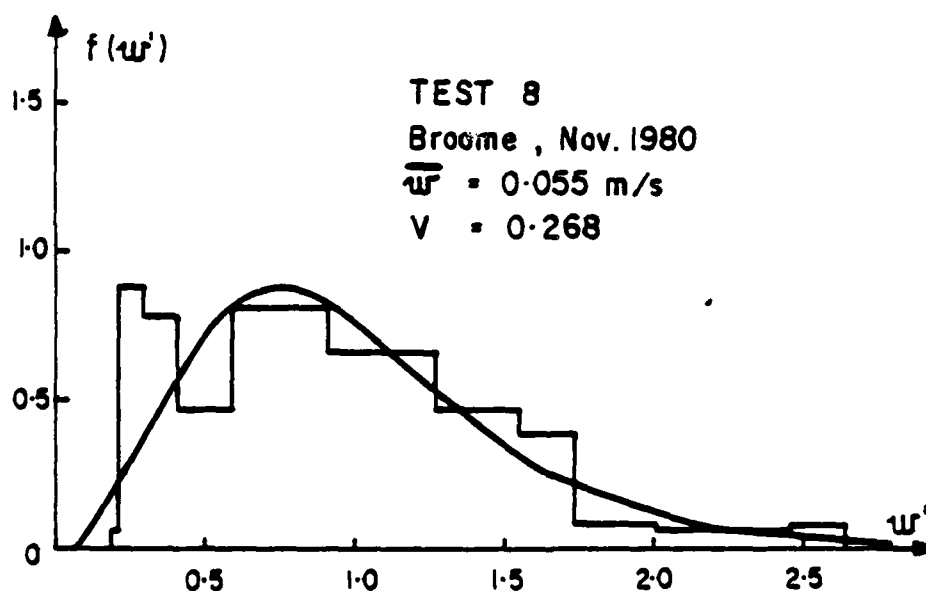


Figure 4.5: Natural distribution approximated by Γ -distribution.

Inserting this into equation (4.27) we find the simple result:

$$\bar{c}(z) = c_0 \left(\frac{1}{1+\sigma V} \right)^{1/V} \quad (4.29)$$

under the assumption that ϵ and thus σ is independent of w' .

AD-A121 122

SUSPENDED SEDIMENT UNDER WAVES(U) SYDNEY UNIV
(AUSTRALIA) COASTAL STUDIES UNIT P NIELSEN ET AL.
SEP 82 CSU-TR-82/6 N00014-80-G-0001

244

UNCLASSIFIED

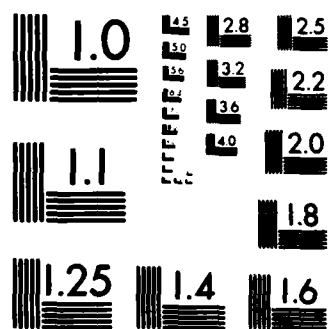
F/G 8/3

NL

END

FILED

DIME



MICROCOPY RESOLUTION TEST CHART
NATIONAL BUREAU OF STANDARDS-1963 A

The desired aim is to find a method for determining a true ϵ from a measured \bar{c} -profile of non homogeneous sediment. This can be done in the following way. Equation (4.22) yields the following relation between σ and the true diffusivity

$$\frac{\bar{w}}{\epsilon} = \frac{d\sigma}{dz} \quad (4.30)$$

and can get $\frac{d\sigma}{dz}$ from (4.29):

$$\frac{d\sigma}{dz} = -\left(\frac{c_0}{\bar{c}}\right)^V \frac{d \ln \bar{c}}{dz} \quad (4.31)$$

and find

$$\epsilon = \left(\frac{\bar{c}}{c_0}\right)^V \frac{-\bar{w}}{\frac{d \ln \bar{c}}{dz}} \quad (4.32)$$

Let us compare this true diffusivity with the apparent one, ϵ_a , which we would find by neglecting the variance of w . The apparent diffusivity ϵ_a is found by applying (4.21) directly to the concentrations of non homogeneous sediment which yields

$$\epsilon_a = \frac{-\bar{w}}{\frac{d \ln \bar{c}}{dz}} \quad (4.33)$$

and thus

$$\frac{\epsilon}{\epsilon_a} = \left(\frac{\bar{c}}{c_0}\right)^V \quad (4.34)$$

The result shows that the ratio between real and apparent

diffusivities at a given level depends only on the measurable quantity \bar{c}/C_0 and on the variation coefficient V , which is very convenient. We see that the effect depends strongly on V as one would expect and that the effect is negligible near the bed (where $\bar{c} \approx C_0$).

The corrected surface diffusivity ϵ_{sc} is derived from (4.14) and (4.34)

$$\epsilon_{sc} = \epsilon_a(h) \left(\frac{\bar{c}(h)}{C_0} \right)^V - \epsilon_B \quad (4.35)$$

$$\epsilon_{sc} = (\epsilon_B + \epsilon_s) \exp \left[- \frac{\bar{w}hV}{\sqrt{\epsilon_B \epsilon_s}} \tan^{-1} \sqrt{\frac{\epsilon_s}{\epsilon_B}} \right] - \epsilon_B \quad (4.36)$$

DESCRIPTION OF EXPERIMENT SITES

PALM BEACH

Experiments 1 and 2 were carried out at the southern end of Palm Beach, on October 26, 1980. Palm Beach is the most northern of Sydney's beaches, and on the day of the experiments it was in an accreting state with shallow bars moving onshore. The bed was covered with large ripples or megaripples.

CABLE BEACH, BROOME

Experiments 3 through 24 were performed on Cable Beach at Broome, North Western Australia in November 1980. Cable Beach has a tidal range of more than 9 metres, and most of the beach profile is flat, without bars. Ripples are generally small or absent because the sediment is very fine. Exceptions from this general pattern are some areas near the neap high tide line where the sediment is coarse ($\bar{d} \approx 0.5$ mm) due to a large content of shell fragments. These areas tend to develop ridge and runnel systems, and at high tide the bed is covered by sharp crested vortex ripples. Experiments 9, 10 and 11 were performed over such ripples. The morphology and wave climate are described in more detail in Wright et al (1982).

MEROO BEACH

Experiments 25 through 35 were carried out at the southern end of Meroo Beach approximately 8 kilometres south of Ulladulla, New South Wales in February 1981. The beach was in an intermediate state with rather confused bar topography. The bed forms were large vortex ripples or megaripples.

SEVEN MILE BEACH

Experiments 36 through 43 were carried out at the northern end of Seven Mile Beach, south of Kiama, New South Wales in March 1981 and experiments 61 through 66 were done at the same location in March 1982. The northern end of Seven Mile Beach has very fine sand throughout and is exposed to the prevailing sea and swell from the Southeast. The modal state of the beach is therefore the extreme dissipative. The profile is flat, bed-forms are normally absent, and the sand is very firmly packed (no foot prints).

EASTERN BEACH

Experiments 48 through 60 were carried out on Eastern Beach at Lakes Entrance, Victoria in May 1981. At the time of the experiments a well developed bar about a hundred metres from the shoreline was moving towards the shore. The depths over the bar crest was less than half a metre at low tide while the maximum depth in the trough was about two metres. All suspension measurements were taken in the trough at depths of approximately one metre. The bed was always covered by well developed vortex ripples that showed no influence at all from the sometimes strong longshore current which reversed with the tide.

WARRIWOOD BEACH

Experiments 67, 68 and 69 were carried out in April 1982 at Warriwood Beach, which is one of Sydney's northern beaches. The modal state of the beach is intermediate because the sand is quite coarse and the headlands at both ends give some protection. The suspension measurements were taken on the outer slope of a shallow bar and the bed was covered by megaripples.

WINDAWOPPA BEACH

Experiments 70 and 71 were carried out on Windawoppa Beach at Hawk's Nest, fifty kilometres northeast of Newcastle, New South Wales in July 1982. The beach was recovering after being severely eroded by storm waves the preceding week. The topography was rather confused and the bed was covered with megaripples at the test site.

PEARL BEACH

Experiments 44 through 47 were carried out at Pearl Beach, north of Broken Bay near Sydney in March 1981. The measurements were taken over the rippled bed about 10 metres seaward from the step of the reflective beach. Since wave reflection is very significant for this location, the hydrodynamic data for these experiments were derived from the near bed water velocities rather than from the pressure variation.

5. EMPIRICAL RESULTS

SEDIMENT DISTRIBUTIONS OVER VORTEX RIPPLES

Twenty eight of the experiments were performed over well developed vortex ripples (R), under non breaking waves.

The results show the same general picture as the laboratory experiments of Horikawa and Watanabe (1967), Bijker et. al. (1976), Nakato et. al. (1977), MacDonald (1977) and Nielsen (1979). That is, the profiles are straight lines in the usual semi logarithmic plot, ($\log \bar{c}$ versus z), showing that \bar{c} decays exponentially away from the bed.

$$c(z) = C_0 \exp(-z/L_s) \quad (4.10)$$

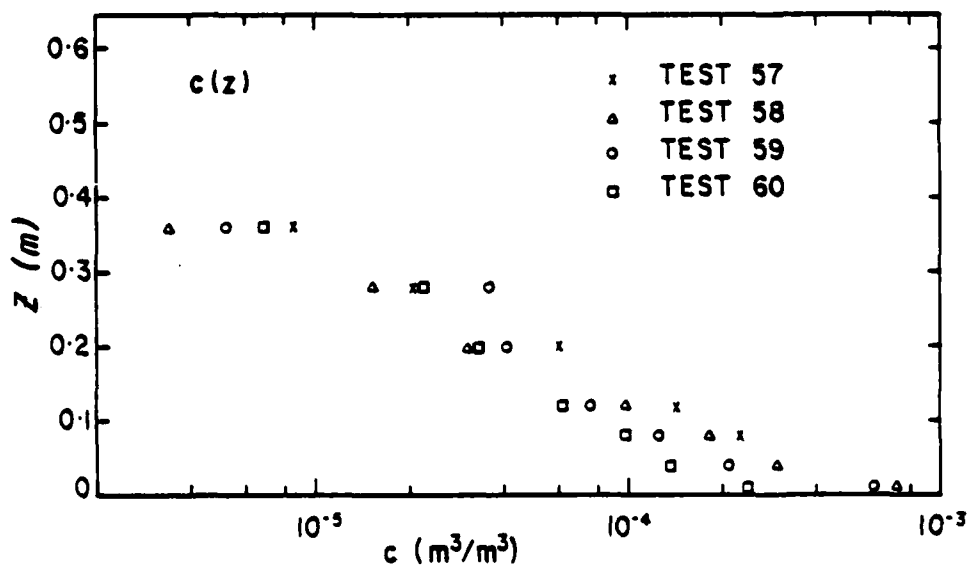


Figure 5.1: Four successive profiles measured over well developed ($\eta/a \approx .12$) vortex ripples in a bar trough. The profiles are exponential with a vertical length scale approximately equal to the ripple height η ($\approx .08m$).

The vertical length scale of this decay (l_s) is approximately equal to the ripple height η , so the concentrations decay by a factor 100 ($\approx e^{4.5}$) over four to five ripple heights. Figure 5.1 shows the results of four successive runs from the bar trough in Gippsland. Apart from the abovementioned exponential behaviour the figure also shows the repeatability of the tests.

We can thus describe these concentration profiles by two parameters C_0 and l_s . C_0 determines the magnitude and l_s determines the distribution. It was pointed out by Nielsen (1979) and it may be seen in the data of Nakato et. al. in Figure 5.2 that concentration profiles measured over the ripple trough are slightly different from those over the crest. Both will be approximately exponential but C_0 will be 1.5 times smaller over the trough than over the crest while l_s will be the same factor larger, so that the total amount of suspended material

$$\int_0^{\infty} C dz = C_0 l_s \quad (5.1)$$

is the same for all vertical sections. All the field measurements of the present study and the laboratory experiments quoted in the following were taken over the ripple crest.

In general we would expect l_s to be a function of the bed geometry, the boundary layer structure and the parameters that determine the sand motion in the boundary layer flow.

When the bed is covered with sharp crested ripples, the natural vertical length scale is the ripple height η .

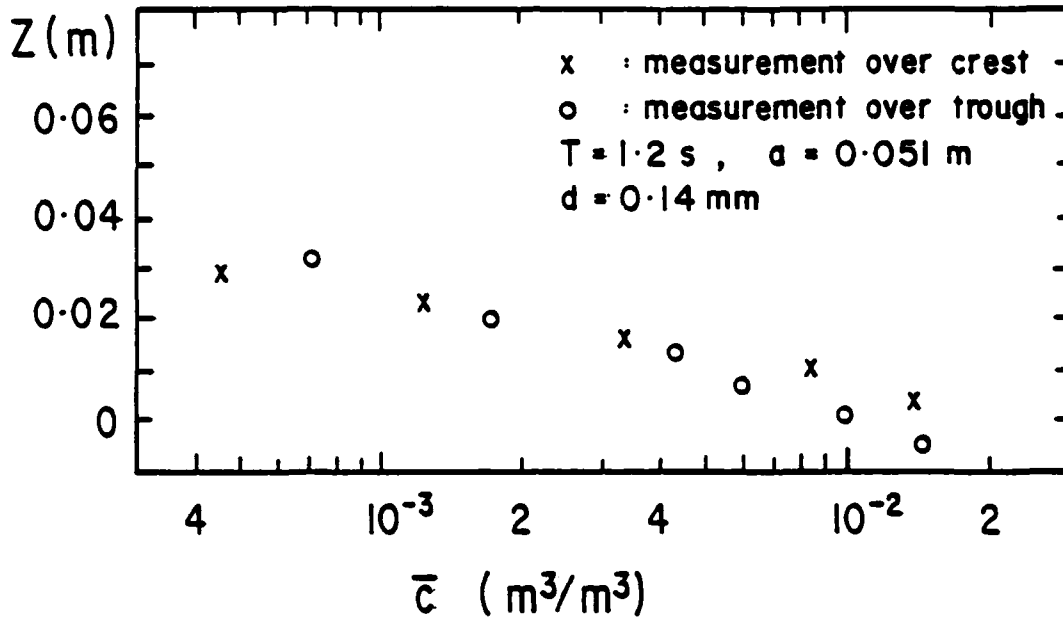


Figure 5.2: Tunnel data from Nakato et. al. (1977). The time-mean concentration decreases faster over the ripple crest than over the trough.

The boundary layer structure will depend on η/a and on the flow Reynolds number $a^2\omega/\nu$.

The flow structure is dominated by the lee vortices and we found in Chapter 3 that the behaviour of a sand grain in vortex flow is determined by the grain Reynolds number wd/ν and the velocity ratio $R\Omega/w$. The observations of Tunsdall and Inman (1975) show that the velocity scale in the lee vortices is $a\omega$ so we may replace $R\Omega$ by $a\omega$.

In the present context it might also be relevant to consider the ratio t_s/T between the spiralling time scale (equation 3.51) and the wave period.

We would thus expect l_s to be given by a relation of the form

$$\frac{l_s}{\eta} = F \left(\frac{\eta}{a}, \frac{a^2\omega}{\nu}, \frac{wd}{\nu}, \frac{t_s}{T}, \frac{a\omega}{w} \right) \quad (5.2)$$

The following empirical considerations show that most of the variation of l_s/η can be accounted for by aw/w in the case of fully developed sharp crested ripples.

Figure 5.3 shows l_s/η as function of t_s/T and we see that for all the data where aw/w is reasonably big ($aw/w > 9$) the variation is not significant except for a few data points with $t_s/T > 1$. The points that fall far below correspond to small values of aw/w (< 7.5) which indicates that for aw/w less than about 9 the vortex trapping mechanism is less efficient. To calculate t_s we have used equation (3.51) and assumed that the velocity scale in the vortex is aw and that the vortex radius is 0.5η . We thus find the angular velocity Ω in the vortex to be

$$\Omega = \frac{a}{0.5\eta} \frac{2\pi}{T} \quad (5.3)$$

and

$$\frac{t_s}{T} = \frac{gT\eta^2}{16\pi^2 w a^2} \quad (5.4)$$

Experiments with extremely large values of t_s/T will also lead to unusually high values of l_s/η . Large values of t_s/T occur when T and w are both small and η/a is large. In relative terms, such conditions are characterized by small grain Reynolds numbers ($wd/\nu \leq 1$) and small flow Reynolds numbers ($a^2w/\nu \leq 2000$), e.g. the experiments "H" and "N" in Figures 5.3 through 5.5.

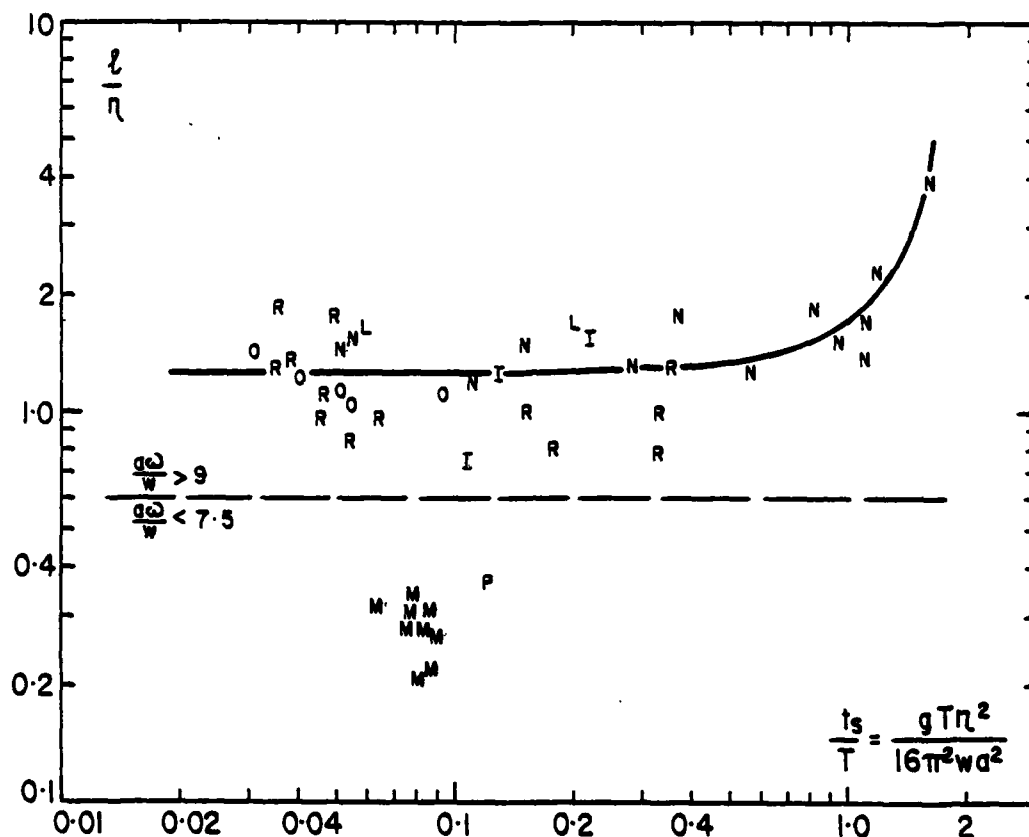


Figure 5.3: The variation of z_s/η with t_s/T is insignificant for $t_s/T < 1$, which includes all field observations. But the variation with gw/w must be strong since all data with $gw/w < 7.5$ fall significantly below the rest. Since the typical value of z_s/η is $1.4 \approx 1/\ln 2$, we can derive the following rule of thumb:

The concentration decreases by a factor two when the elevation is increased by one ripple height.

The symbols used in Figure 5.3 and the following are defined in Table

5.1. The field data are primarily described by the bed topography:

R for vortex ripples, T for small ripples with low steepness due to

high shear stresses, F for flat beds and MR for megaripples. But

they may alternatively be described by the wave characteristics: N

for non breaking, S for spilling breakers or P for plunging breakers.

Symbol	Author	Wave Period (Seconds)	Grain Size (mm)	Facility	η/a
.	MacDonald (1977)	3.2 - 15.2	.45	Swing	.031 - .075
I	Nakato et. al. (1977)	1.2, 1.8, 2.4	.14	Tunnel	.16 - .18
J	Homma et. al. (1965)	1.0, 1.3, 1.6, 1.72	.18	Flume	.11 - .33
H	Nielsen (1979)	1.0	.082	Flume	.18 - .47
L	Nielsen (1979)	1.7	.17	Flume	.11 - .20
M	Nielsen (1979)	1.7	.55	Flume	.18 - .23
N	Nielsen (1979)	1.7, 1.27	.082	Flume	.050 - .28
O	Nielsen (1979)	1.3, 1.7, 3.0	.19	Flume	.076 - .15
P	Nielsen (1979)	1.7	.36	Flume	.24
R	Present study	6.1 - 11.5	.28 - .50	Field	.010 - .23
T	Present study	5.3 - 11.2	.19 - .48	Field	.018 - .010
F	Present study	5.3 - 12.9	.12 - .23	Field	0.00
MR	Present study	5.3 - 11.2	.28 - .50	Field	0.08 - 0.13

Table 5.1: Key to the symbols in figures 5.3 through 5.15. The field data from the present study may alternatively be distinguished by breaker conditions: "N" for non breaking, "S" for spilling breakers and "P" for plunging breakers.

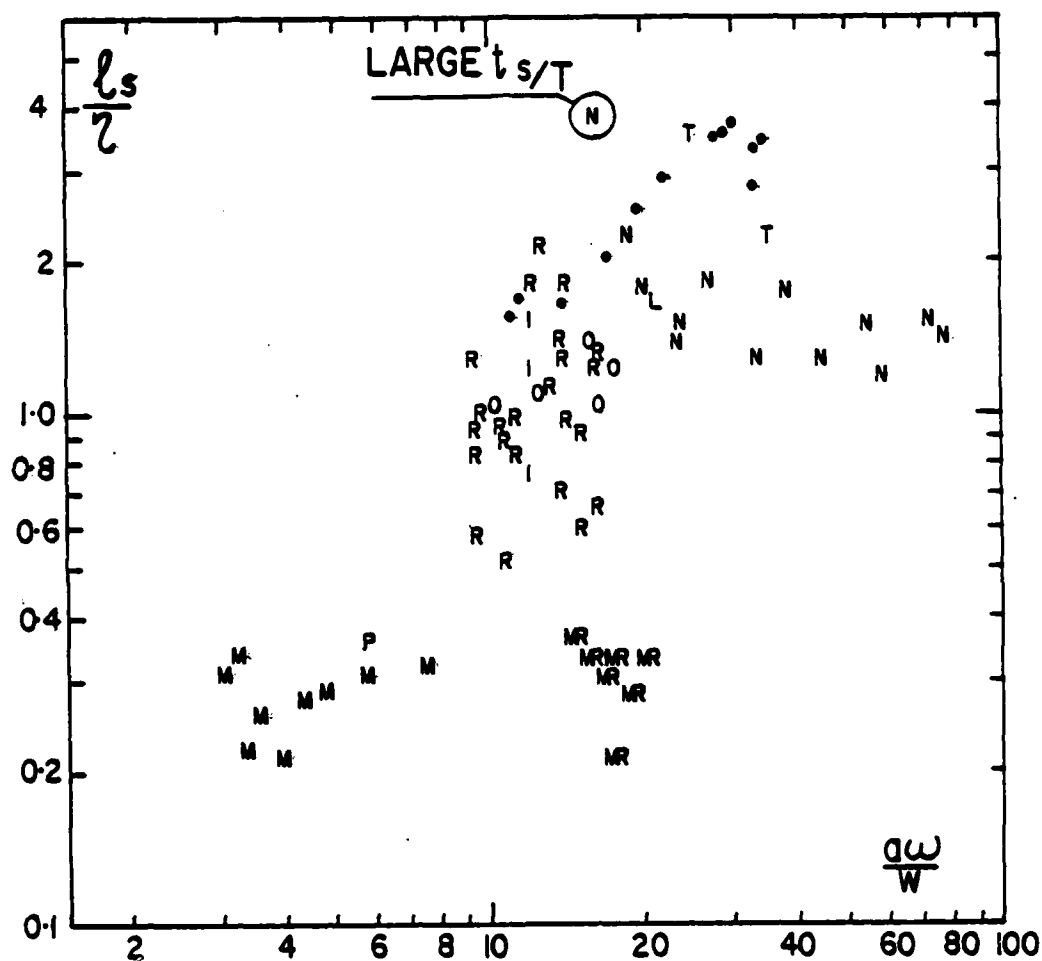


Figure 5.4: The relative vertical suspension length scale, l_s/η , as function of the velocity ratio $a\omega/w$. l_s/η grows with $a\omega/w$ between 3 and 10 as the vortex trapping becomes more efficient. l_s/η becomes constant for $a\omega/w \geq 10$, probably because the ripples get more rounded. If the ripple "sharpness" is maintained as in MacDonald's experiments (\circ), l_s/η may continue to grow.

When the ripple height is small ($\eta/a \leq 0.01$) as for the data marked (T) l_s/η will be large because l_s does not become substantially smaller than the total bed roughness.

Megaripples (MR) do not shed strong vortices, so the concentration profiles do not scale on the megaripple height but on the flat bed roughness.

Figure 5.4 shows λ_s/η versus aw/w . The main trend here is that λ_s/η increases with aw/w for $3 < aw/w < 10$, indicating that the vortex trapping mechanism gets more effective with increasing velocity ratio. For $aw/w > 20$, λ_s/η tends to decrease again, probably because the ripples get more rounded and less efficient vortex makers. The dots towards the upper right hand corner are measurements from MacDonald (1977) who used solid half circular "ripples" with just a small amount of loose sand around. These wooden "ripples" will of course maintain their shape and vortex making capability independent of aw/w so that λ_s/η can continue its upward trend. (The shown "MacDonald data" all have $\alpha/\eta > 14$. When α is smaller ($4.9 < \alpha/\eta < 13$) it seems to restrict the increase of λ_s/η somewhat).

The data marked "T" represents conditions where the relative ripple height (η/α) has decreased due to increasing ψ and θ' , and become smaller than the equivalent flat-bed-roughness, r . Under such conditions λ_s/η is again large because λ_s now scales on r .

The influence of t_s/T on λ_s/η is shown by the circled N-experiment in Figure 5.4 but possibly also by the experiments of Nakato et. al. which are marked I. Those experiments were performed with constant aw/w and three different periods: 1.2, 1.8 and 2.4 seconds. They show a considerable increase of λ_s/η with T which may be due to the related increase in $t_s/T \sim gT/w$.

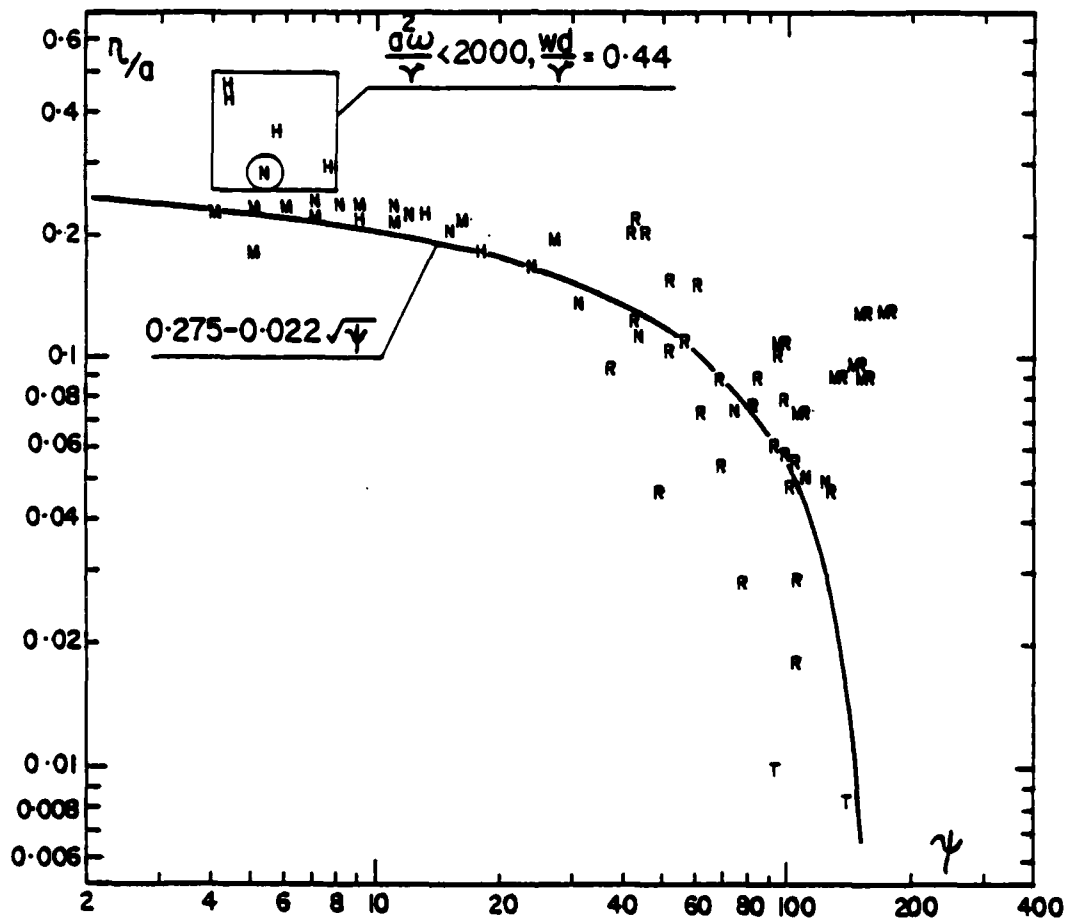


Figure 5.5: Observed relative ripple heights from the present field study and from some of the laboratory studies quoted. The curve represents the trend of all available laboratory experiments with quartz sand (Nielsen 1981). The bed forms referred to as megaripples have rounded crests and are not shedding vortices periodically. Extreme values of n/a (>0.25) tend to occur for small grain - and flow Reynolds numbers.

GRAIN SIZE VARIATION WITH ELEVATION OVER VORTEX RIPPLES

The profiles measured in tests 57 through 60 are very similar (see Figure 5.1), and it was thought reasonable to pool samples from the same elevation to get amounts big enough for a sieving analysis. The result of the sieving is shown in Table 5.2. The distributions from the four highest elevations are so similar that they could not be distinguished in a usual cumulative-distribution-plot. The distributions from the lower levels differ somewhat more, mainly with respect to the coarsest material ($d \geq 0.5$ mm), but the general picture is that the typical grain size (and settling velocity) varies much less with elevation than a diffusion model would suggest.

If the entrainment process was diffusion with $\epsilon(z)$ independent of grain size and if settling velocities were Γ -distributed with variation coefficient V at z_0 . Then, using the terminology introduced in section 4, we find that the mean settling velocity will vary with z as

$$\bar{w}(z) = \frac{\bar{w}(z_0)}{1+\sigma V} \quad (5.5)$$

where σ is the non dimensional elevation

$$\sigma = \int_{z_0}^z \frac{\bar{w}(z_0)}{\epsilon(z)} dz \quad (4.22)$$

The variation corresponding to (5.5) with $z_0 = 0.01$ m, $\bar{w}(z_0) = 0.053$ m/s, $V = 0.106$ and $\epsilon = 0.0043$ m²/s is shown in Figure 5.6 together with the observed values from Table 5.2. We see that the observed values are much more constant than equation (5.5) suggests, which indicates that

z	\bar{d} (mm)	\bar{w} (m/s)	M (g)	Percent of total sample from different fractions (mm)									
(m)				.063-.088	.088-.125	.125-.18	.18-.25	.25-.35	.35-.50	.50-.71	.71-1.0	> 1.0	
BED	.462	.061	67.62	.02	.03	.06	1.0	21	49	24.9	2.17	1.12	
.01	.390	.053	8.99	-	.07	.22	2.6	38	46	12.5	.89	.02	
.04	.389	.051	3.63	-	.08	.58	3.3	39	47	9.7	.30	-	
.08	.385	.051	3.58	-	-	.59	3.9	41	45	9.5	.42	-	
.12	.374	.049	2.12	-	.09	1.04	4.9	44	42	7.1	.33	.28	
.20	.359	.047	.666	-	.15	1.65	6.9	48	38	6.3	.15	-	
.28	.375	.049	.302	-	-	1.88	7.2	38	44	8.4	.31	-	
.36	.363	.047	.103	-	-	1.94	8.7	46	34	9.7	-	-	

Table 5.2: Results of sieving analysis of pooled samples from the bed and from the seven different intakes (RUNS 57, 58, 59 and 60).

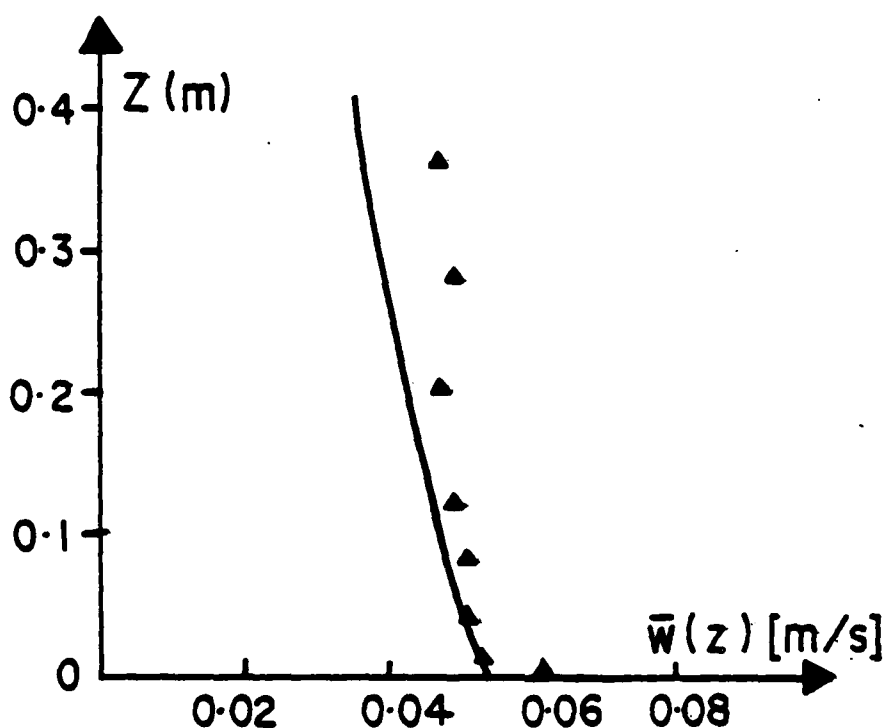


Figure 5.6: Predicted decrease of $\bar{w}(z)$ from diffusion model compared to the observed values (x). The observations show that $\bar{w}(z)$ is much more constant than the diffusion model predicts.

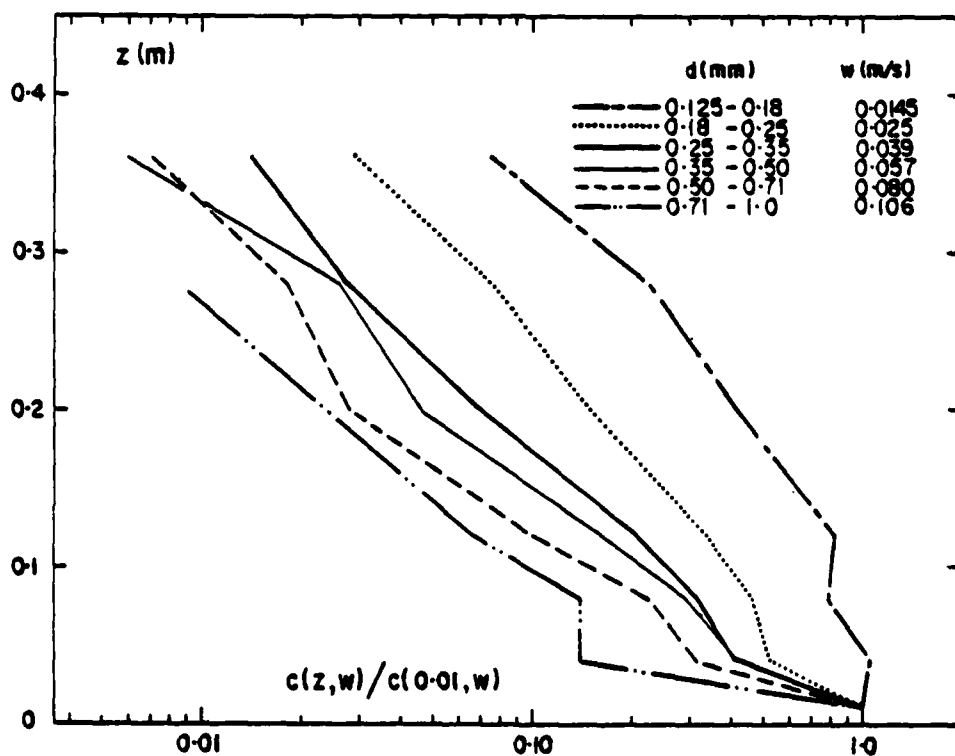


Figure 5.7: Concentration profiles for different sand fractions, normalized with respect to the value at $z = 0.01$ m. We note that all profiles are essentially similar at least for $z > 0.04$ m, irrespective of the large differences in settling velocity.

the distribution of individual size fractions are less dependent of settling velocity than the diffusion model predicts

$$\frac{d \ln \bar{c}}{dz} = - \frac{w}{\epsilon} \quad (5.6)$$

Another way of illustrating this is by plotting concentration profiles for individual size fractions and see whether they have different slopes in accordance with (5.6). This has been done in Figure 5.7 and we see that the differences in slope, especially above $z = 0.08m$ are much smaller than predicted by (5.6). In fact all the slopes are identical for $z > 0.8$, indicating that all grain sizes are distributed alike, irrespective of settling velocity. The mechanism responsible for this cannot be diffusion but must be a convective process where the sand grains travel with the released lee vortices after being trapped as explained in Chapter 3. The effect described above has been noticed before for example by Coleman (1970) who studied concentration profiles for different sand sizes in steady flow. Maintaining the diffusion terminology he concluded that big grains experience a much larger diffusivity than small ones in the same flow. It is more profitable however to discard the diffusion terminology when the flow has a pronounced vortex structure, like over ripples and behind dunes, and describe the concentration profile in terms of the length scale

$$l_s(z) = \left[- \frac{d \ln \bar{c}}{dz} \right]^{-1} \quad (5.7)$$

which is very similar to the corresponding length scale for vertical velocity fluctuations

$$Z_v(z) = \left[- \frac{d \ln v_{rms}}{dz} \right]^{-1} \quad (5.8)$$

as indicated by the measurements of MacDonald (1977) and Nakato et. al. (1977), see Figures 2.6 through 2.8.

Grain size variation with the distance from the bed under breaking waves was measured by Kana (1978) who found a more pronounced variation in average grain size between 10 and 60 centimetres above flat beds. This shows that the entrainment mechanism is different outside the wave boundary layer, under breaking waves, and probably more like diffusion.

CONCENTRATION PROFILES OVER FLAT BEDS

Flat beds of firmly packed sand are common in the surf zone of flat, dissipative beaches.

Under such conditions the concentration gradients are very large near the bed. Typically the concentrations will decrease by an order of magnitude over the lowest ten centimetres.

Figure 5.8 shows two profiles measured under very similar conditions at Seven Mile Beach, March 1982.

The suspended sand near a flat bed forms long stream parallel clouds twice every period near the velocity extremum in either direction; more dense under the stronger shoreward flow. These streaky clouds break up when the flow reverses and some of the sand travels to slightly higher elevations with the turbulent water, but most of the sand will have settled out before the next velocity extremum occurs and forms new clouds.

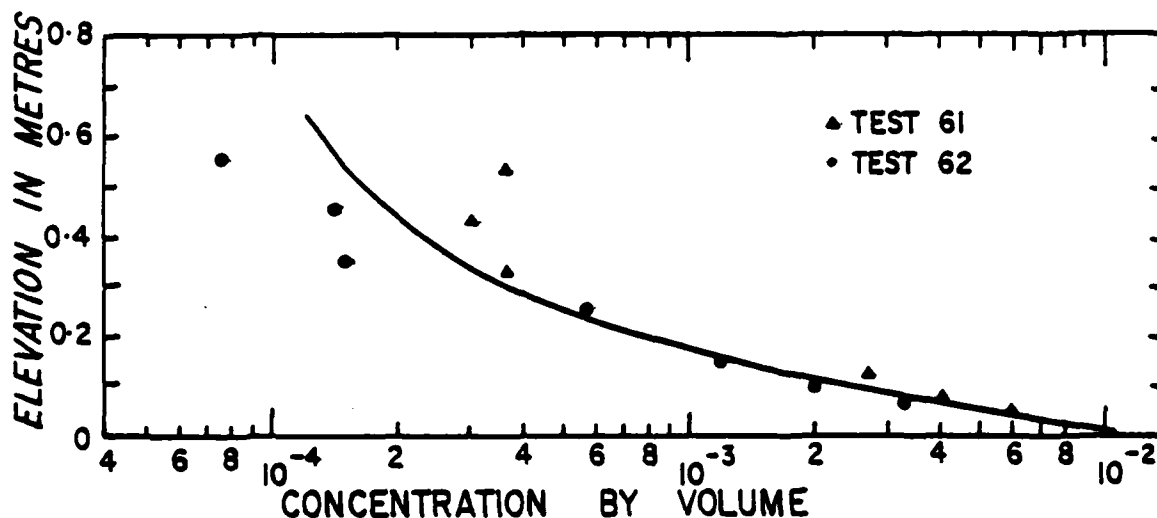


Figure 5.8: Concentrations measured over a flat bed under plunging breakers. The curve is the result of the fitting procedure described in connection with equation 4.13. $C_0 = 1.08 \times 10^{-2}$, $\epsilon_b = 1.86 \times 10^{-3} \text{ m}^2/\text{s}$, $\epsilon_s = 4.0 \times 10^{-2} \text{ m}^2/\text{s}$, $r^2 = 0.954$.

The width and thickness of the clouds is normally 3-5 centimetres under field conditions and results in vertical length scales of the same magnitude near the bed.

The structure of the sand clouds looks very similar to that of the "sublayer streaks" in steady flow. See Cantwell (1981). The characteristic l_s value of 3-5 centimetres is approximately equal to the hydraulic roughness, r given by equation (2.65) or about a hundred grain diametres.

The length scale will normally increase quite rapidly with distance from the bed. Under breaking waves, the increase is due to mixing induced by wave breaking and concentrations of the order of magnitude 10^{-4} may extend all the way to the surface. Under non breaking waves the steepening of the profiles occurs at much lower concentrations (of the order of 10^{-5}) which are made up mainly by the very finest fractions of the bed material, see Figure 5.9.

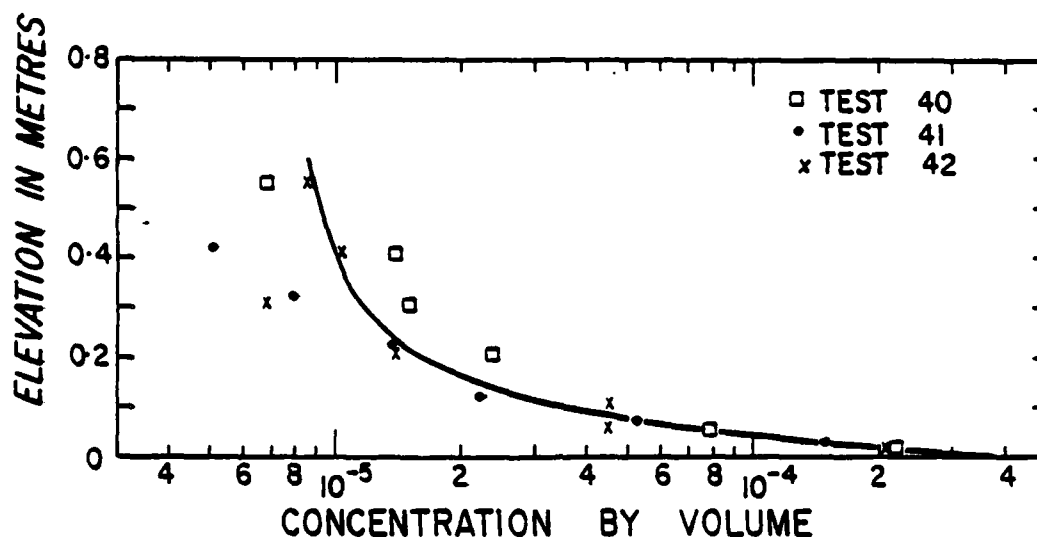


Figure 5.9: Sediment concentrations over a flat bed under non breaking waves. Under non breaking waves, the concentration magnitude will drop to somewhere between 10^{-4} and 10^{-5} before the profile gets steeper.

Figure 5.10 shows l_s/\bar{d} ($= \epsilon_B/w\bar{d}$) for all measurements carried out over flat beds or megaripples.

We see that the near bed length scale l_s determined from the curve fitting as ϵ_B/w , is generally about a hundred grain diameters or of the same magnitude as the hydraulic roughness, r , of a loose sand bed as derived from the friction measurements of Carlsens et. al. (1969) and Lofquist (1980)

$$r = 8\pi^2/\lambda + 190 \sqrt{\theta' - 0.05'} d \quad (2.65)$$

which gives

$$r/d = 190 \sqrt{\theta' - 0.05'} \quad (5.9)$$

for a flat bed.

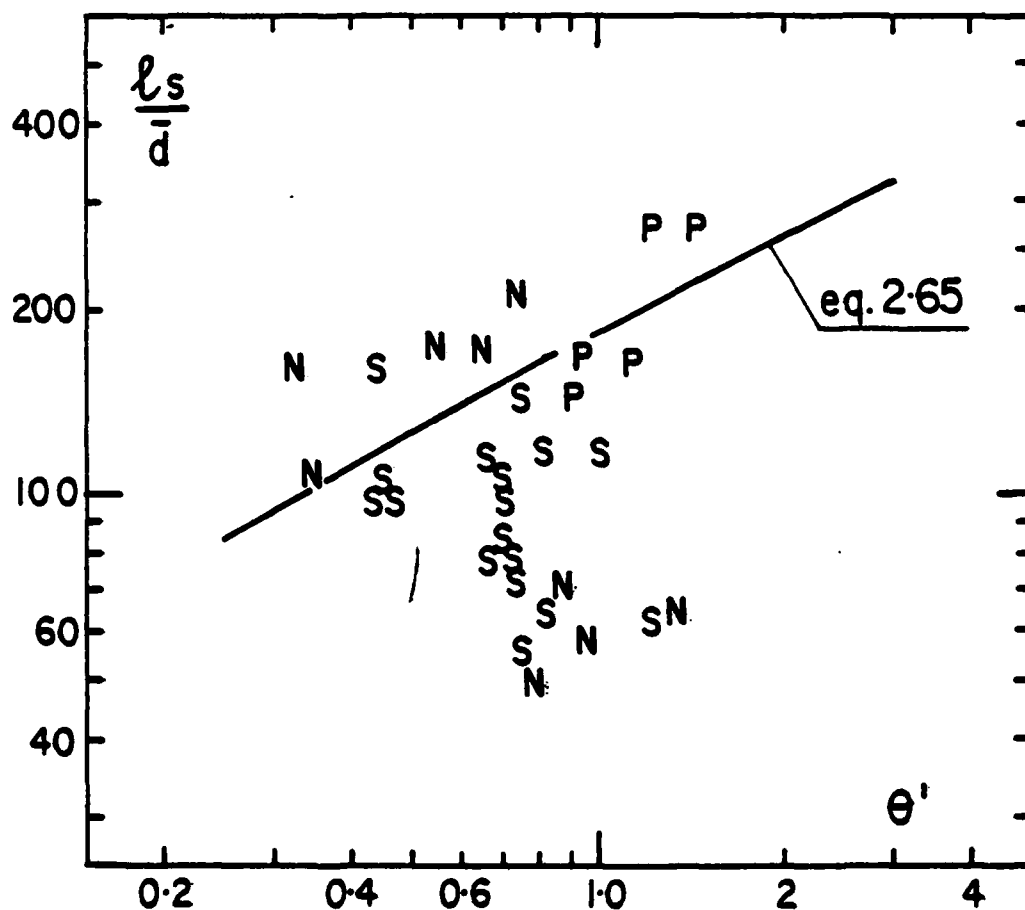


Figure 5.10: The value of l_s near the flat bed is about a hundred grain diameters or approximately equal to the hydraulic roughness given by equation (2.65). There is a slight tendency for plunging breakers (P) to give larger near bed length scales than spilling breakers (S) indicating that the turbulence of a plunging breaker penetrates further towards the bed.

The data in Figure 5.10 show no systematic trend and the relation between l_s and r may be expressed

$$l_s/r = 0.81 \pm 0.50 \quad (5.10)$$

The standard deviation is very large indeed and this is of course partly due to the fact that the sampler is not really designed for sampling over flat beds. There are too few intakes within the lowest ten centimetres, and it is very difficult to adjust and measure the elevation of the lowest intake with sufficient accuracy. There are however no other detailed measurements available at the moment as far as the author knows.

One might have expected the appropriate length scale to be the boundary layer thickness or the displacement thickness δ_1 rather than the roughness r , and indeed l_s/δ_1 is typically of the order of magnitude one.

However l_s does not seem to grow with a in the way δ_1 does. (For the relevant range of r/a we have $\delta_1 \sim a^{.75} r^{.25}$). Figure 5.11 shows l_s/δ_1 versus a/d for the same data as plotted in Figure 5.10.

The scatter is very large indeed, but we see the trend of l_s/δ_1 to decrease with increasing a/d , which probably means that l_s is fairly independent of a while δ_1 grows like a to a power between 0.25 and 0.75. (For the determination of δ_1 , see equations 3.61, 2.62 and 2.65).

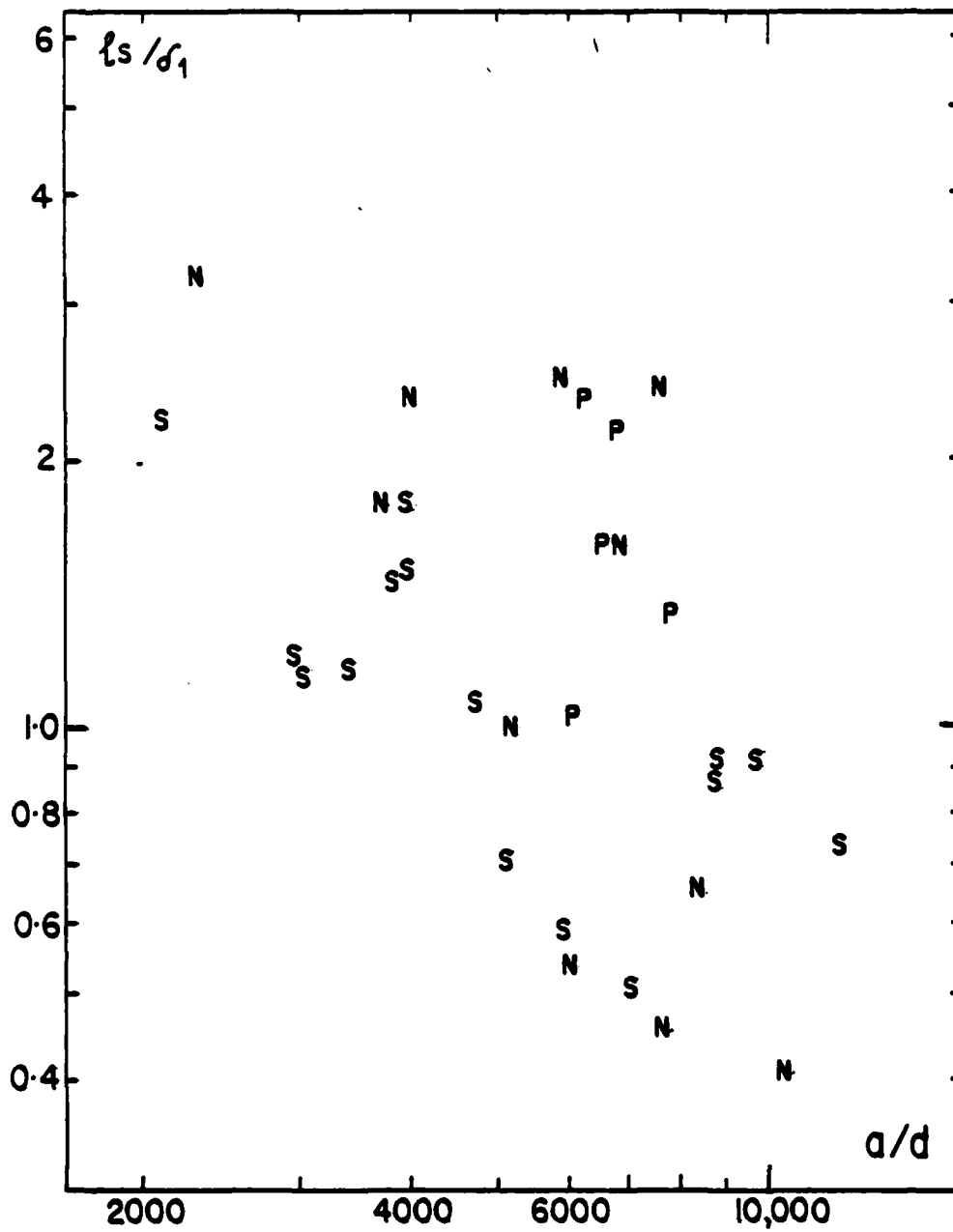


Figure 5.11: Relative near bed length scales, l_s/δ_1 as function of a/d from measurements over flat beds or megaripples. The height η of the megaripples is not included in the calculation of δ_1 .

CONCENTRATION PROFILES OVER MEGARIPPLES

When the bed forms are nicely regular like long crested vortex ripples the suspended sediment pattern is correspondingly regular, uniform in the longshore direction and periodic in the shore-normal direction. It is however quite common to find different, more irregular bed forms like megaripples and the suspended sediment pattern over them shows strong and complicated spatial and temporal variability.

Megaripples are irregular bedforms with typical heights of ten to thirty centimetres and lengths of one to two metres in the shore normal direction. The crest lengths are of the same order of magnitude as the crest to crest length, so the pattern is three dimensional and quite irregular.

The crests are very rounded compared to those of fully developed vortex ripples and there is no periodic formation of lee vortices. The suspension pattern is therefore in most places rather like that over a flat bed with sand entrained by turbulence bursts that form long streaks parallel to the wave motion and reaching heights comparable to the roughness length, r , of a flat sand bed. However in some places and under some waves large sand fountains are formed by strong vortices that are formed around the current maxima and released by the following flow reversal to travel upward carrying suspended sand up to elevations as high as one or two metres above the bed. Horizontal sections through the fountains will typically have diameters of 0.3 to 0.5 metres.

Megaripples are often non stationary with a continually changing pattern so the distribution of active (in the sense of

fountain making) spots is variable and similarly a spot which is at some time very active may in the matter of minutes become inactive.

Figure 5.12 shows two concentration profiles (Run 70 and 71) measured at the same location with half an hour interval. The bed was covered by megaripples and the waves were spilling breakers. Obviously the sampler intakes were close to an active spot during Run 71 and in a fairly inactive area during Run 70.

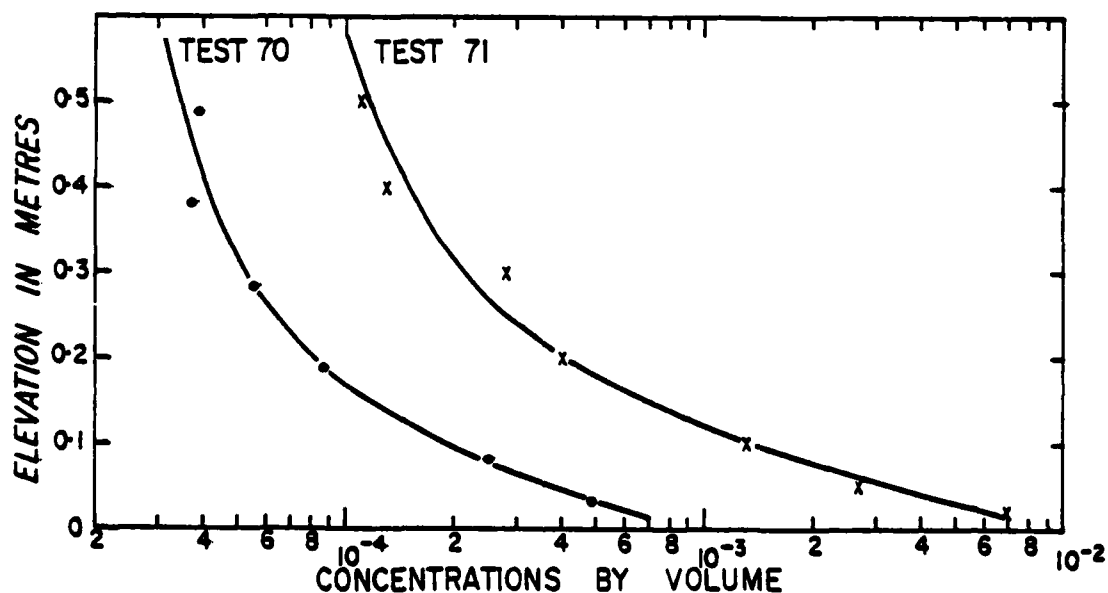


Figure 5.12: Two concentration profiles measured under identical wave conditions at the same location, over megaripples. The level of activity has changed considerably due to the temporal variation of the megaripple pattern.

Figure 5.13 shows time series of shore normal velocity at $z = 0.20\text{m}$ together with instantaneous sediment concentrations measured at $z = 0.04\text{m}$ near the sampling location of the two $\bar{c}(z)$ profiles shown in Figure 5.12. During the first three minutes of the record, the detector was at a very active spot where strong bursts of suspended sand were created by every second or third wave and then decayed over a twenty to thirty second period.

Over the last 3 minutes nothing much happened in the way of sediment suspension although the waves were unchanged. The active spot had died or moved on.

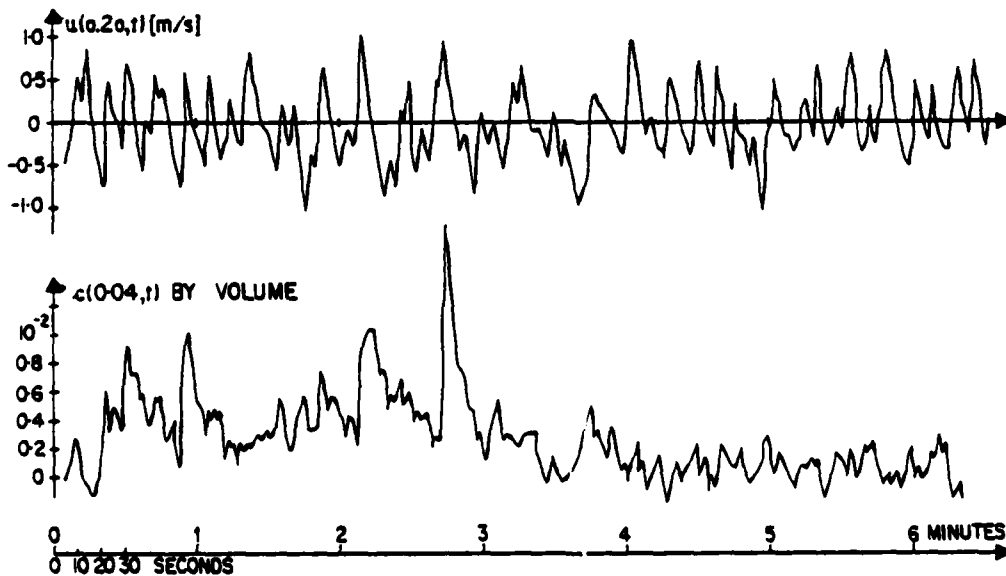


Figure 5.13: Simultaneous time series of shore normal velocities and instantaneous sediment concentrations. For the first 3 minutes, the area around the sediment detector was much more active than during the last half of the record. There is no corresponding change in the water motion, so the change must be due to changes in the megaripple topography. The instantaneous concentrations were measured via gamma radiation absorption by Alan Davison of the Australia Atomic Energy Commission.

The near bed sediment distribution over megaripples away from the active spots is similar to that over a flat bed. The shape of the upper part of the profiles is similar to that under breaking waves over flat beds and the present data does not enable us to distinguish the effects of breaking waves from those of sand fountains.

THE DIFFUSION APPROACH TO NEAR BED SEDIMENT DISTRIBUTIONS

The classical approach to suspended sediment phenomena is the gradient diffusion approach where the upward sediment flux is assumed proportional to the concentration gradient $\frac{\partial \bar{c}}{\partial z}$ and to the diffusivity ϵ , which may be a function of z but should be essentially independent of w and approximately equal to the eddy viscosity, ν_T , if diffusion of sediment is physically analogous to diffusion of momentum.

The distribution's dependence on w enters through the assumption of local equilibrium between the upward flux $\epsilon \frac{\partial \bar{c}}{\partial z}$ and the downward flux $w\bar{c}$. This equilibrium is expressed by the time averaged diffusion equation

$$\epsilon \frac{d\bar{c}}{dz} + w\bar{c} = 0 \quad (4.19)$$

It should be noted here that Nakato et. al (1977) found that there is no local equilibrium between time averaged upward and downward fluxes over ripples. The net flux is upward over ripple

crests and downward over the troughs. However the diffusion equation may still be applied in a space averaged sense. That is if \bar{c} is defined as the average over a ripple length.

If the diffusivity is essentially the same as the eddy viscosity it should be scaled by a typical velocity v_v and a typical length l_v of the boundary layer:

$$\frac{\epsilon}{v_v l_v} = \text{const} \quad (5.11)$$

Nielsen (1979) tested several relations of this type for the case of rippled beds with negative conclusions. The diffusion model does not apply over rippled beds because the dominating entrainment mechanism is convection through the entire boundary layer thickness of sand trapped in vortices. We have studied this process in previous sections.

The turbulence structure over flat beds is evidently different, so it is not clear a priori whether the entrainment process is mainly diffusion or convection. That is whether the distributions will be determined by a diffusivity, given by the turbulence structure

$$\epsilon \sim v_T^3 \quad (5.12)$$

leading to different length scales ϵ/w for different grain sizes, or the distributions of all grain sizes will have a common vertical length scale, l_s , determined by the boundary layer structure.

We have found in the previous section that a common length scale namely the bed roughness applies pretty well:

$$\frac{z_s}{r} = 0.81 \pm 0.50 \quad (5.10)$$

in accordance with a convection model.

However the scatter is very considerable and in fact a diffusion model, assuming

$$\frac{\epsilon_B}{u_* \delta_1} = \text{constant} \quad (5.13)$$

does not fall through completely on the basis of the present data.

Figure 5.14 shows $\epsilon_B/u_* \delta_1$ versus w for the same megaripple - (MR) and flat bed data (F) that were used in Figure 5.10. We see that the typical magnitude of $\epsilon_B/u_* \delta_1$ is around 0.3 which we would expect in view of Jonsson and Carlsen's eddy viscosity measurements that are shown in Figure 2.20. However, there is a significant tendency for the observed eddy viscosities to increase with w . This is evidence in favour of the convection process because the universal (= independent of w) length scale z_s of the convection model corresponds to ϵ_B being proportional to w :

$$\epsilon_B = w z_s \quad (5.14)$$

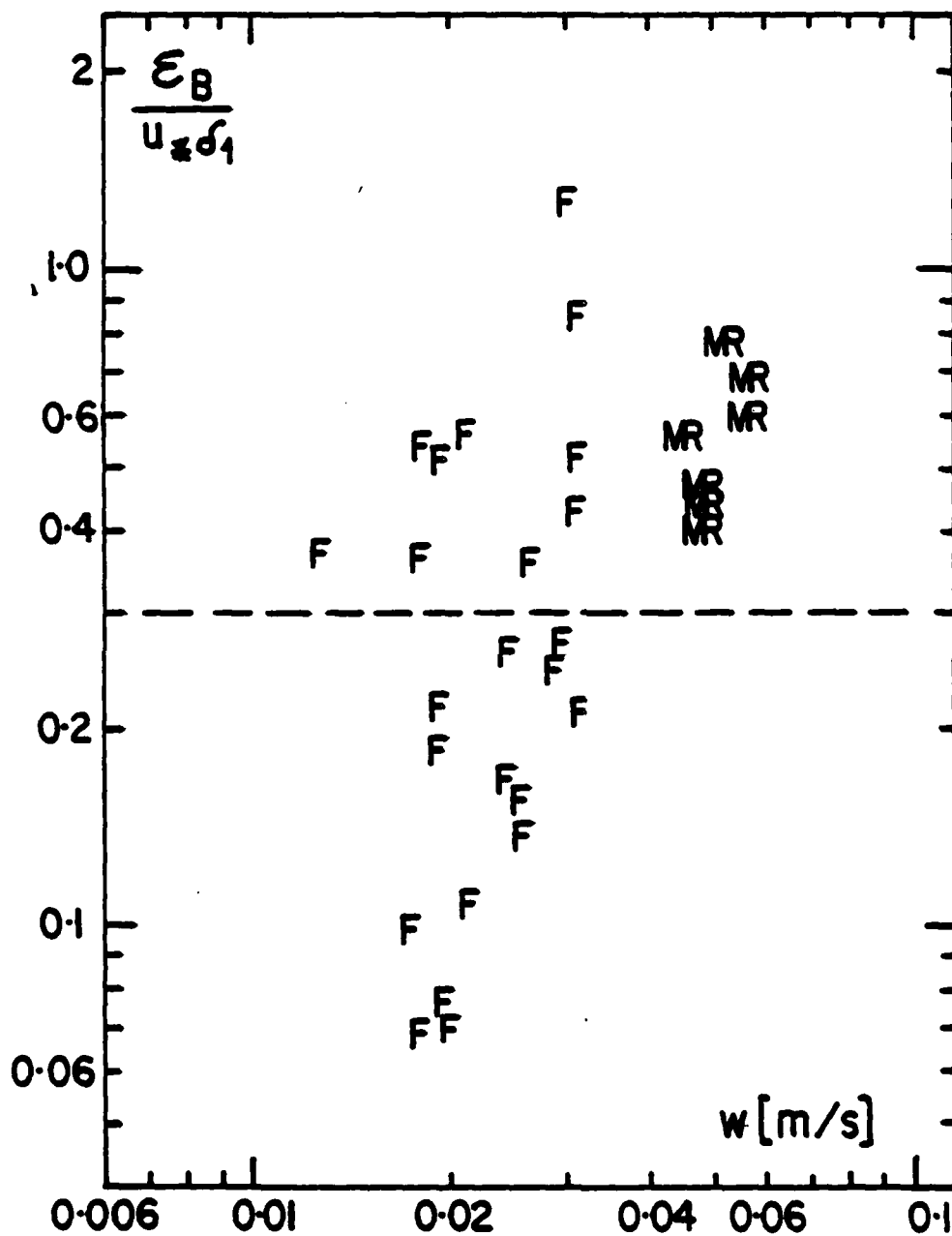


Figure 5.14: Measured relative diffusivities for flat bed (F) and megaripple (MR) data. The typical magnitude is 0.3 which one would expect from Jonsson and Carlsen's eddy viscosity measurements; but the observed diffusivities increase with w , which indicates that the entrainment process is really convective.

CONCENTRATION MAGNITUDE

The concentration magnitude is determined by C_0 which is defined as the time averaged concentration (by volume) at the ripple crest level and it is determined experimentally by extrapolation of the fitted profiles given by 4.10 or 4.13 to the level $z = 0$.

It is natural to expect C_0 to depend mainly on the ratio between moving τ (= shear stress) and stabilizing forces on the bed sediment particles.

This ratio is expressed by the Shields parameter

$$\theta = \frac{\tau}{\rho g (s-1) d} = 0.5 f_w \psi \quad (5.15)$$

The form drag on ripples and other bedforms is unlikely to influence the motion of individual grains so roughness due to bed form geometry i.e. the first term of equation 2.65, should not be included in the calculation of the Shields parameter. The roughness due to moving grains is mainly a function of θ' as we found in connection with (2.65) so any effect of moving-grain-roughness is automatically included if we assume a relation of the following form

$$C_0 = F(\theta') \quad (5.16)$$

where

$$\theta' = \frac{\tau'}{\rho g (s-1) d} = \frac{1}{2} f_w' \psi \quad (5.17)$$

and f_w' is calculated as f_w from (2.62) with $r = 2.5d$.

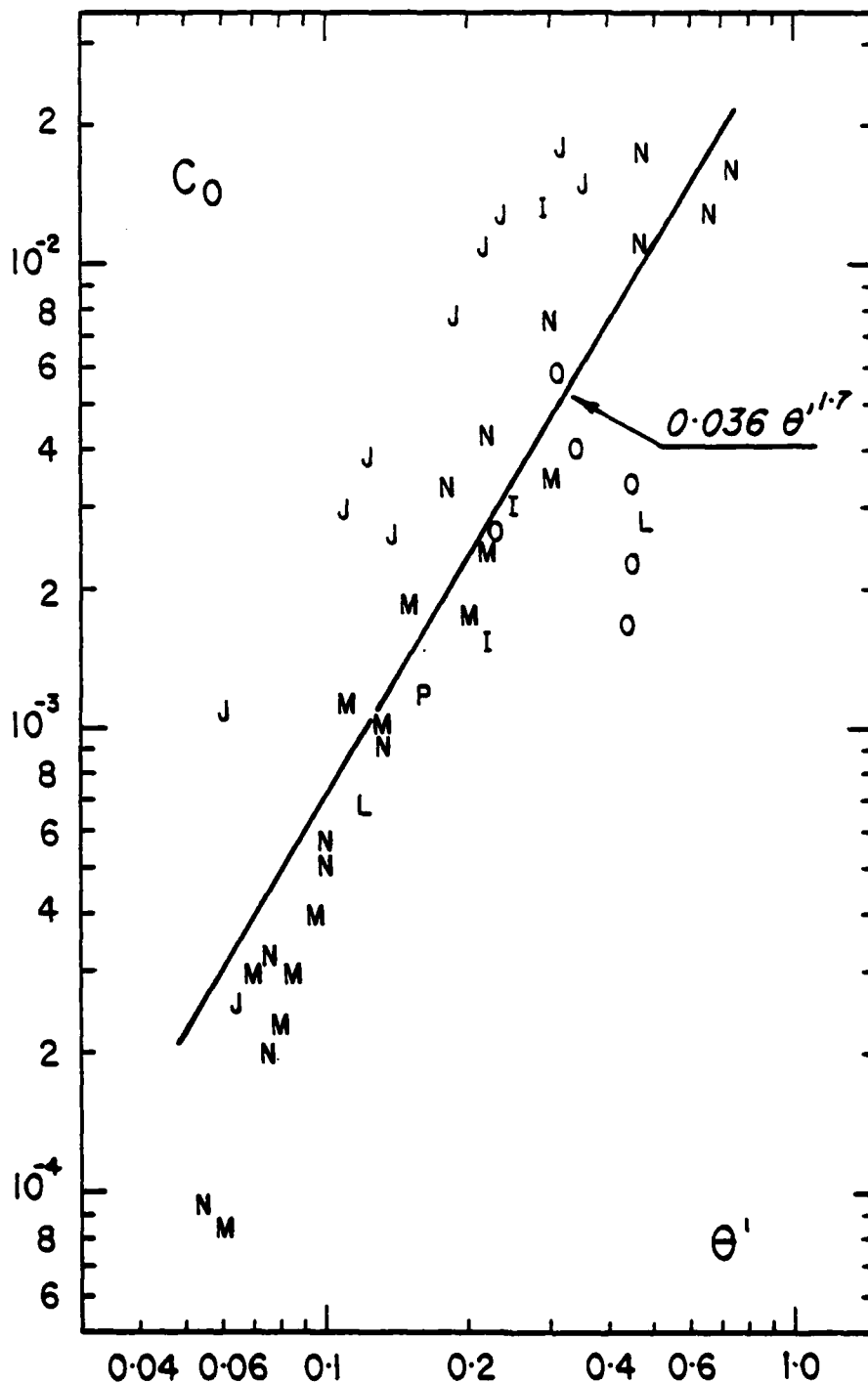


Figure 5.15: C_0 , measured over ripple crests, as function of θ' for all available laboratory data. Different grain sizes follow the same trend (M, N), but experiments with longer periods tend to fall lower than those with short periods (I). The results of Homma et. al. (1965) fall consistently above the rest for unknown reasons.

Figure 5.15 shows C_o as function of θ' for all available laboratory data. The concentrations measured by Homma et. al., (J), are generally three to four times larger than the main line of the rest which remains unexplained. They were measured by the same kind of optical device as used by Nakato et. al. (I). The very different grain diameters (0.082 - 0.55 mm) used by Nielsen (1979) follow the same trend, so the variation of relative grain size (a/d) is properly accounted for. However there is a significant tendency for data with longer periods or higher flow Reynolds numbers ($a^2\omega/\nu$) to fall below those with smaller Reynolds numbers. See for example the data of Nakato et. al. that are marked "I". The three experiments were carried out with the same sand and the same velocity amplitude ($a\omega$) but with different periods: 1.2, 1.8, and 2.4 seconds and correspondingly different Reynolds numbers: 1.4×10^4 , 2.1×10^4 , and 2.7×10^4 .

The power function

$$C_o = 0.036 \theta'^{1.7} \quad (5.18)$$

is found by log-log linear regression and redrawn in Figure 5.16 to illustrate the fact that all the field data fall significantly below the main stream of the laboratory data. The field data correspond to much longer periods than the laboratory data, typically 8 seconds as opposed to 2 seconds, and will therefore have much larger Reynolds numbers for the same θ' . The discrepancy between experiments with different Reynolds numbers is caused by the way in which θ' is calculated. The use of equation (2.62) assumes rough turbulent flow

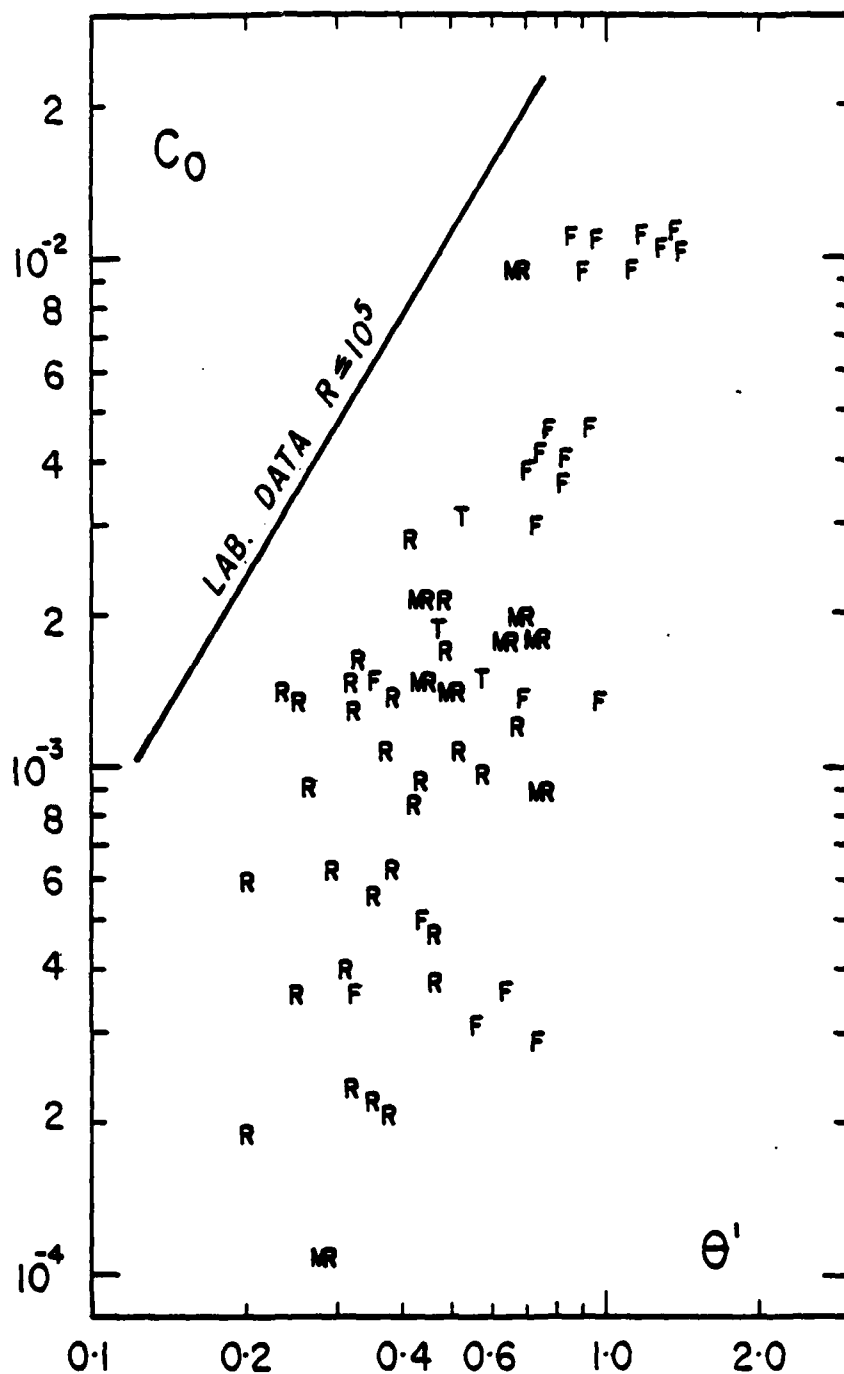


Figure 5.16: C_0 versus θ' for field data. The trend is the same for ripples, megaripples and flat beds (R, MR and F) but all field data fall significantly below the line given by (5.18), which represents the general trend of the laboratory data.

conditions, while viscous effects are probably still quite important in most of the laboratory experiments. The viscous contribution to the friction factor may be roughly estimated by

$$f_w = 2 \left(\frac{\alpha^2 \omega}{\nu} \right)^{-0.5} \quad (2.53)$$

which we derived above for laminar flow over a smooth bed. This will be considerably larger than the values derived from (2.62) for small scale experiments and therefore the proper Shields parameter for the laboratory experiments is larger than θ' . In Figure 5.17 the laboratory data have been moved to the right, to closer agreement with the field data by including viscous effects in the friction factor and the Shields parameter in the following way. For the friction factor we use the combined formula

$$f_* = f_e + 2 \left(\frac{\alpha^2 \omega}{\nu} \right)^{-0.5} \exp \left(-10^{-5} \frac{\alpha^2 \omega}{\nu} \right) \quad (5.19)$$

and get the revised Shields parameter

$$\theta_* = 0.5 f_* \psi \quad (5.20)$$

The Reynolds numbers for field data range roughly between 10^5 and 10^6 so in their case θ_* is practically identical to θ' . The scatter is still very large, especially towards the lower values of C_o and unfortunately it is real. As mentioned in connection with Figure 5.12 the concentrations can be an order of magnitude different due to details in the bed form topography under the same waves and with the same bed sediment, so if we are looking at general relations

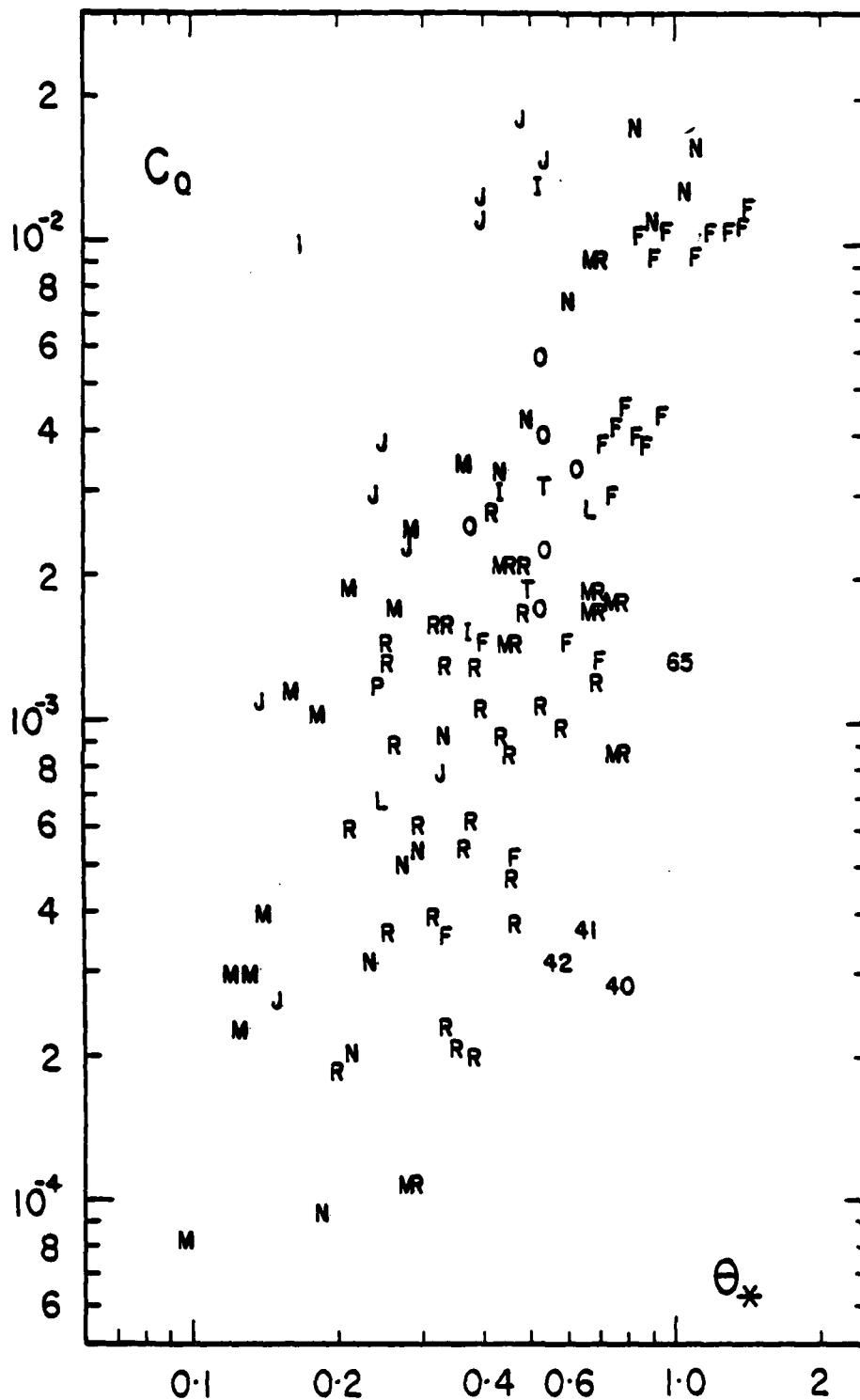


Figure 5.17: C_Q as function of θ_* for field and laboratory data. The major deviations from the main trend are found for the laboratory measurements of Homma et. al (J) and for field measurements over hard, flat beds at moderate values of the Shields parameter (40, 41, 42 and 65).

between Shields parameter and concentration magnitude we must expect this kind of scatter for beds covered with irregular bed forms.

For flat beds and rippled beds with samples consistently taken over the ripple crest, we might expect a somewhat smaller scatter and that is generally what we find. However over some flat beds of fine sand we tend to find concentrations that are extremely small compared to the general trend. Such concentrations were found in experiments 40, 41, 42 and 65 at Seven Mile Beach. The fine sand ($\bar{d} \approx 0.17$ mm) was very firm to stand on, nearly like solid concrete, the bed was completely flat and nearly no sediment motion occurred although the Shields parameter was larger than 0.55. That is an order of magnitude larger than the conventional critical value for the onset of sediment motion ($\theta_c \approx 0.05$).

INFLUENCE OF WAVE BREAKING ON CONCENTRATION PROFILES

The wave boundary layer turbulence decays very rapidly with distance from the bed as described by Tunsdall and Inman (1975) and measured by MacDonald (1977) and Nakato et. al. (1977), see Figure 2.19. The data support the following rough estimate of the scale of turbulent velocities

$$v_{rms} \approx 0.9 u_* e^{-z/4.5 \delta_1} \quad (2.81)$$

This means that the suspended sediment distribution outside the boundary layer ($z \geq 5\delta_1$) is likely to be determined by entrainment and mixing due to sources such as wave breaking.

Different types of breaking waves are likely to generate mixing of vastly different character and strength. Waves that plunge heavily on shallow bars or on the step of steep beaches can form very strong jets, that penetrate right through to the bed and thus introduce very strong external turbulence into the boundary layer itself.

The jet is also able to inject large amounts of entrained air into the boundary layer, and when this air rises, it generates large localized, upward water velocities that act as very efficient elevators for suspended sand. The magnitude of the vertical water velocities, generated in this way can be estimated from the typical heights, Z , reached by the water and sand dragged up by the escaping air.

It is not uncommon to see splashes of white or brownish water rise about a metre above the local water level shortly after a wave has plunged.



Figure 5.18: Big waves ($H_B \approx 1.5\text{m}$) plunging on a shallow bar. The arrow shows plumes of sandy water, dragged up by escaping air.



Figure 5.19: Big waves plunging onto the step of a steep reflective beach (Pearl Beach, North of Sydney). The jets of water, thrown upwards by escaping air are about one metre high.

The relation between starting velocity v_o and culmination height Z is

$$v_o = \sqrt{2gZ} \quad (5.21)$$

so even with a conservative estimate of $Z = 0.5$ m we find

$$v_o = 3 \text{ m/s} \quad (5.22)$$

which is a hundred times the typical sediment settling velocities. These large velocities of course are concentrated around large escaping air pockets and of short duration but they dominate the sand entrainment in the areas around the plunge point. The described process may create some very strange looking concentration profiles when the rising plumes spread along the surface above areas with little sediment motion. Then one may observe that the concentrations increase toward the surface.

Mixing due to spilling breakers and bores has a very different character. The writer once observed the effect of spilling breakers in a wave tank ($T = 1.7$ s, $h = 0.40$ m, $H = 0.2$ m, $d = 0.082$ mm) at the Institute of Hydrodynamics and Hydraulic Engineering (ISVA), Technical University of Denmark, during the following experiment: At first the waves were not breaking and the suspended sand formed a well defined layer over the rippled bed, only a few centimetres thick. Then the amplitude of the wave generator was slightly increased so that the waves began to break and passed over the test section as gently spilling breakers, the wave height being practically unchanged.

The suspension distribution was *unchanged* for four or five wave periods after the onset of wave breaking. Then it changed very rapidly and apparently reached a new equilibrium with considerable concentrations throughout the water column. The transition took only about two wave periods (from a visual judgement).

When the wave maker was turned down again so that the waves stopped breaking, the old equilibrium with clear water above a few centimetres of dense suspension was reestablished in about ten wave periods time.

The two above mentioned situations of the heavily plunging wave and the gently spilling one are the extremes with respect to breaker introduced mixing, and their effects on the sediment distribution in general and on the boundary layer in particular are probably very different.

The laboratory measurements shown in Figure 5.20 are from under non breaking waves and spilling breakers of the same height. The breaker turbulence has obviously changed the upper part of the profile drastically; but the lower part, that is C_0 and l_s are unchanged, so the concentration magnitude and the near bed vertical length scale l_s are the same under spilling breakers as under on breaking waves. This tendency is not contradicted by the field measurements of the present study. See Figure 5.10.

None of the field experiments referred here we carried out under really heavily plunging waves. All the experiments marked "P" for plunging in Figure 5.10 were performed on flat straight beaches where the upwelling of sand with entrained air never becomes as well developed on shallow bars for example. Nevertheless there is a tendency for the "P"-experiments to fall above the

average in Figure 5.10 indicating some injection of breaker turbulence into the Boundary layer.

A theoretical treatment of sediment dispersion due to wave breaking does not seem possible at the moment although some information about the turbulence structure can be gained from such studies as Miller (1976), Peregrine and Svendsen (1979), Madsen (1981) and Thompson (1982). Neither is it possible to derive precise quantitative information concerning the upper part of the concentration profiles on the basis of presently available data. A detailed quantitative description would require a comprehensive laboratory study where such things as break point and breaker type can be clearly defined. These are never constant nor well defined in the field. It will also be necessary to start with very uniform sediment, so that the effects of settling velocity variability are eliminated in the first place.

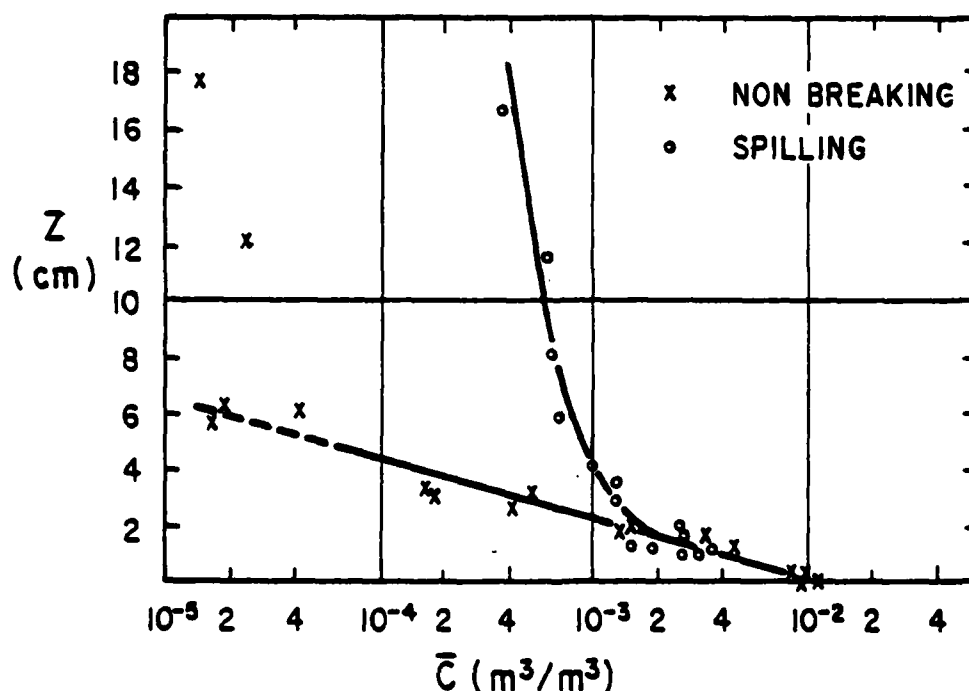


Figure 5.20: Concentrations measured under spilling breakers and non breaking waves of the same height, from Nielsen (1979), $h = 0.4m$, $T = 1.7s$, $H = 0.19m$, $\bar{d} = 0.082mm$. The spilling does not change concentration magnitude or profile slope inside the boundary layer ($Z \leq 2cm$); but it changes the profile completely at higher elevations.

INFLUENCE OF CURRENTS ON CONCENTRATION PROFILES

In none of the field experiments of the present study did the steady current influence the suspended sediment concentrations significantly. That is, none of the data show a significant tendency for C_0 to be larger or the distribution to be different due to a stronger relative steady current.

The relative strength of the steady current is defined here as

$$V_R = (\bar{u}^2 + \bar{v}^2) / (aw)^2 \quad (5.23)$$

where the mean current components \bar{u} and \bar{v} are shore parallel and shore normal respectively and \bar{u} is generally measured 0.2m above the bed while \bar{v} is measured at 0.3m.

The range of V_R in the experiments carried out over the rippled bed in the bar trough at Eastern Beach, Gippsland was 0.02 to 0.19 with the steady current being predominantly shore parallel. The strongest longshore current was 0.32m/s in Test 54, measured 0.25m above the bed. The current velocity at the surface was about 0.5m/s which is a very considerable current to work in. Nevertheless the ripples on the bed were apparently not affected by the current at all. They were sharp crested, shore parallel and symmetrical, just like under a pure wave motion. This shows that it takes a very strong longshore current to change the bed form geometry, the boundary layer structure or the sediment entrainment process over a rippled bed.

The wave boundary layer and bed forms seem to be somewhat

more sensitive to shore normal currents like rip currents. From visual observations it seems that even a weak rip current ($V_R \approx 0.05$) tends to change the bed forms into asymmetrical dunes with somewhat larger length than vortex ripples and with no vortex shedding from the landward slope. Unfortunately we did not succeed in getting any concentration measurements from rip currents. This is of course due to the fact that rip currents are very difficult to work in. The laboratory studies of Brevik and Aas (1980) and Kemp and Simons (1982) have revealed important details about the boundary layer under waves and a strong "shore normal" current over a solid rippled bed. But the response of a loose sand bed to such flows is definitely worth a study as well.

SHORENORMAL SEDIMENT TRANSPORT

Prediction of sediment transport under waves and a current is a very complicated matter and at present there is not model in existence which is both theoretically based and in agreement with experimental evidence.

As early as 1963, Inman and Bowen showed that the net sediment transport under waves and a codirectional current will just as often be against the net current as with it.

This means that no transport model by which the net transport has the direction of the net flow will be in general agreement with the empirical evidence.

More such evidence has since been obtained by many detailed flume experiments at the Technical University in Delft; see van de Graff (1980). All of these experiments as well as those of Bowen and Inman were carried out over rippled beds, with relatively weak currents.

The explanation for the tendency of the net transport direction to be opposite to that of the strongest instantaneous current lies in the way sand is entrained over ripples (see the illustrations of Bijker et. al. 1976): The sand that is picked up by the velocity in say, the shoreward direction is trapped in the lee vortex and thus not effectively moved until the vortex is released by the flow reversal and carried seaward by the following seaward current. In this way the weaker offshore current carries larger concentrations which is likely to result in net seaward transport because concentrations grow rapidly with the entraining velocity (like u^4 or u^6). The picture is of course different when the current becomes so strong that the flow never reverses through

most of the water column. Further complication is added by the fact that waves and steady currents have very different abilities to penetrate the lower layers where the concentrations are largest. Recent laboratory studies by Brevik and Aas (1980) and Kemp and Simons (1982) give good details about the current distributions under waves, over solid rippled beds, however it must be borne in mind here that the bed forms in for example rip currents are very different from ripples and this may change the turbulence structure and the current distribution.

For quantitative description of the sediment transport it is appropriate to write both velocities and concentrations as Fourier series

$$u(z,t) = \operatorname{Re} \left\{ \sum_0^{\infty} U_m(z) e^{im\omega t} \right\} \quad (5.24)$$

$$c(z,t) = \operatorname{Re} \left\{ \sum_0^{\infty} C_m(z) e^{im\omega t} \right\} \quad (5.25)$$

since the whole process must be periodic. In general $U_m(z)$ and $C_m(z)$ are complex numbers of which the argument determines the phase shift relative to the fundamental mode of the waves.

The net sediment flux through a vertical element dz at elevation z is then

$$\sum Q_m(z) dz = \sum |U_m(z)| |C_m(z)| \cos \phi dz \quad (5.26)$$

where ϕ is the local phase shift between U_m and C_m given by

$$\phi = \text{Arg} \{U_m(z)\} - \text{Arg}\{C_m(z)\} \quad (5.27)$$

This dependence of the sediment flux on local phase relations is a central problem in non steady sediment transport modelling and as yet there is not model which is capable of predicting these phase relations on theoretical grounds.

The model presented by Nielsen et al. (1978) and Nielsen (1979) predicts these phase relations as well as net sediment fluxes that are in agreement with the Dutch measurements, with appropriate choice of parameters. However, this model is based on the diffusion equation, and as we found earlier in this section the entrainment process especially over ripples is not a diffusion process.

SHORE PARALLEL SEDIMENT TRANSPORT

In the direction perpendicular to the wave motion the problem is not so complex because there are no oscillatory velocity components (except for maybe pulsation of longshore currents at surf beat frequency) so the total sediment flux is simply

$$Q = \int_0^h \bar{v}(z) \bar{c}(z) dz \quad (5.28)$$

The evaluation of $\bar{c}(z)$ and $\bar{v}(z)$ is not straight forward however. The concentration, $c(z)$ will in general be a function of \bar{u} and \bar{v} as well as of ω although the dependence on \bar{u} and \bar{v} seems to be rather weak and is in fact hidden in the scatter of the presently available field data.

Our ability of predict the longshore current distribution is also very limited. Two rather recent models for wave current boundary layers are those of Grant and Madsen (1979) and Christoffersen (1982). The first model assumes that the eddy viscosity grows linearly both inside and outside the wave boundary layer while the latter assumes a constant ν_T in the boundary layer. The second model is much simpler to work with and in fact the measurements of Kemp and Simons (1982) show that under their experimental conditions ν_T is more like a constant than anything else inside the wave boundary layer.

None of the two models considers the possibly vast importance of the orientation of the vortices over rippled beds. This orientation may however lead to very different eddy viscosities

felt by flow in the shore parallel and the shore normal direction. Strong vortices with shore parallel axes will probably cause much more resistance to longshore currents than to shore normal ones.

The general behaviour of bed forms under combinations of waves and currents is also virtually unknown so far. We only know that they look very different under rip currents and longshore currents of the same strength relative to aw .

REFERENCES

- BAGNOLD, R.A. (1946): Motion of Waves in Shallow Water: Interaction Between Waves and Sand Bottoms. Proc. Roy. Soc. London, A. Vol. 187, pp. 1-15
- BIJKER, E.W., E. VAN HIJUM and P. VELLINGA (1976): Sand transport by Waves. Proc. 15th Int. Conf. Coastal Eng., Hawaii pp. 1149-1167
- BOSMAN, J.J. (1982): Concentration measurements under oscillatory water motion: Report on model investigation M 1695, Part II, waterloopkundig laboratorium, delft hydraulics laboratory.
- BREVIK, I. and AAS, B. (1980): Flume Experiment on Waves and Currents. I. Rippled Bed. Coastal Engineering, No. 3 pp. 149-177
- CACCHIONE, D.A. and DRAKE, D.E. (1982): Measurements of Storm-Generated Bottom Stresses on the Continental Shelf. Journal of Geophysical Research, Vol. 87, No. C3, pp 1952-1960
- CANTWELL, B.J. (1981): Organized Motion in Turbulent Flow. Ann. Rev. Fluid Mech. pp 457-515
- CARSTENS, M.R., NEILSON, F.M. and ALTINBILEK, H.D. (1969): Bed Forms Generated in the Laboratory under Oscillatory Flow, Coastal Engineering Research Center, Technical Memo 28, Washington D.C.
- CHRISTOFFERSEN, J.B. (1982): Current Depth Refraction of Dissipative Water Waves. Series Paper 30, Institute of Hydrodynamics and Hydraulic Engineering, Technical University of Denmark.
- COLEMAN, N.L. (1970): Flume studies of the sediment transfer coefficient. Water Resources Res., Vol. 6, No. 3, pp. 801-809
- DU TOIT, C.G. and J.F.A. SLEATH (1981): Velocity Measurements Close to Rippled Beds in Oscillatory Flow. Journal of Fluid Mechanics Vol. 112, pp. 71-96
- FAIRCHILD, J.C. (1959): Suspended Sediment Sampling in Laboratory Wave Action, CERC, BEB Tech. Memo 115
- FAIRCHILD, J.C. (1977): Suspended Sediment in the Littoral Zone of Ventnor, New Jersey, and Nags Head, North Carolina. CERC Tech. Paper No. 77-5
- GRAAFF, J. van de and W.M.K. TILMANS (1980): Sand transport by waves Proc. 17th Int. Conf. Coastal Eng., Sydney, pp 1140-1157
- GRANT, W.D. and MADSEN, O.S. (1979): Combined wave and current interaction with a rough bottom. Journal of Geophysical Research, Vol. 84, No. C4, pp 1797-1808

- GRANT, W.D. and O.S. MADSEN (1982): Movable bed roughness in unsteady oscillatory flow. *Journal of Geophysical Research*, Vol. 87, pp. 469-481
- HO, H.W. (1964): Fall velocity of a sphere in an oscillating fluid. PhD Thesis, University of Iowa
- HOMMA, M., HORIKAWA, K., and KAJIMA, R. (1965): A study of suspended sediment due to wave action. *Coastal Engineering in Japan*, Vol. 8, pp. 85-103
- HORIKAWA, K., and WATANABE, A., (1967): A Study of sand movement due to wave action. *Coastal Engineering in Japan*, Vol. 10, pp 39-57
- INMAN, D.L. and A.J. BOWEN (1963): Flume experiments on sand transport by waves and currents. *Proc. 8th Int. Conf. Coastal Eng.* pp 137-150
- JENKINS, B.S. (1973): Studies of the Flow of a Fluid with Density Differences caused by Turbidity, Report No. 133, Water Research Laboratory, University of New South Wales, Manly Vale
- JONSSON, I.G., Wave Boundary Layers and Friction Factors, *Proc. 10th International Conferences on Coastal Engineering*, Tokyo 1966, Chapter 10.
- JONSSON, I.G. (1980): A New Approach to Oscillatory, Rough Turbulent Boundary Layers. *Ocean Engineering*, Vol. 7, pp 109-152
- JONSSON, I.G. and CARLSEN, N.A. (1976): Experimental and Theoretical Investigations in an Oscillatory Rough Turbulent Boundary Layer, *Journal of Hydraulic Research*, Vol. 14, No. 1, Mar. 1976, pp. 45-60
- KAJIURA, K. (1968): A model of the bottom boundary layer in water waves. *Bull. Earthquake Res. Inst. Univ. of Tokyo*, Vol. 46, Chapter 5, pp. 75-123
- KALKANIS, G. (1964) Transport of bed material due to wave action. CERC, Tech. Memo No. 2
- KAMPHUIS, J.W. (1975): Friction Factors Under Oscillatory Waves. *Proc. A.S.C.E.*, Vol. 102, WW2, pp. 135-144
- KANA, T.W. (1979): Suspended Sediment in Breaking Waves. Tech. Rep. No. 18-CRD, Department of Geology, University of South Carolina.
- KEMP, P.H. and SIMONS, R.R. (1982): The interaction between waves and a turbulent current: waves propagating with the current. *Journal of Fluid Mechanics*, Vol. 116, pp. 227-250
- KENNEDY, S.K., R. EHRLICH and T.W. KANA (1981): The Non-normal Distribution of Intermittent Suspension Sediments Below Breaking Waves. *Journal of Sedimentary Petrology*, Vol. 51, No. 4 pp. 1103-1108

- LAMBRAKOS, K.F. (1982): Seabed Wave Boundary Layer Measurements and Analysis. *Journal of Geophysical Research*, Vol. 87, No. C6 pp 4171-4189
- LOFQUIST, K.E.B. (1980): Measurements of oscillatory drag on sand ripples. *Proc. 17th Coastal Eng. Conf.*, Sydney, pp 3087-3106
- LONGUET-HIGGINS, M.S. (1981): Oscillating flow over steep sand ripples. *J. Fluid Mechanics*, Vol. 107, pp 1-35
- LUNDGREN, H. (1972): Turbulent Currents in the Presence of Waves, *Proc. 13th International Conference on Coastal Engineering*, Vancouver, pp 623-634
- MACDONALD, T.C. (1977): Sediment Suspension and Turbulence in an Oscillating Flume. *C.E.R.C., Tech. Paper No. 77-4*
- MADSEN, P.A. (1981): A Model For a Turbulent Bore. *Ins. Hydrodynamic and Hydraulic Engineering (ISVA)*, Series Paper 28, 149pp
- MILLER, R.L. (1976): Role of Vortices in Surf Zone Predictions: Sedimentation and Wave Forces. In *Beach and Nearshore Sedimentation*. Ed: R.A. Davis and R.L. Ethington. *Society of Economic Paleontologists and Mineralogists. Special Publication No. 24*
- NAKATO, T., F.A. LOCHER, J.R. GLOVER and J.F. KENNEDY (1977): Wave entrainment of sediment from rippled beds. *Proc. A.S.C.E.* Vol. 103, No. WW1, pp 83-100.
- NAVNTOFT, E. (1968): An Experimental Study on Sediment Transport and Sediment Suspension (in Danish), PhD Thesis, Institute of Hydrodynamics and Hydraulic Eng., Tech. University of Denmark.
- NIELSEN, P. (1979): Some Basic Concepts of Wave Sediment Transport. series Paper 20, *Inst. Hydrodynamics and Hydraulic Engineering (ISVA)*, Technical University of Denmark, 160pp.
- NIELSEN, P. (1981): Dynamics and Geometry of Wave Generated Ripples. *Journal of Geophysical Research*, Vol. 86, No. C7, pp 6467-6472.
- NIELSEN, P. (in press): Explicit Formulae for practical Wave Calculations. To appear in *Coastal Engineering*.
- NIELSEN, P., SVENDSEN, I.A. and STAUB, C. (1978): Onshore-Offshore Sediment Movement on a Beach. *Proc 16th International Conference on Coastal Engineering*, Hamburg pp. 1475-1492.
- NIELSEN, P. and P.J. COWELL (1981): Calibration and Data Correction Procedures for Flow Meters and Pressure Transducers Commonly used by the Coastal Studies Unit. *Tech. Rep. 81/1*, Coastal Studies Unit, Department of Geography, Univ. of Sydney.

- PEREGRINE, D.H. and SVENDSEN, I.A. (1979): Spilling Breakers, Bores and Hydraulic Jumps. Proc. 16th Int. Conf. Coastal Eng., Hamburg pp 540-550.
- RASMUSSEN, P and J. FREDSOE (1981): Measurements of sediment transport in combined waves and currents. Progress Rep. 53, Institute of hydrodynamics and hydraulic engineering, Technical University of Denmark. pp 27-31.
- REIZES, J.A. (1977): A Numerical study of the Suspension of Particles in a Horizontally Flowing Fluid. 6th Australasian Hydraulics and Fluid Mechanics Conference, Adelaide.
- THOMPSON, R.O.R.Y. (1982): A Potential Flow Model of Turbulence Caused by Breaking Waves. Journal of Geophysical Research, Vol. 87, No. C3, pp 1935-1939.
- TOOBY, P.F., WICK, G.L. and ISAACS, J.D., (1977): The Motion of a Small Sphere in a Rotating Velocity Field: A Possible Mechanism for Suspending Particles in Turbulence, Journal of Geophysical Research, Vol. 82, No. 15, pp 2096-2100
- TUNSDALL, E.B. and D.L. INMAN (1975): Vortex generation by oscillatory flow over rippled surfaces. Journal of Geophysical Research, Vol. 80, No. C24, pp. 3475-3485.
- WRIGHT, L.D., J. CHAPPELL, B.G. THOM, M. P. BRADSHAW and P.J. COWELL, (1979): Morphodynamics of Reflective and Dissipative Beach and Inshore Systems: Southeastern Australia. Marine Geology, Vol. 32, pp 105-140
- WRIGHT, L.D., P. NIELSEN, A.D. SHORT and M.O. GREEN (1982) Morphodynamics of a Macrotidal Beach. Marine Geology, Vol. 50
- WRIGHT, L.D., P. NIELSEN, A.D. SHORT, F.C. COFFEY and M.O. GREEN (1982): Nearshore and surfzone morphodynamics of a storm wave environment: Eastern Bass Strait, Australia Tech. Rep. 82/3, Coastal Studies Unit, Dept. of Geography, Univ. of Sydney.

LIST OF SYMBOLS

a	m	Water semi excursion, eq. 4.8.
$\bar{c}(z)$	-	Time averaged suspended sediment concentration
c_o	-	$\bar{c}(0)$
C_n	-	Drag coefficient, eq. 2.43.
C_D	-	Drag coefficient for settling through still water, eq. 3.19
C'_D	-	Instantaneous drag coefficient, eq. 3.13. and 3.15.
C_M	-	Added mass coefficient, eq. 3.13.
d	m	Grain diameter.
\bar{d}	m	Mean grain diameter, eq. 4.4 .
$D(z,t)$	-	Non dimensional velocity deficit, eq. 2.16.
$D_n(z)$	-	Local amplitude of Fourier component of $D(z,t)$, eq. 2.22 .
E	Wm^{-2}	Specific energy dissipation due to bed friction, eq. 2.54 .
f_e	-	Energy dissipation coefficient eq. 2.57 .
f_w	-	Wave friction factor, eq. 2.50, approximately equal to f_e .
f'_w	-	Friction factor corresponding to eq. 2.62 and 2.63 .

f_r	-	Friction factor, roughly including viscous effects. eq. 5.19.
g	$m\ s^{-2}$	Acceleration due to gravity.
h	m	Water depth.
H	m	Wave height, measured from a trough to the following crest.
H_{rms}	m	Root-mean-square wave height.
H_s	m	Significant wave height.
\bar{H}	m	Average wave height.
i	-	Imaginary unit = $\sqrt{-1}$.
k	m^{-1}	Wave number = $2\pi/L$.
k_0	m^{-1}	Deep water wave number.
l	m	Thickness of wave dominated layer, eq. 2.85.
l_s	m	Vertical length scale of exponential \bar{c} -profile, eq. 2.9 (constant).
$l_s(z)$	m	Vertical length scale in general eq. 4.11.
l_v	m	Vertical length scale for distribution of velocity fluctuations, eq. 2.10.
l_v	m	Turbulence length scale, eq. 2.70.
L	m	Wave length.
L_0	m	Deep water wave length = $gT^2/2\pi$.
p	Nm^{-2}	Pressure.
\bar{p}	Nm^{-2}	Time averaged pressure.

\tilde{p}	Nm^{-2}	Periodic pressure component.
Q	$m^2 s^{-1}$	Sediment flux per unit width.
$Q_m(z)$	$m s^{-1}$	Fourier coefficient of local sediment flux, eq. 5.26.
r	m	Bed roughness.
r^2	-	Goodness of fit, eq. 4.18.
R	m	Radius of vortex or particle path.
s	-	Relative sediment density.
t	s	Time.
t_s	s	Spiralling time scale, eq. 3.51.
T	s	Wave period. Experimentally defined by zero crossings of near-bed shore-normal velocities.
$u(z,t)$	ms^{-1}	Horizontal water velocity.
$u_\infty(t)$	ms^{-1}	Velocity outside boundary layer.
$\bar{u}(z)$	ms^{-1}	Time average of $u(z,t)$.
$\vec{u}(x,z,t)$	ms^{-1}	Total water velocity in Chapter 3.
$\vec{u}_p(x,z,t)$	ms^{-1}	Total sediment particle velocity, eq. 3.1.
$\tilde{u}(z,t)$	ms^{-1}	Periodic component of $u(z,t)$.
\bar{u}_*	ms^{-1}	Friction velocity, eq. 2.86.
$U_m(z)$	ms^{-1}	Local amplitude of Fourier component of \tilde{u} .
$\bar{U}(z)$	ms^{-1}	Local amplitude of $\tilde{u}(z,t)$.
\bar{U}	ms^{-1}	Time averaged shore normal velocity.

v_{rms}	ms^{-1}	Root mean square vertical velocity
$\vec{v}(x,z,t)$	ms^{-1}	Sediment velocity component due to flow accelerations, eq. 3.1.
V	-	Variation coefficient for w , eq. 4.6.
\bar{V}	ms^{-1}	Time averaged longshore velocity
w, \vec{w}	ms^{-1}	Sediment settling velocity
\bar{w}	ms^{-1}	Average settling velocity of bed sediment
w'	ms^{-1}	w/\bar{w}
x	m	Horizontal coordinate.
z	m	Vertical coordinate, measured from ripple crest or flat bed level.
z_0	m	Bed roughness parameter for steady flow.
z_1	m	Apparent bed roughness in wave-current boundary layer.
α	-	See eq. 3.24
γ	-	See eq. 3.16
δ	m	Boundary layer thickness, broadly defined.
δ_1	m	Displacement thickness corresponding to the fundamental mode of oscillatory velocity eq. 2.59.
Δ_1	m	Complex displacement thickness, eq. 2.46.
$\epsilon(z)$	m^2s^{-1}	Sediment diffusivity.
$\epsilon_a(z)$	m^2s^{-1}	Apparent diffusivity, eq. 4.14.

ϵ_B	$m^2 s^{-1}$	Limit of ϵ and ϵ_a for $z \rightarrow 0$.
ϵ_S	$m^2 s^{-1}$	Diffusivity due to non boundary layer turbulence eq. 4.14 .
η	m	Ripple height .
θ	-	Shields parameter, eq. 5.15 .
θ'	-	Skin friction Shields parameter eq. 5.17.
θ_c	-	Critical Shields parameter for onset of sediment motion.
κ	-	von Karman's constant ≈ 0.4 .
λ	m	Ripple length.
ν	$m^2 s^{-1}$	Kinematic viscosity of water.
ν_T	$m^2 s^{-1}$	Eddy viscosity.
ν_w	$m^2 s^{-1}$	Eddy viscosity due to wave boundary layer turbulence .
ρ	$Kg m^{-3}$	Density of water.
σ	-	Non dimensional elevation, eq. 4.22 .
τ	Nm^{-2}	Shear stress.
τ'	Nm^{-2}	Bed shear stress due to skin friction alone.
ψ	-	Sediment mobility number, eq. 4.9.
ω	s^{-1}	Angular velocity of waves = $2\pi/T$.
Ω	s^{-1}	Angular velocity in vortices.

HYDRODYNAMICS-, SEDIMENT-, and PROFILE DATA.

RUN	T (s)	h (m)	H _s (m)	ū (m/s)	v̄ (m/s)	t (C)	d̄ (mm)	w̄ (m/s)	V -	λ (m)	η (m)	C _O by vol.	ε _B (m ² /s)	ε _S (m ² /s)	r ²	
1	9.6	1.02	0.51	-0.03	-0.09	-	0.37	0.057	0.110	0.40	0.060	R	0.00214	0.00244	0.077	0.96
2	10.4	0.80	0.42	-0.19	-0.33	-	0.32	0.051	0.110	0.40	0.090	MR	0.00214	0.00172	0.054	0.96
3	5.3	1.29	0.44	0.20	-0.29	26	0.20	0.026	0.285	0.05	0.010	R	0.00315	0.00028	0.265	0.99
4	5.3	1.25	0.41	-0.02	-	26	0.20	0.026	0.285	-	0.000	T	0.00190	0.00039	0.140	0.99
6	8.4	1.76	0.47	-	-	26	0.49	0.055	0.268	0.50	0.050	R	0.00060	0.00280	0.720	0.99
9	7.1	1.62	0.50	-	-	26	0.50	0.063	0.123	0.50	0.150	R	0.00036	0.01230	0.000	0.98
10	7.5	1.42	0.47	-	-	26	0.50	0.063	0.123	0.50	0.150	R	0.00135	0.00740	0.000	0.97
11	7.6	1.29	0.44	-0.04	-	26	0.50	0.063	0.123	0.50	0.150	R	0.00143	0.00934	0.000	-
12	7.2	1.67	0.44	0.00	-	26	0.25	0.030	0.496	0.00	0.000	F	0.00036	0.00120	0.220	0.97
13	8.5	1.50	0.57	-	-	26	0.16	0.017	0.671	-	0.000	F	0.00453	0.00015	0.400	0.99
14	10.8	1.48	0.61	-0.06	-	26	0.23	0.021	0.800	-	0.000	F	0.01100	0.00022	0.260	-
15	12.9	1.42	0.66	-0.11	-	26	0.17	0.018	0.819	-	0.000	F	0.01100	0.00018	0.220	-
16	7.1	1.67	0.43	-	-	26	0.11	0.014	0.344	0.05	0.005	T	0.00149	0.00015	0.310	0.98
17	7.1	1.60	0.33	-	-	26	0.12	0.011	0.615	-	0.000	F	0.00149	0.00015	0.310	0.98
20	5.4	1.50	0.49	0.39	-0.36	26	0.25	0.031	0.489	-	0.000	F	0.00050	0.00091	1.260	0.98
21	7.8	1.50	0.59	0.38	-0.38	26	0.25	0.025	0.489	-	0.000	F	0.00300	0.00040	0.820	-
22	9.5	1.83	0.69	-0.06	-	26	0.20	0.025	0.401	-	0.000	F	0.00434	0.00030	1.110	0.99
23	8.0	1.56	0.66	-0.72	-	26	0.20	0.025	0.411	-	0.000	F	0.00400	0.00034	0.690	-
24	9.3	1.50	0.70	-0.07	0.33	26	0.20	0.026	0.473	-	0.000	F	0.00451	0.00093	0.175	0.98
25	7.1	1.63	0.71	0.09	-	-	0.28	0.048	0.501	0.75	0.075	MR	0.00180	0.00119	0.584	0.95
26	6.4	1.40	0.64	0.04	0.17	-	0.28	0.048	0.501	0.75	0.075	MR	0.00180	0.00113	0.502	0.95
27	6.4	1.55	0.68	0.24	0.12	-	0.28	0.048	0.501	0.75	0.075	MR	0.00180	0.00114	0.556	0.95
28	7.8	1.50	0.54	0.01	-	-	0.33	0.040	0.088	0.70	0.075	R	0.00280	0.00200	0.019	-
29	8.9	1.44	0.47	-0.03	-	-	0.33	0.040	0.088	0.70	0.075	R	0.00160	0.00180	0.030	-
30	8.2	1.59	0.43	0.00	-	-	0.30	0.036	0.072	0.65	0.075	MR	0.00011	0.00250	0.024	-
31	9.0	1.57	0.52	0.04	-	-	0.30	0.036	0.072	0.65	0.075	R	0.00107	0.00171	0.017	-
32	8.2	1.60	0.53	-0.02	-	-	0.40	0.048	0.117	0.80	0.100	R	0.00130	0.00342	0.032	-
33	7.6	1.56	0.55	0.01	-	-	0.40	0.048	0.117	0.80	0.100	R	0.00056	0.00390	0.013	-
34	8.4	1.53	0.61	0.02	-	-	0.40	0.048	0.109	0.60	0.080	R	0.00091	0.00380	0.025	-
35	7.8	1.45	0.55	0.03	-	-	0.40	0.048	0.117	0.60	0.080	R	0.00130	0.00350	0.017	-
36	8.2	1.29	0.74	0.00	0.00	21	0.17	0.019	0.057	-	0.000	F	0.01106	0.00021	0.150	0.97
37	9.4	1.32	0.68	0.00	0.26	21	0.17	0.019	0.064	-	0.000	F	0.00970	0.00056	0.245	0.98
38	9.2	1.34	0.68	0.09	0.25	21	0.17	0.019	0.068	-	0.000	F	0.00970	0.00056	0.245	0.98

NUM	T (s)	h (m)	H _s (m)	B (m/s)	\bar{y} (m/s)	t (C)	\bar{a} (mm)	\bar{w} (m/s)	V -	λ (m)	n (m)	C ₀ by vol.	ϵ_B (m ² /s)	ϵ_S (m ² /s)	r ²	
39	7.9	1.40	0.75	S	0.00	21	0.17	0.019	0.066	-	0.000	F	0.01080	0.00021	0.404	0.99
40	8.6	1.44	0.54	N	0.08	21	0.16	0.019	0.123	-	0.000	F	0.00029	0.00074	0.115	1.00
41	10.5	1.41	0.51	N	0.00	21	0.16	0.018	0.077	-	0.000	F	0.00037	0.00051	0.185	-
42	7.9	1.32	0.48	N	0.09	21	0.20	0.021	0.152	-	0.000	F	0.00032	0.00074	0.107	0.99
43	9.5	1.23	0.58	N	0.08	21	0.16	0.018	0.054	-	0.000	F	0.000045	0.00103	0.027	1.00
44	10.0	1.70	0.44	N	0.00	22	0.44	0.055	0.175	0.55	0.057	R	0.00019	0.00269	0.770	1.00
45	12.0	1.51	0.81	N	0.00	22	0.62	0.074	0.195	0.55	0.057	R	0.00171	0.00598	0.052	0.98
46	10.5	1.29	0.59	N	0.00	22	0.51	0.064	0.203	0.48	0.043	R	0.00061	0.00604	0.260	0.96
47	9.4	1.32	0.45	N	0.00	22	0.45	0.056	0.245	0.48	0.043	R	0.00091	0.00128	0.510	0.99
48	12.9	1.58	0.65	N	0.00	16	0.38	0.049	0.111	0.50	0.080	R	0.00049	0.00540	0.000	0.99
49	12.6	1.57	0.58	N	0.00	16	0.38	0.049	0.111	0.50	0.090	R	0.00020	0.00730	0.000	0.95
50	11.2	1.50	0.56	N	0.03	16	0.45	0.060	0.098	0.35	0.070	R	0.00023	0.000790	0.000	0.97
52	5.7	1.50	0.80	N	0.00	16	0.44	0.058	0.089	0.50	0.080	R	0.00122	0.00369	0.000	0.89
53	7.1	1.04	0.58	N	-0.03	16	0.48	0.063	0.080	0.60	0.080	R	0.00109	0.00496	0.000	0.98
54	7.7	1.10	0.56	N	0.00	16	0.49	0.065	0.096	0.60	0.080	R	0.00090	0.00586	0.000	0.99
55	9.6	1.22	0.62	N	0.06	16	0.47	0.062	0.098	0.60	0.080	R	0.00038	0.00649	0.000	0.99
56	10.2	1.19	0.70	N	0.00	16	0.47	0.062	0.098	0.60	0.080	R	0.00098	0.00622	0.000	0.99
57	9.2	1.21	0.49	N	0.06	16	0.47	0.061	0.122	0.50	0.075	R	0.00157	0.00396	0.000	0.94
58	7.2	1.23	0.45	N	0.08	16	0.47	0.061	0.122	0.50	0.075	R	0.00061	0.00430	0.000	0.99
59	6.2	1.42	0.50	N	0.04	16	0.45	0.060	0.089	0.55	0.100	R	0.00040	0.00536	0.000	0.95
60	6.1	1.48	0.54	N	0.00	16	0.45	0.060	0.089	0.55	0.100	R	0.00022	0.00603	0.000	0.99
61	8.4	1.00	0.67	P	-	22	0.22	0.031	0.121	-	0.000	F	0.01080	0.00186	0.040	0.95
62	8.2	1.00	0.74	P	-	22	0.22	0.031	0.133	-	0.000	F	0.01080	0.00186	0.040	0.95
63	11.9	0.94	0.54	S	-	22	0.20	0.028	0.177	-	0.000	F	0.00390	0.00069	0.117	0.93
64	13.9	0.80	0.45	S	-	22	0.20	0.028	0.177	-	0.000	F	0.00390	0.00059	0.100	0.93
65	14.4	1.80	0.78	S	-	22	0.17	0.024	0.120	-	0.000	F	0.00136	0.00048	0.81	0.98
66	12.9	1.70	0.61	S	-	22	0.17	0.024	0.120	-	0.000	F	0.00136	0.00045	0.76	0.98
67	10.6	1.47	0.68	S	-	20	0.50	0.044	0.132	1.00	0.150	MR	0.00150	0.00218	0.17	0.91
68	10.6	1.48	0.68	S	-	20	0.50	0.044	0.132	1.00	0.150	MR	0.00150	0.00218	0.17	0.91
69	10.6	1.58	0.70	S	-	20	0.50	0.044	0.132	1.00	0.150	MR	0.00150	0.00218	0.20	0.91
70	9.2	1.50	0.82	S	0.10	18	0.38	0.056	0.049	1.50	0.200	MR	0.00089	0.00317	0.35	1.00
71	9.8	1.50	0.77	S	0.10	18	0.38	0.056	0.049	1.50	0.200	MR	0.00947	0.00253	0.23	1.00

MEASURED VALUES OF \bar{c} AND THE CORRESPONDING ELEVATIONS

Run Num- ber	z (1) in metres	c (1) ppm by volume	z (2) in metres	c (2) ppm by volume	z (3) in metres	c (3) ppm by volume	z (4) in metres	c (4) ppm by volume	z (5) in metres	c (5) ppm by volume	z (6) in metres	c (6) ppm by volume	z (7) in metres	c (7) ppm by volume
1	.010	1700	.090	720	.140	130	.240	27	.340	14	.440	21	.540	5
2	.020	890	.100	104	.150	85	.250	21	.350	38	.450	10	.550	9
3	.020	530	.060	98	.110	19	.210	15	.310	12	.410	12	.550	15
4	.040	370	.080	240	.130	130	.230	51	.330	55	.430	55	.570	45
8	.060	200	.100	130	.150	69	.250	53	.350	39	.450	33	.590	29
9	.000	-	.040	360	.090	200	.190	110	.290	77	.390	67	.530	21
10	.070	690	.110	430	.160	250	.260	300	.360	57	.460	41	.600	5
11	.090	1200	.130	630	.180	340	.280	170	.380	91	.480	39	.620	34
12	.0	-	.040	140	.090	46	.190	14	.290	10	.390	12	.530	4
13	.045	140	.085	81	.135	51	.235	39	.335	21	.435	34	.575	21
14	.025	2900	.065	140	.115	77	.215	50	.315	33	.415	39	.555	24
15	.025	1000	.065	190	.115	94	.215	53	.315	70	.415	70	.555	57
16	.020	150	.060	62	.110	33	.210	15	.310	9	.410	15	.550	12
17	.010	1900	.050	130	.100	45	.200	25	.300	17	.400	17	.540	14
20	.045	160	.085	100	.135	87	.235	81	.335	70	.435	63	.575	62
21	.0	-	.040	320	.090	140	.190	94	.290	82	.390	82	.530	79
22	.045	360	.085	210	.135	130	.235	120	.335	170	.435	94	.575	100
23	.060	250	.100	170	.150	130	.250	110	.350	93	.450	82	.590	75
24	.040	1510	.080	655	.130	391	.230	137	.330	64	.430	89	.570	84
25	.060	640	.110	74	.145	51	.246	62	.345	33	.445	24	.586	24
26	-	-	.0	1400	.035	180	.136	76	.235	55	.335	33	.476	48
27	.015	1600	.065	210	.100	58	.201	36	.300	38	.400	31	.541	17
28	.038	2000	.072	550	.120	210	.222	36	.322	17	.422	5	.564	5
29	.038	1200	.072	260	.120	65	.222	26	.322	12	.422	10	.564	10

Run Num- ber	z (1) in metres	c (1) ppm by volume	z (2) in metres	c (2) ppm by volume	z (3) in metres	c (3) ppm by volume	z (4) in metres	c (4) ppm by volume	z (5) in metres	c (5) ppm by volume	z (6) in metres	c (6) ppm by volume	z (7) in metres	c (7) ppm by volume
30	.028	69	.062	70	.110	17	.212	5	.312	3	.412	1	.554	1
31	.028	1900	.062	140	.110	58	.212	12	.312	5	.412	2	.554	1
32	.038	980	.074	430	.120	200	.222	60	.322	29	.422	14	.564	10
33	.015	550	.049	310	.097	140	.199	48	.299	17	.399	7	.541	2
34	.023	660	.057	430	.105	260	.207	84	.307	26	.407	12	.549	7
35	.021	1600	.055	510	.013	220	.205	58	.305	29	.405	15	.547	3
36	.070	120	.109	110	.157	57	.259	17	.358	17	.457	17	.599	17
37	.030	850	.068	450	.118	350	.218	260	.318	210	.417	160	.558	150
38	.050	2380	.089	680	.137	530	.239	340	.338	280	.437	210	.579	160
39	.020	2300	.058	430	.108	340	.208	210	.308	150	.407	150	.548	120
40	.018	210	.057	79	.106	46	.206	24	.306	15	.406	14	.549	7
41	.020	210	.058	45	.108	46	.208	14	.308	7	.407	10	.548	9
42	.030	151	.070	53	.120	22	.220	14	.320	7	.420	5	.560	2
43	.063	19	.113	10	.213	3	.313	2	.413	2	.553	0	-	-
44	.015	137	.054	75	.103	34	.203	19	.303	17	.403	12	.543	10
45	.03	1530	.069	800	.118	218	.218	127	.317	82	.417	21	.558	86
46	.03	600	.068	200	.117	200	.219	100	.317	90	.417	50	.560	50
47	.01	-	.048	140	.098	65	.198	19	.298	19	.397	17	.540	15
48	.030	460	.070	240	.120	154	.220	43	.320	29	.420	14	.520	3
49	.020	310	.060	120	.110	75	.210	43	.310	19	.410	9	.510	10
50	.015	290	.055	150	.105	77	.205	38	.305	29	.405	7	.505	7
52	.030	1340	.070	490	.120	204	.220	160	.320	96	.420	81	.520	81
53	.020	1090	.060	310	.110	170	.210	5	.310	220	.410	2	.510	17
54	.030	980	.070	350	.120	230	.220	67	.320	17	.420	10	.520	3
55	.025	360	.065	-	.115	137	.215	36	.315	17	.415	7	.515	3
56	.030	-	.070	500	.120	254	.220	130	.320	33	.420	12	.520	7
57	.010	-	.040	2700	.080	230	.120	134	.200	60	.280	21	.360	9

Run Num- ber	z(1) in metres	c(1) ppm by volume	z(2) in metres	c(2) ppm by volume	z(3) in metres	c(3) ppm by volume	z(4) in metres	c(4) ppm by volume	z(5) in metres	c(5) ppm by volume	z(6) in metres	c(6) ppm by volume	z(7) in metres	c(7) ppm by volume
58	.010	720	.040	300	.080	182	.120	99	.200	31	.280	15	.360	3
59	.010	610	.040	210	.080	127	.120	76	.200	41	.280	36	.360	5
60	.010	240	.040	136	.080	98	.120	62	.200	33	.280	12	.360	7
61	.040	5900	.070	4000	.122	2700	.222	580	.322	360	.420	300	.567	360
62	.060	3300	.090	2000	.143	1200	.246	570	.343	150	.450	140	.570	75
63	.010	3500	.040	290	.090	160	.195	170	.290	86	.400	54	.510	54
64	.005	3500	.035	900	.088	830	.190	550	.290	440	.400	81	.510	35
65	.025	580	.055	130	.107	86	.210	62	.305	45	.415	44	.515	37
66	.005	950	.035	270	.090	150	.190	94	.288	74	.398	74	.500	59
67	.060	-	.092	770	.144	77	.244	40	.344	75	.444	45	.544	22
68	.000	-	.032	630	.086	330	.190	180	.285	59	.385	22	.490	12
69	.060	-	.090	190	.150	86	.250	35	.350	34	.450	23	.550	18
70	.000	-	.033	490	.083	250	.188	86	.283	55	.383	37	.488	39
71	.020	7000	.050	2700	.100	1300	.200	400	.300	280	.400	130	.500	110

ACKNOWLEDGEMENTS

This study was supported by the Office of Naval Research, Coastal Sciences Program, Task NR 388-157, Grant N-00014-80-G-0001.

All members of the Coastal Studies Unit have put a substantial amount of work into the collection of the present field data.

The manuscript was typed by Wendy Nickalls, Janette Martin and Cheryl Fleury and the figures were drawn by John Roberts and Johanna de Roder. Special thanks to Don Wright for providing excellent working conditions over the last three years.

Unclassified

SECURITY CLASSIFICATION OF THIS PAGE (When Data Entered)

REPORT DOCUMENTATION PAGE		READ INSTRUCTIONS BEFORE COMPLETING FORM
1. REPORT NUMBER	2. GOVT ACCESSION NO. 9121122	3. RECIPIENT'S CATALOG NUMBER
4. TITLE (and Subtitle) SUSPENDED SEDIMENT UNDER WAVES		5. TYPE OF REPORT & PERIOD COVERED TECHNICAL REPORT 1980-1982
		6. PERFORMING ORG. REPORT NUMBER TECH. REP. 82/6
7. AUTHOR(s) P. Nielsen, M.O. Green, F.C. Coffey		8. CONTRACT OR GRANT NUMBER(s) Grant N-00014-80-G-0001
		9. PERFORMING ORGANIZATION NAME AND ADDRESS University of Sydney Coastal Studies Unit Sydney, N.S.W., 2006, Australia
10. PROGRAM ELEMENT, PROJECT, TASK AREA & WORK UNIT NUMBERS NR 388-157		11. CONTROLLING OFFICE NAME AND ADDRESS Office of Naval Research Coastal Sciences Program, Code 422CS Arlington Virginia, 22217
12. REPORT DATE September 1982		13. NUMBER OF PAGES 158
14. MONITORING AGENCY NAME & ADDRESS (if different from Controlling Office)		15. SECURITY CLASS. (of this report) Unclassified
		15a. DECLASSIFICATION/DOWNGRADING SCHEDULE
16. DISTRIBUTION STATEMENT (of this Report) Distribution of this document is unlimited		
17. DISTRIBUTION STATEMENT (of the abstract entered in Block 20, if different from Report)		
18. SUPPLEMENTARY NOTES		
19. KEY WORDS (Continue on reverse side if necessary and identify by block number) Suspended sediment, Sediment transport, boundary layers, waves		
20. ABSTRACT (Continue on reverse side if necessary and identify by block number) A new very simple and dependable field sediment sampler has been developed. It is a multi siphon device that samples suspended same from sevel elevations simulatneously. The 65 concentration profiles that have been obtained so far are presented, complete with hydrodynamics and bed sediment data. The pro-files were measured under breaking and non breaking waves in a wide range of coastal environments all over Australia. These data together with a review of oscillatory boundary layer flow and the motion of the suspended sand in an accelerated non uniform flow lead to a range of new insights into the process		

DD FORM 1 JAN 73 1473

EDITION OF 1 NOV 65 IS OBSOLETE of sediment entrainment under waves.

5/N 0102-LS-014-6601

Unclassified

SECURITY CLASSIFICATION OF THIS PAGE (When Data Entered)